UNIVERSITÀ DEGLI STUDI DI TRIESTE

XXVII CICLO DEL DOTTORATO DI RICERCA IN

INGEGNERIA DELL' INFORMAZIONE

STUDY AND DEVELOPMENT OF ANALYTICAL AND ANALYTICAL-NUMERICAL METHODS FOR THE STUDY OF ELECTRICAL MACHINES

Settore scientifico-disciplinare: **ING-IND/32**

DOTTORANDO
LORENZO BRANZ

COORDINATORE
PROF. ROBERTO VESCOVO

SUPERVISORE DI TESI
PROF. ALBERTO TESSAROLO

ANNO ACCADEMICO 2014 / 2015

Contents

1 Introduzione

Questa tesi di dottorato riassume i principali risultati ottenuti durante il mio dottorato di ricerca. L'attività di ricerca si è focalizzata sulla determinazione di metodi analitici e analitico-numerici per la soluzione di alcuni problemi "aperti" di interesse nella progettazione e l'analisi di macchine elettriche. I temi dello studio sono stati selezionati sulla base di diverse esigenze e criteri, tra cui la rilevanza pratica e l'applicabilità a livello ingegneristico. In realtà, ho sviluppato la mia ricerca lavorando allo stesso tempo in R&D presso Sicor SpA (www.sicor-spa.it), dove sono attualmente impegnato nella progettazione e sviluppo di motori elettrici innovativi da utilizzare in azionamenti per ascensori civili ed industriali. Questo ha posto alcune inevitabili difficoltà dovute all'esigenza di combinare gli impegni lavorativi e di ricerca, ma ha anche fornito una grande quantità di stimoli, idee e ispirazioni per la selezione di nuovi problemi di interesse pratico su cui concentrare l'attenzione da un punto di vista scientifico.

L'attività di ricerca riportata nella tesi include una gamma piuttosto ampia di argomenti, ma è stata sviluppata seguendo una singola linea di indagine unitaria, che consiste nel tentativo di cercare e, dove possibile, definire e implementare, metodi matematici sufficientemente veloci ma accurati per eseguire calcoli su macchine elettriche in modo da evitare l'uso massiccio di tecniche basate su analisi agli elementi finiti. Queste infatti sono note per essere precise ed affidabili, ma allo stesso tempo richiedono ingenti risorse computazionali e sono quindi poco adatte quando è necessario esplorare un gran numero di varianti di progetto, come nel caso di programmi di ottimizzazione progettuale basati su algoritmi genetici. I metodi agli elementi finiti non sono stati esclusi, naturalmente, ma piuttosto utilizzati come "benchmark" per valutare la validità delle tecniche di calcolo alternative proposte, ove non fosse possibile effettuare un confronto diretto con dati sperimentali.

I tipi di macchine elettriche a cui si sono applicati i metodi di calcolo sviluppati in questa tesi sono diversi e vanno dai motori a magneti permanenti superficiali con cave statoricge (capitoli 2, 3, 4) a motori a magneti permanenti superficiali con statore slotless (capitoli 5, 6), dalle macchine sincrone a riluttanza (capitolo 7) alle macchine sincrone a rotore avvolto (capitolo 8), per finire con motori a induzione a gabbia di scoiattolo (capitoli 9, 10). Tutti questi tipi di macchine sono sempre più importanti nelle applicazioni odierne, sia nel settore industriale che per i sistemi di trazione. Per affrontare lo studio di queste macchine si sono di volta in volta sviluppati approcci di calcolo analitico diversi, anche in funzione degli obiettivi da raggiungere.

Esempi di questi approcci analitici impiegati sono i seguenti: la teoria della "winding function" applicata al calcolo della coppia di macchine a magneti superficiali (capitoli 2, 3, 4); la teoria della "permeance function" applicata al calcolo delle macchine con eccentricità di rotore (capitolo 8); l'approccio mediante circuito equivalente magnetico o reti di riluttanze in combinazione a tecniche basate sulle mappe conformi per lo studio dei motori sincroni a riluttanza (capitolo 7); la soluzione delle equazioni di Laplace e di Poisson per determinare il campo magnetico nelle macchine a magneti permanenti superficiali slotless (capitoli 5, 6) e a gabbia di scoiattolo(capitoli 9, 10).

Nel complesso, i principali temi affrontati in questo lavoro di tesi possono essere classificati nelle seguenti categorie principali:

a) Metodo analitico per calcolare la coppia di riluttanza di macchine a magneti permanenti superficiali e per ridurre al minimo la coppia di riluttanza attraverso algoritmi di ottimizzazione genetiche. Questo argomento

è trattato nei capitoli 2, 3 e 4.

b) Studio analitico delle macchine a magneti permanenti slotless, con particolare riguardo al calcolo del campo magnetico all'interno del nucleo di statore e al calcolo della coppia a pieno carico. Il tema è sviluppato nei capitoli 5 e 6.

c) studio analitico delle macchine sincrone a riluttanza con un numero generico di fasi statoriche. Questo è trattato nel capitolo 7.

d) la modellazione analitica di macchine sincrone a rotore avvolto, soggette ad importanti eccentricità di rotore. Questo argomento è trattato nel capitolo 8.

e) calcolo analitico delle induttanze di dispersione di cava di rotore di macchine ad induzione a gabbia di scoiattolo.

In ogni capitolo,viene innanzitutto introdotto l'argomento principale del problema e viene quindi descritto l'approccio utilizzato per la sua soluzione. Inoltre, di volta in volta, viene riportata la descrizione dettagliata delle procedure matematiche e degli algoritmi proposti, compresa la loro rigorosa derivazione teorica. Infine, l'applicazione degli algoritmi di calcolo proposti è illustrata mediante opportuni casi di studio ed i risultati ottenuti sono sempre convalidati mediante confronto con tecniche di calcolo alternative (in particolare l'analisi agli elementi finiti). Particolare enfasi è posta sul ridotto onere computazionale ottenuto applicando le procedure di calcolo proposte, rispetto all'approccio standard, tradizionalmente basato su analisi agli elementi finiti. Naturalmente, ove necessario si sono altresì poste in evidenza le limitazioni dei metodi presentati in termini di eventuale ridotta precisione ed impossibilità di tenere conto di vari effetti "non ideali" come la saturazione magnetica.

Quasi tutti i contenuti inclusi in questa tesi di dottorato sono stati presentati a conferenze sponsorizzate dall'IEEE ed sono stati poi pubblicati a livello di IEEE. Tutti gli articoli pubblicati e citati nella tesi sono infatti disponibili nella banca dati on line IEEEXplore.

Oltre al lavoro incluso in questa tesi, ho condotto vari altri studi, che hanno portato ad altre pubblicazioni (disponibili su IEEEXplore). Tuttavia, questo materiale aggiuntivo non è stato incluso in questa tesi in quanto si è deciso di effettuare una cernita selezionando solo il materiale con maggiore attinenza alla mia attività di ricerca programmata fin dall'inizio del dottorato.

1 Introduction

This doctoral thesis summarizes the main results obtained during my Ph.D. course. My research activity has been mainly focused on the determination of analytical and numerical/analytical methods to approach the solution of some "hot" topics in the design and analysis of electric machines. The topics of the study have been selected based on various needs and criteria, including the practical relevance and applicability to engineering applications. In fact, I have developed my research as a Ph.D. while working, at the same time, a an R&D Engineer in the private company Sicor S.p.A. (www.sicor-spa.it), where I am currently in charge of the design and development of innovative electric motors to be used in full-electric drives for civil and industrial elevators. This has posed some challenges due to the inevitable difficulties of combining my industrial and research commitments, but has also provided me with a large amount of stimuli, ideas and inspiration for selecting new problems of practical interest that could be worth being investigated from a scientific point of view.

The research activity reported in this thesis includes a number of quite different subjects, but has been developed following a single line of inquiry. This is the attempt to find sufficiently fast but accurate mathematical methods to perform calculations on electric machines so as to avoid the massive use of finite element analysis approaches, which are known to be precise and reliable, but extremely time consuming, hence little suitable for usage when a very large number of machine design variants needs to be explored, as in the case of design optimization programs based on genetic algorithms. Finite element methods have not been ruled out, of course, but rather used as a benchmark to assess the validity of the proposed alternative calculation techniques, wherever experimental data were not available for direct comparison with measurements taken on real equipment.

The kinds of electrical machines considered in this thesis are various, ranging from surface-mounted permanent-magnet motors with slotted stator (chapters 2, 3, 4) to surface-mounted permanent-magnet motors with slotless stator (chapters 5, 6), from synchronous reluctance machines (chapter 7) to synchronous wound-field machines (chapter 8), to end with squirrel-cage induction motors (chapters 9, 10). All these kinds of machine are of increasing importance in today's applications, both in the industry and for vehicle traction.

The analytical methods employed to approach the study of these machines are quite different from one case to another. Examples of these analytical approach are the following: the winding function theory applied to the torque computation of surface-permanent magnet machines (chapters 2, 3, 4), the permeance function theory applied to the computation of eccentric-rotor machines (chapter 8), the magnetic equivalent circuit approach combined with conformal mapping techniques for the study of synchronous reluctance motors (chapter 7), the solution of Laplace's or Poisson's partial-derivative differential equations to determine the magnetostatic field inside slotless surface-mounted permanent-magnet machines (chapters 5, 6) and squirrel-cage induction motors (chapters 9, 10).

Overall, the main topics addressed in this work of thesis can be classified into the following main categories:

a) Analytical method to compute the cogging torque of surface permanent-magnet machines and to minimize the cogging torque through genetic optimization routines**.** This subject is covered by chapters 2, 3 and 4.

b) Analytical study of slotless permanent-magnet machines, with special regards to the computation of the magnetic field inside the stator core and of the full-load torque. The topic is developed throughout chapters 5 and 6.

c) Analytical study of synchronous reluctance machines with a generic number of stator phases. This is addressed in chapter 7.

d) Analytical modeling of round-rotor synchronous wound-field machines subject to important eccentricity. This is covered in chapter 8.

e) Analytical computation of slot leakage inductances for the rotor winding of induction machines.

In each chapter, the main relevance of the problem being addressed and the approach used to solve it are described first. Then, a detailed description is provided of the mathematical procedures or algorithm proposed, including their rigorous theoretical derivation, whenever applicable. Finally, the application of the proposed computation algorithms is illustrated by means of suitable case studies and the results are always validated by comparison with alternative computation techniques (including finite element analysis above all). Special emphasis is placed on the computational gains that can be obtained by applying the proposed analytical calculation procedures instead of the standard approach, like finite element analysis. Of course, the limitations of the techniques presented are also pointed out in terms of possibly reduced precision and impossibility to account for various non-ideal effects like magnetic saturation.

Practically the work included in this Ph.D. thesis has been presented in IEEE-sponsored conferences and has been then published by IEEE. All the published papers reporting the material included in the thesis are available in the online database IEEEXplore. In addition to the work included in this thesis, I have conducted various further studies during my Ph.D. course, leading to other publications (available on IEEEXplore as well). However, this additional material has not been included in this thesis as it is found not fully consistent with the aim and scope of my scheduled research activity as a Ph.D. student.

2 Cogging Torque Fast Calculation Method for SPM Machines Based on Winding Function Theory

2.1 Introduction

One of the issues in computing the performance of surface permanent magnet (SPM) machines is the fast evaluation of their cogging torque from design quantities [7]. Although the calculation can be performed by means of finite-element analysis, the use of analytical or numerically-assisted methods is preferable as it allows to obtain results immediately and with no machine geometric model preparation. For this purpose, cogging torque analytical computation through Maxwell's stress tensor is a possible solution. Nevertheless, it has been pointed out in the literature how this approach may give quite inaccurate results due its high sensitivity to air-gap flux tangential magnetic field values [9]. To obtain accurate predictions, various improved formulations have been recently proposed ([1],[4],[10],[7]) based on Maxwell's equation exact analytical solution in the air-gap domain and on field integration through Maxwell's stress tensor method.

In this chapter a relatively simple SPM-motor cogging torque expression is derived where no tangential field component is involved. The expression is derived by treating permanent magnets as fictitious field windings and modeling them through the winding function theory [5]. The application of the approach to various sample SPM machine geometries is presented and found to give satisfactorily accurate results. In particular, it is shown that for a given air-gap field solution, the cogging torque computed with the proposed method is much more accurate than that computed via Maxwell's stress tensor [9]. In other terms, the proposed formulation is not only easier to implement numerically, but also more resilient to possible errors in the determination of the air-gap field.

2.2 Permanent magnet representation through an equivalent field circuit

In order for the winding function approach to apply, it is necessary that permanent magnets are modeled as an equivalent field circuit carrying a constant excitation current I_f. The equivalent field circuit must be such that, when carrying the current I_f, it produces the same air-gap field as permanent magnets do. The concept is illustrated in Fig. 1: Fig. 1a shows a permanent magnet shape suitable for installation on an SPM machine. In the hypothesis of uniform radial magnetization, the field produced by the permanent magnet is the same as that generated by a uniform surface current density j_s flowing on the magnet lateral surfaces as depicted in Fig. 1b.

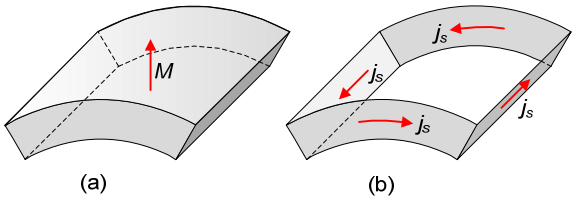

Fig. 1. (a) Surface permanent magnet. (b) Equivalent surface current density.

The equivalent current density j_s has the same value as the radial magnetization M [5], hence we can write:

$$j_s = M = \mu_r H_c \frac{h+\delta}{h+\mu_r \delta} \tag{1}$$

where H_c is permanent magnet coercivity, h is magnet height, μ_r its relative permability and δ is the air-gap width. The total current I_f flowing along each equivalent current sheets shown in Fig. 1b is:

$$I_f = j_s h = Mh = \mu_r H_c \frac{h+\delta}{h+\mu_r \delta} h \tag{2}$$

For example, let us consider the example electric machine illustrated in Fig. 2a. A comparison between the flux density generated by the real permanent magnets and by the equivalent field circuit (both computed by FE method)[2] is illustrated in Fig. 2c. The figure shows that the equivalent field winding perfectly reproduces the effect of permanent magnets.

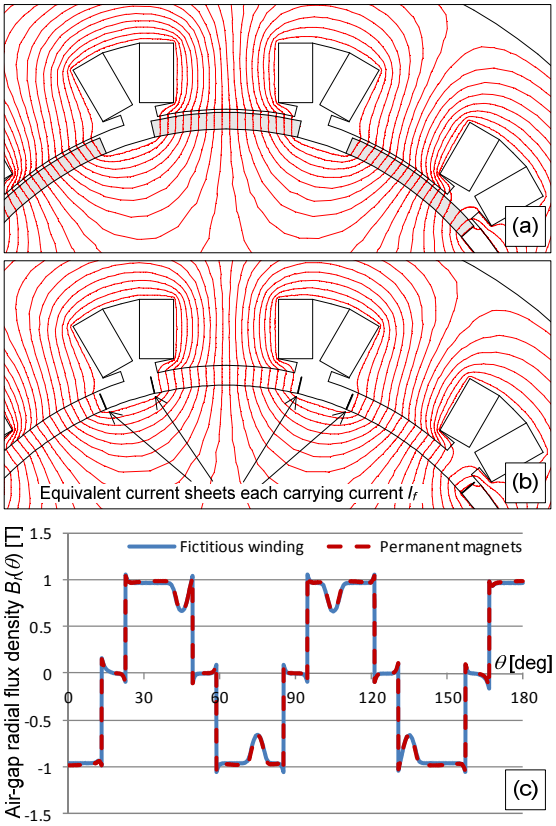

Fig. 2. (a) No-load flux lines in a permanent magnet machine; (b) Flux lines due to equivalent current sheets; (c) comparison between radial flux densities on the mean air-gap circumference.

2.3 Cogging torque computation via winding function theory

For the equivalent field circuit it is possible to introduce a winding function $w_f(\xi)$ that is defined as follows [5]:

$$W_f(\xi) = \frac{h+\delta}{I_f} \frac{B_r(\xi)}{\mu_0}. \tag{3}$$

where ξ is an angular coordinate measured along the air-gap and $B_r(x)$ is the radial flux density which appears on the mean air-gap circumference Γ defined as per Fig. 3, when the equivalent field circuit carries the current I_f, in the hypothesis of slotless stator core (Fig. 3).

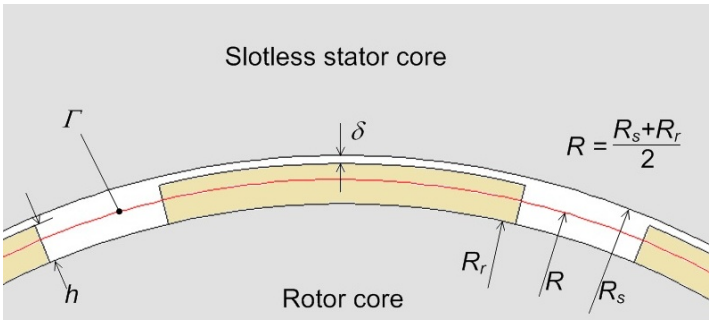

Fig. 3. Mean air-gap circumference Γ and slotless stator model used to define the equivalent field circuit winding function.

When the rotor is at position x, the self inductance of the equivalent field winding can be defined by the WFT as:

$$L(x) = \frac{R L \mu_0}{\delta + h} \int_0^{2\pi} W_f(\xi)^2 P(\xi - x) d\xi \tag{4}$$

where L is the axial core length and $P(\xi)$ denotes the air-gap permeance function, that includes stator slotting effects.

In the hypothesis of unsaturated stator and rotor cores, the electromagnetic torque when the rotor is at position x can be expressed in terms of the inductance derivative with respect to x as follows [3]:

$$T(x) = \frac{1}{2}\left[\frac{d}{dx} L(x)\right] I_f^{\,2} . \tag{5}$$

Substitution of (4) into (5) yields:

$$T(x) = \frac{R L \mu_0 I_f^{\,2}}{2(\delta + h)} \int_0^{2\pi} W_f(\xi)^2 \left[\frac{d}{dx} P(\xi - x)\right] d\xi . \tag{6}$$

Finally, substitution of (3) into (6) gives:

$$T(x) = \frac{R L (\delta + h)^2}{2\mu_0} \int_0^{2\pi} B_r(\xi)^2 \left[\frac{d}{dx} P(\xi - x)\right] d\xi \tag{7}$$

It can be seen from (7) that the equivalent current I_f vanishes in the torque expression. Conversely, two unknown functions of x appear in (7), that are: the no-load air-gap radial flux density B_r(x) of the machine in the hypothesis of slotless air-gap; the permeance function $P(x)$ including slotting effects.

As concerns $P(x)$, it can be computed analytically, for example with the method proposed by Zarko *et al.*, 2008; as an alternative, $P(x)$ can be also computed with a single magnetostatic FE analysis as described by Tessarolo *et al.*, 2012. This latter approach actually requires the stator core geometry to be modeled for FE

analysis, but this task is nowadays very easy to automate in batch mode through user-defined programs (D. Meeker).

As regards the expressions of $B_r(x)$, it can be also determined either analytically ([1], [4], [7], [9], [10]) or by means of a single magnetostatic FE analysis [5].

It is worth noting that determining $P(x)$ and $B_r(x)$ by means of a single magnetostatic FE analysis is definitely a short task compared to the cogging torque computation by FE analysis, which requires to run a large number of simulations, for different rotor positions.

The functions $B_r(x)^2$ and $P(x)$ can be expressed as Fourier-series expansions as:

$$B_r{}^2(x) = \sum_{m=0,1,2,\ldots} b_m \cos(2pmx) \tag{8}$$

$$P(x) = \sum_{n=0,1,2,\ldots} p_n \cos(znx) \tag{9}$$

where p is the number of pole pairs and z is the number of stator slots. By using (8)-(9), the torque expression (7) becomes:

$$T(x) = \frac{RL(\delta+h)^2}{2\mu_0} \sum_{\substack{m=0,1,2,\ldots \\ n=0,1,2,\ldots}} \int_0^{2\pi} b_m p_n n z \cos(2pm\xi)\sin[zn(\xi-x)]d\xi \tag{10}$$

Based on the identity

$$\int_0^{2\pi} \cos(2pm\xi)\sin[zn(\xi-x)]d\xi = \begin{cases} -\pi\sin(nzx) & \text{if } nz = 2pm \\ 0 & \text{otherwise} \end{cases}, \tag{11}$$

(10) can be put in the final form:

$$T(x) = -\frac{\pi RLz(\delta+h)^2}{2\mu_0} \sum_{\substack{m=0,1,2,\ldots \\ n=0,1,2,\ldots}} b_m p_n n \,\delta_{nz,2pm} \sin(znx) \tag{12}$$

where $\delta_{i,j}$ is the Knronecher's delta, which equals 1 if $i=j$, zero otherwise. Equation (12) has the advantage of not including any integral and being easy to compute numerically once Fourier parameters b_m and p_n are known. Cogging torque expression (12) is also much simpler than the one obtained with Maxwell's stress tensor method [9].

2.4 Validation through FE analysis and comparison with Maxwell's stress tensor

The cogging torque expression (12) is assessed on some sample SPM machine geometry and the result is compared with the cogging torque computed by FE analysis. A comparison is also made with the cogging torque computed on the same geometry via Maxwell's stress tensor.

An example of SPM machine geometry taken into consideration is depicted in Fig. 4. The main dimensional data are the following (see Fig. 3 for symbol meaning):

Stator bore radius, R_s:	51.5 mm	Permanent magnet permeability:	1.04
Magnet height, δ:	3 mm	Permanent magnet coercivity:	918200 A/m
Air-gap width, g:	0.8 mm	Number of stator slots, z:	24
Permanent magnet span:	9/10 of pole span	Core length:	210 mm

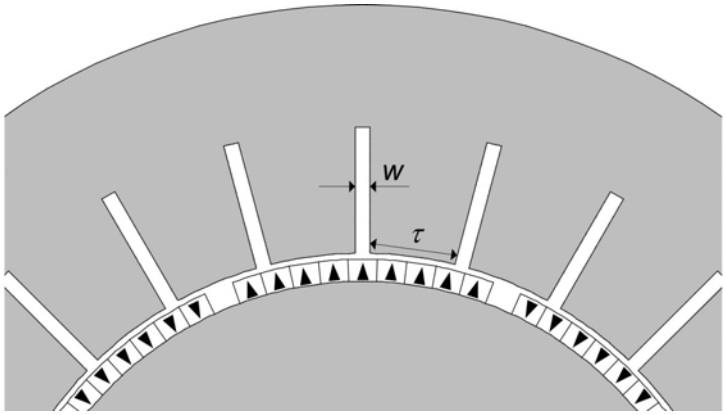

Fig. 4. Example of the machine cross section considered for method assessment.

To assess the method accuracy for different air-gap profiles, the cogging torque computation is run for various machine geometries characterized by different pole pairs p (the cases of p=2 and p=3 are hereinafter addressed) and different slot widths w (Fig. 4). The slot width values considered and the corresponding tooth to slot width ratios are provided in Table I.

Table I

w	τ / w
2 mm	5.7
4 mm	2.4
6.7 mm	1.0

The cogging torque computation is performed for both the 4-pole and 8-pole configurations with the slot width assuming the values in Table I. For assessment purposes, three methods of computation are compared, i.e.:

a) the FE method, where a set of magnetostatic simulations is run on the machine cross section for equally-spaced rotor positions with 0.5 mm step;

b) the proposed method based on the winding function theory and summarized by (12); the flux density and permeance function Fourier coefficients appearing in (12) are computed analytically as per [9];

c) by the analytical method proposed by [9] based on Maxwell's stress tensor.

The results obtained with the three approaches are shown in Fig. 5. As usually done in the literature [8], the FE calculation is assumed to give the correct cogging torque profile. With respect to such FE computation,

the proposed method proves to be satisfactorily accurate, especially if compared to the analytical result obtained through Maxwell stress tensor's method.

It is worth noting that both methods *b)* and *c)* employ an analytical field solution for the air-gap flux density which is not exact and, in particular, exhibits some inaccuracy in the tangential air-gap field component [9]. Nevertheless, one can observe that the proposed method gives more accurate cogging torque results and then seems more robust than Maxwell's stress tensor method, i.e. less sensitive to possible inaccuracies in the air-gap field computation. A possible explanation of this lies in the fact that the proposed leads to a cogging torque expression (12) where the tangential field component does not appear.

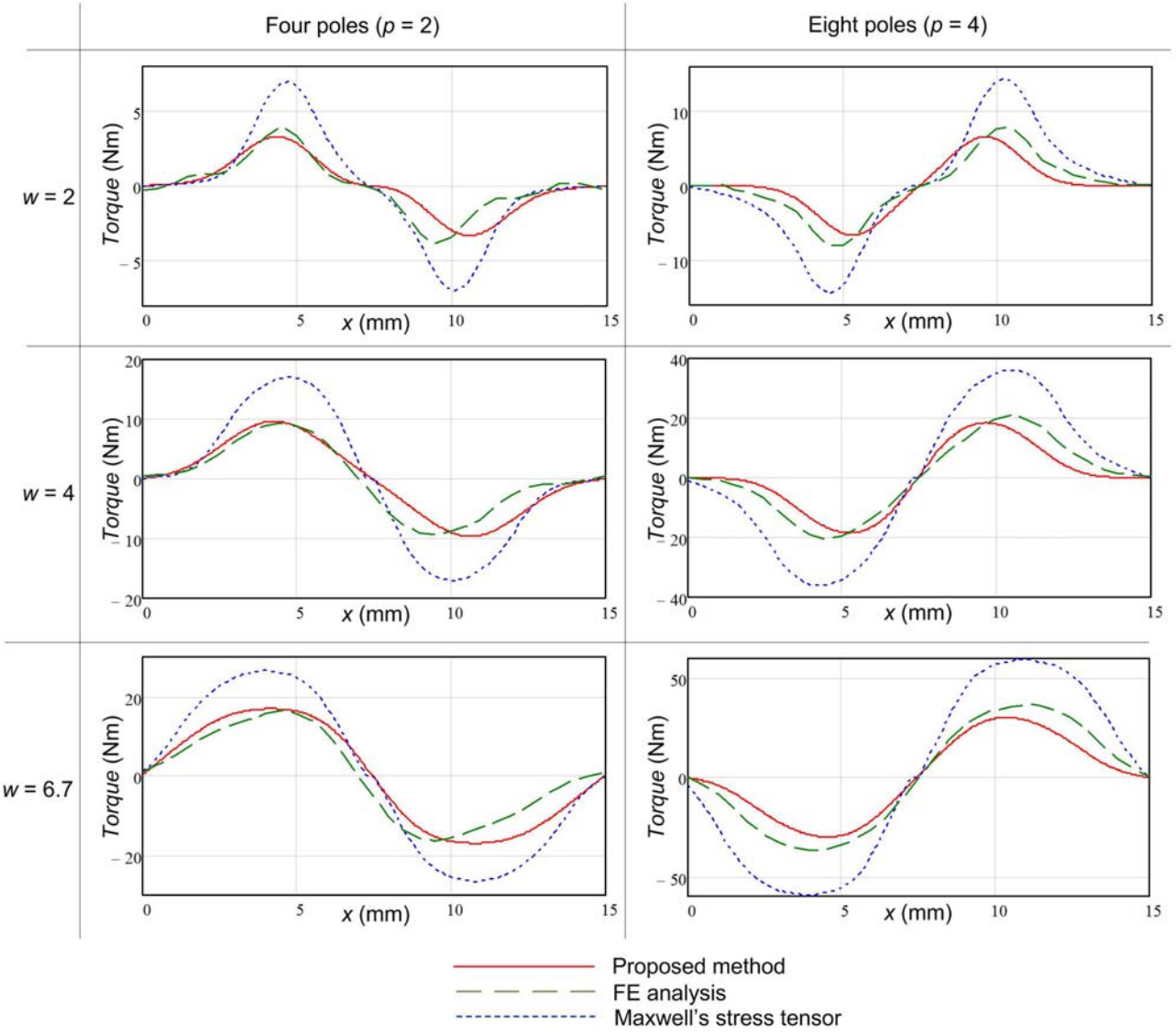

Fig. 5. Cogging torque diagrams computed with different techniques.

2.5 Conclusion

In this chapter a cogging torque computation method has been proposed for SPM machines. The method has been derived by replacing surface-mounted permanent magnets by appropriate current sheets capable of producing the same air-gap field and thus modeling permanent magnets through the winding function theory. Compared to previously proposed formulas, based on Maxwell's stress tensor, the analytical cogging torque expression derived in the chapter is much simpler to implement and has the property of not including the air-gap tangential field component. The accuracy of the method has been assessed on various SPM machine geometries featuring different slot-to-tooth width rations and different pole numbers. In all the cases, the proposed technique has been proved to give more accurate results than the Maxwell's stress tensor, exhibiting a better robustness with respect to inaccuracies in the air-gap field solution.

2.6 References

[1]Lin, D., Ho, S.L., Fu, W.N. (2009), "Analytical Prediction of Cogging Torque in Surface-Mounted Permanent-Magnet Motors", *IEEE Transactions on Magnetics*, vol. 45, no. 9, pp. 3296-3302.

[2]Meeker D., *Finite Element Method Magnetics (FEMM): A Free Magnetic Finite-Element Package for Windows* [Online]. Available: http://www.femm.foster-miller.net.

[3]Nagel, N.J., Lorenz, R.D. (2000), "Modeling of a saturated switched reluctance motor using an operating point analysis and the unsaturated torque equation", *IEEE Transactions on Industry Applications*, vol.36, no.3, pp.714-722.

[4]Starschich, E., Muetze, A., Hameyer, K. (2010), "An Alternative Approach to Analytic Force Computation in Permanent-Magnet Machines", *IEEE Transactions on Magnetics*, vol. 46, no. 4, pp.986-995.

[4]Tessarolo A. (2012, in press), "Accurate Computation of Multiphase Synchronous Machine Inductances Based on Winding Function Theory", *IEEE Transactions on Energy Conversion*.

[5]Tessarolo, A., Agnolet, F., Luise, F., Mezzarobba, M. (2012), "Use of Time-Harmonic Finite-Element Analysis to Compute Stator Winding Eddy-Current Losses Due to Rotor Motion in Surface Permanent-Magnet Machines", *IEEE Transactions on Energy Conversion,* vol. 27, no. 3, pp. 670-679.

[6]Wu, L.J., Zhu, Z.Q., Staton, D., Popescu, M., Hawkins, D. (2011), "An Improved Subdomain Model for Predicting Magnetic Field of Surface-Mounted Permanent Magnet Machines Accounting for Tooth-Tips", *IEEE Transactions on Magnetics*, vol. 47, no. 6, pp.1693-1704.

[7]Wu, L.J., Zhu, Z.Q., Staton, D.A., Popescu, M., Hawkins, D. (2012) "Comparison of Analytical Models of Cogging Torque in Surface-Mounted PM Machines", *IEEE Transactions on Industrial Electronics*, vol. 59, no. 6, pp. 2414-2425.

[8]Zarko, D., Ban, D., Lipo, T.A. (2008), "Analytical Solution for Cogging Torque in Surface Permanent-Magnet Motors Using Conformal Mapping", *IEEE Transactions on Magnetics,* vol. 44, no. 1, pp. 52-65.

[9]Zhu, Z.Q., Wu, L.J., Xia, Z.P. (2010), “An Accurate Subdomain Model for Magnetic Field Computation in Slotted Surface-Mounted Permanent-Magnet Machines”, *IEEE Transactions on Magnetics*, vol. 46, no. 4, pp.1100-1115.

3 Special Magnetic Wedge Design Optimization with Genetic Algorithms for Cogging Torque Reduction in Permanent-Magnet Synchronous Machines

3.1 Introduction

In electric machines with open-slot stator design, magnetic wedges are often used to improve the flux-density profile in the air-gap by reduction of slotting harmonics [1], [2], [3]. This problem can practically occur in high-torque permanent-magnet motors for traction applications, which are characterized by small voltage and high current values and are therefore designed with flat-turn windings and open stator slots [4].

In [5], a new magnetic wedge design is proposed for reducing the cogging torque of open-slot permanent-magnet machines and contemporarily controlling phase inductance values. In [5] finite-element analyses are used to show how the change in the proposed wedge design can significantly affect machine behavior and parameters in terms of phase inductance and cogging torque.

In this chapter, the purpose is to find the optimal wedge geometry in order to minimize the cogging torque amplitude for a given surface permanent-magnet machine structure. The problem is numerically solved by means of a genetic optimization algorithm combined with a finite-element code for automatic cogging torque calculation.

3.2 Wedge technology and problem statement

The magnetic wedge technology presented in [5] is exemplified by the sample piece shown in Fig. 1. It can be seen that magnetic body of the wedge is crossed by a groove filled with a non-magnetic bar for mechanical reasons. The groove is simply obtained by a milling process applied to a magnetic wedge of traditional type and, by using different milling tools, can be suitably shaped as concerns its width w groove depth h, it is not very significant from a functional viewpoint because the magnetic wedge portion below the groove saturates and, due to saturation, the wedge practically behaves as if the groove depth were equal to the wedge thickness (Fig. 2b).

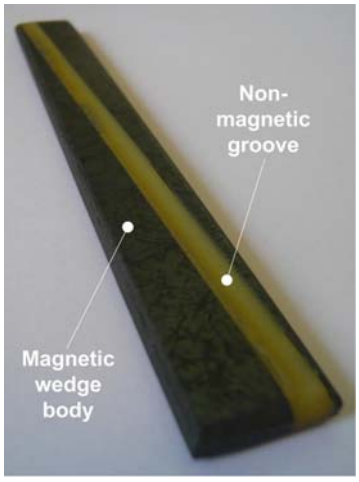

Fig. 1. Magnetic wedge prototype with slant non-magnetic groove.

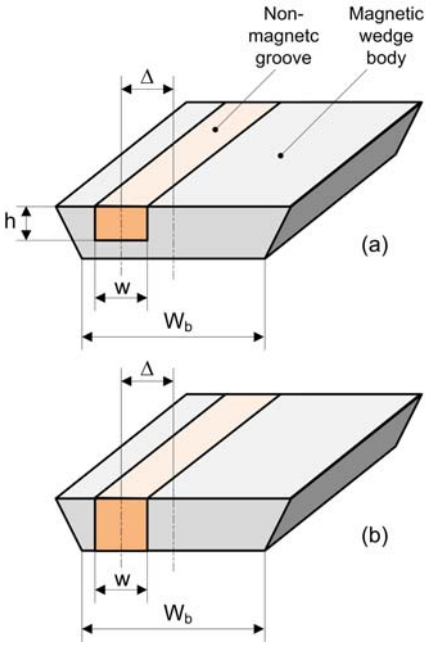

Fig. 2. Scheme of proposed magnetic wedge geometry and dimensions.

Finally, the groove can be slanted with respect to the wedge longitudinal axis, as in the case shown in Fig. 1, thus producing a stator skewing-like effect.

The influence of wedge geometry on machine phase inductance and cogging torque amplitude has been discussed in [5] showing how the groove width w strongly affects the slot leakage inductance.

As concerns cogging torque amplitude, it has been shown that significant enhancement can be obtained by changing the groove position with respect to the wedge center in the various slots. For example, let us consider a four-pole surface permanent-magnet machine with Z=12 stator open slots as shown in Fig. 3 (the geometric data of the sample machine are reported in [5]). If we number the slots from 1 to Z, we can decide that the groove placed in the k^{th} slot has a groove whose distance Δ from the center (see Fig. 2) is equal to Δ_k. For the sake of commodity, let us denote the groove position with respect to the center of the k^{th} wedge with the non-dimensional parameter δ_i defined as follows:

$$\delta_i = \frac{2\Delta_i}{W_b - w} \qquad (1)$$

where W_b is the wedge width and w the groove width.

It can be easily seen that parameter δ_i may vary between –1 and 1. In particular, it is –1 when the groove is completely shifted to the left, 1 when it is completely shifted to the right, 0 when it is centered [5].

Furthermore, let us suppose that the groove width w has been fixed to obtain the desirable value of phase inductance as discussed in [5]. The problem is now to determine the optimal groove positions in all the Z

stator slots so as to minimize the cogging torque amplitude. In mathematical terms, the vector of non dimensional parameters δ_k (with $k = 1..Z$) is to be determined so as to minimize the cogging torque amplitude.

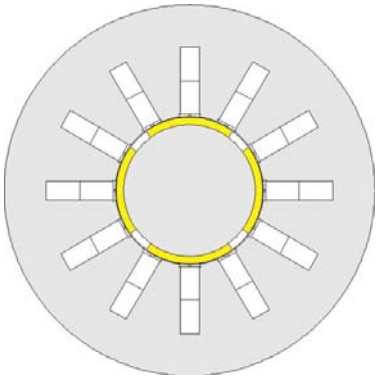

Fig. 3. Sample surface permanent-magnet machine considered for optimization

3.3 Optimization problem implementation in the modefrontier environment

The optimization problem stated above is a single-objective problem with twelve constrained design variables. The single objective function is the cogging torque peak T_{peak} to be minimized. The constrained design variables are the twelve real numbers δ_i which are allowed to vary in the [–1, 1] interval. In mathematical terms the problem can be stated as follow:

$$\begin{cases} \text{minimize } T_{peak}(\delta_1, \delta_2, \delta_2, \delta_4, ..., \delta_{11}, \delta_{12}) \\ \delta_k \in [-1, 1] \quad \forall k = 1,2,3..12 \end{cases}$$

The function T_{peak} which links the cogging torque amplitude to the twelve design variables δ_k could be expressed analytically by resorting to such algorithms as presented, for instance, in [7]. However, due to the well known inaccuracy in present analytical methods for cogging torque computation, it is find more reliable, although more time consuming, to implement the function T_{peak} ($\delta_1,\ldots\delta_{12}$) numerically, that is by means of a sequence of finite-element analysis.

The cogging torque calculation for any vector $\delta_1,\ldots\delta_{12}$ of design variables is performed by means of a program written

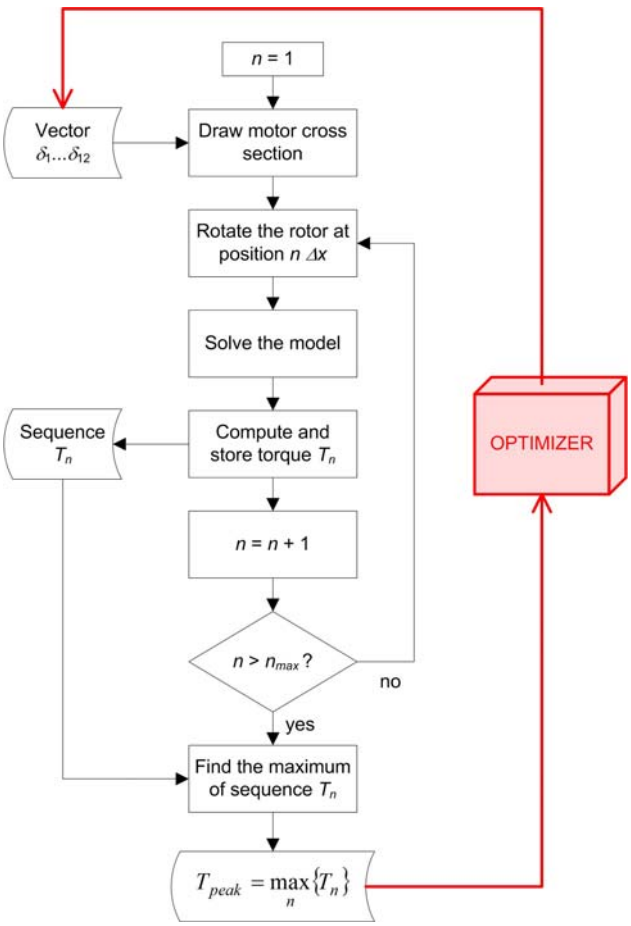

Fig. 4. Flow chart for the numerical calculation of the cogging torque by finite-element analysis.

in LUA language which implements the flowchart drawn in Fig. 4 with black thin line. The program fist builds the machine model as shown in Fig. 3 by using the current vector ($\delta_1,\ldots\delta_{12}$) of design variables to correctly place the wedge grooves. Then it performs a "for" loop by changing the rotor position by Δx -wide steps and, for the n^{th} generic rotor position, it computes and stores the cogging torque value T_n. The computation is done by the FEMM software whose tasks can be executed through appropriate LUA language commands in batch mode [8]. When all the rotor positions across a 360-degree span have been analyzed, the program searches for the maximum in the vector $| T_n |$ of cogging torque amplitudes and sets T_{peak} equal to such maximum value. The objective function T_{peak} thus calculated is then fed into the optimizer which, based on genetic algorithms, will appropriately decide the following vector of design variables ($\delta_1,\ldots\delta_{12}$) to be explored.

The optimization process described has been implemented in the modeFrontier® environment [9] through the workflow diagram reported in Fig. 5. The workflow illustrates how the twelve input variables $\delta_1,\ldots\delta_{12}$ are separately treated and, at any optimization step, transferred into the input file. The application node, at each iteration, launches the LUA program which performs the cogging torque computation through the flowchart shown in Fig. 4. The LUA program writes the results (cogging samples) in an output file and the cogging torque absolute peak in a further file which is intended to contain the number to be minimized.

The overall optimization process employs the MOGA II algorithm (Modified Genetic Algorithm, [9]). The inizialization of the optimization process is performed by a DOE (Design of Experiments) section which

used the simplex algorithm to indentify the initial designs to be explored which form the set from which the genetic algorithm search is started.

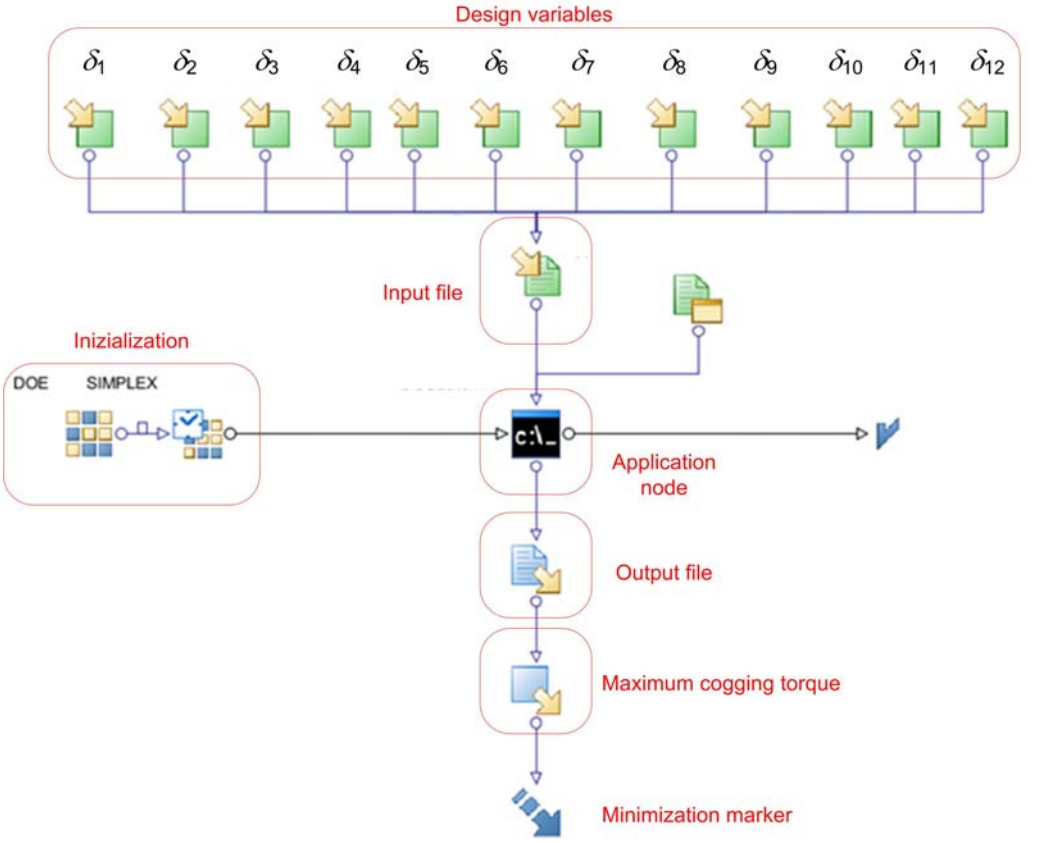

Fig. 5. Workflow that implements the optmization in the modeFrontier environment.

3.4 Optimization results

In the optimization process, more than one hundred configurations have been explored. Each configuration is simply called "design" and is assigned a progressive design ID. Each design is univocally determined by the order set of the twelve design variables $\delta_1,\ldots\delta_{12}$.

A first diagram which can be used to visualize the optimization process output is shown in Fig. 6. It represents the cogging torque amplitudes computed for all the explored design, ordered by design ID. It can be seen that, at the beginning (low design ID values) the amplitudes are relatively high and quite randomly distributed. As the optimization process continues (i.e. for increasing design ID values), the genetic algorithm tends to select only the "fittest" designs, whose cogging torque amplitude, in fact, tends to a value around 1.23 Nm. This value can be treated as the lowest amplitude that can be achieved, provided that the optimization algorithm has worked properly identifying a global and not only local minimum for the given problem.

Another view of the optimization output is provided in fig. 7, where we can see the values taken by all the design variables throughout the optimization. Representing all the design variable trajectories in the same diagram results in a quite confuse representation, so Fig. 8 shows the trajectory followed by each single

design variable separately. The *y*- axis scale is between –1 and 1 for all the design variables, while the abscissa is the design ID in all cases.

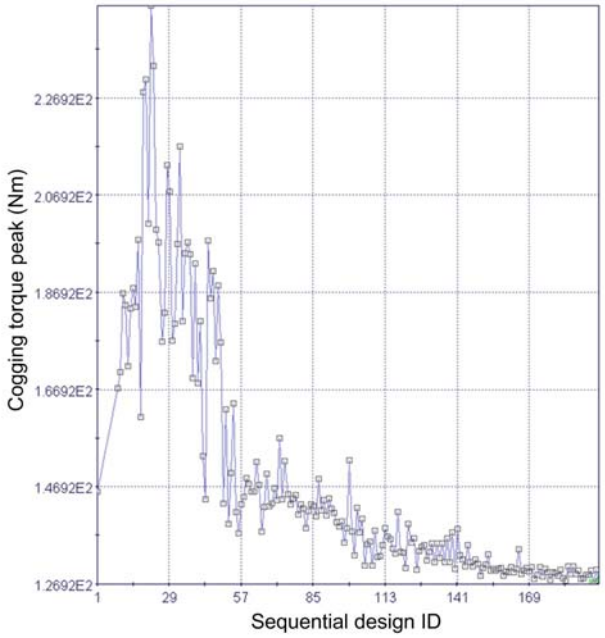

Fig. 6. Peak torque values found throughout the optimization and plotted versus design ID.

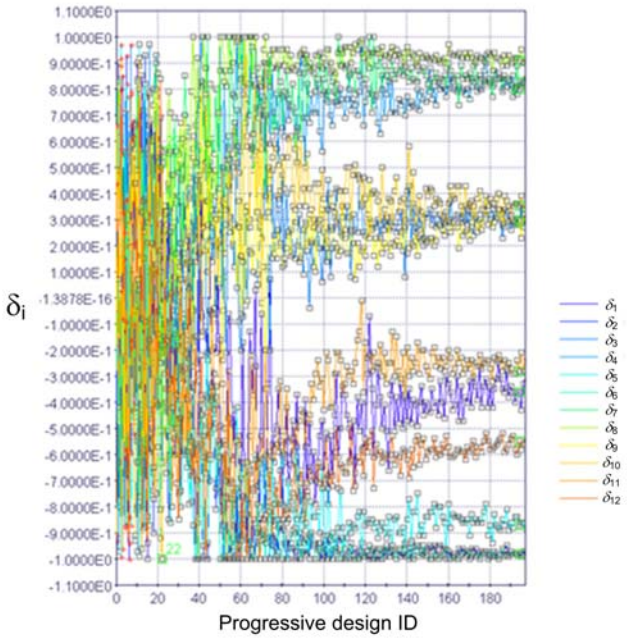

Fig. 7. Trajectory of the twelve design variables throughout the optimization

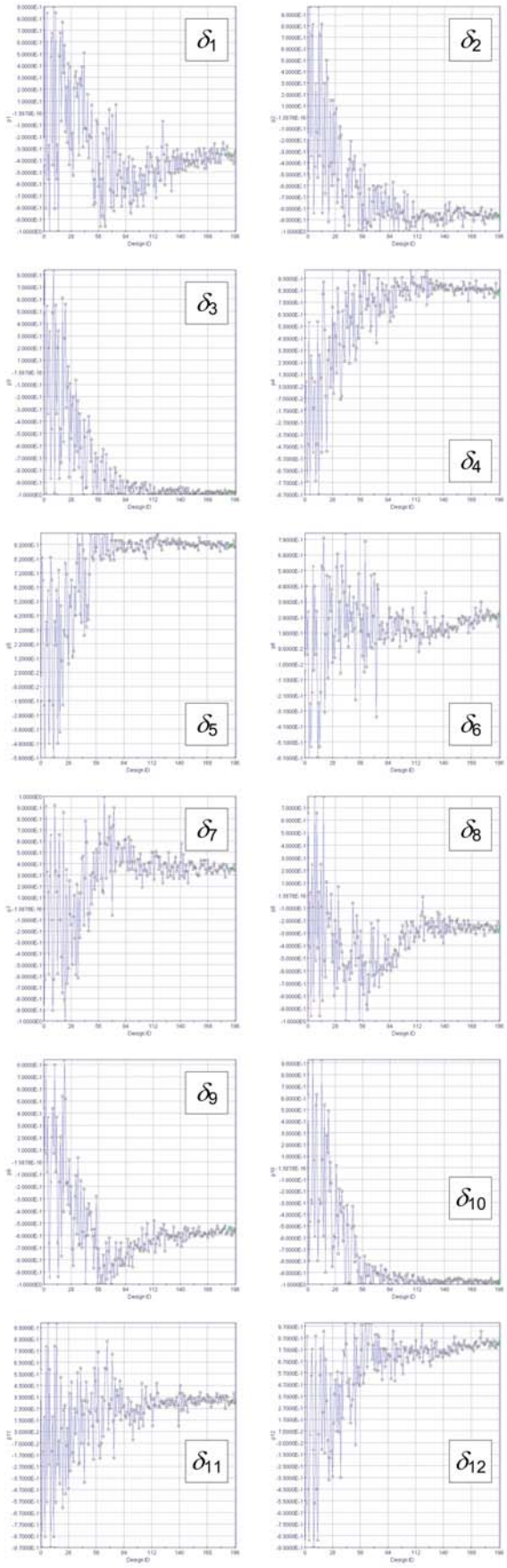

Fig. 8. Trajectory of the twelve design variables throughout the optimization

From Fig. 8 it can be clearly seen that each design variable, after an initial wide fluctuation, tends toward a quite precise value which defines its optimal value.

The optimal solution is then constituted by the vector of variables δ_i indicated as "optimal" in the histogram in Fig. 9. For the sake of comparison, two more design solutions are considered in the same figure, i.e. the worst design (which gives the highest torque ripple amplitude found throughout the optimization) and a generic non-optimal solution.

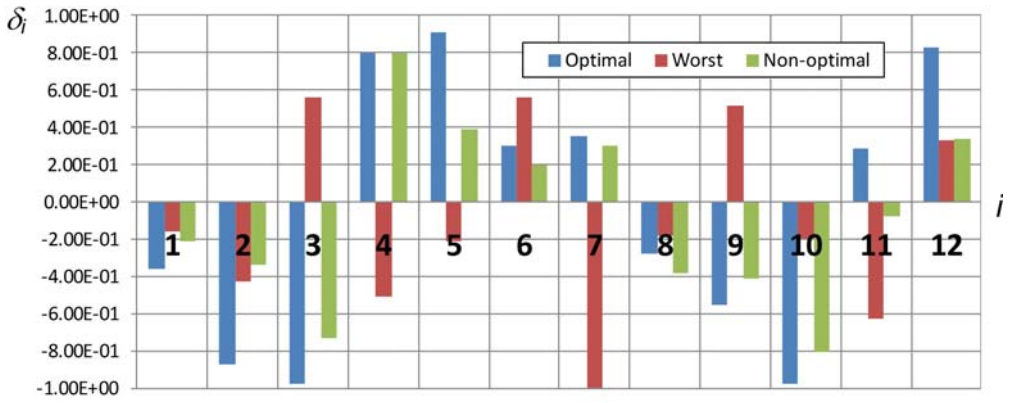

Fig. 9. Numerical values of three design solutions: the optimal one, the worst one (among those been explored) and a generic non-optimal one.

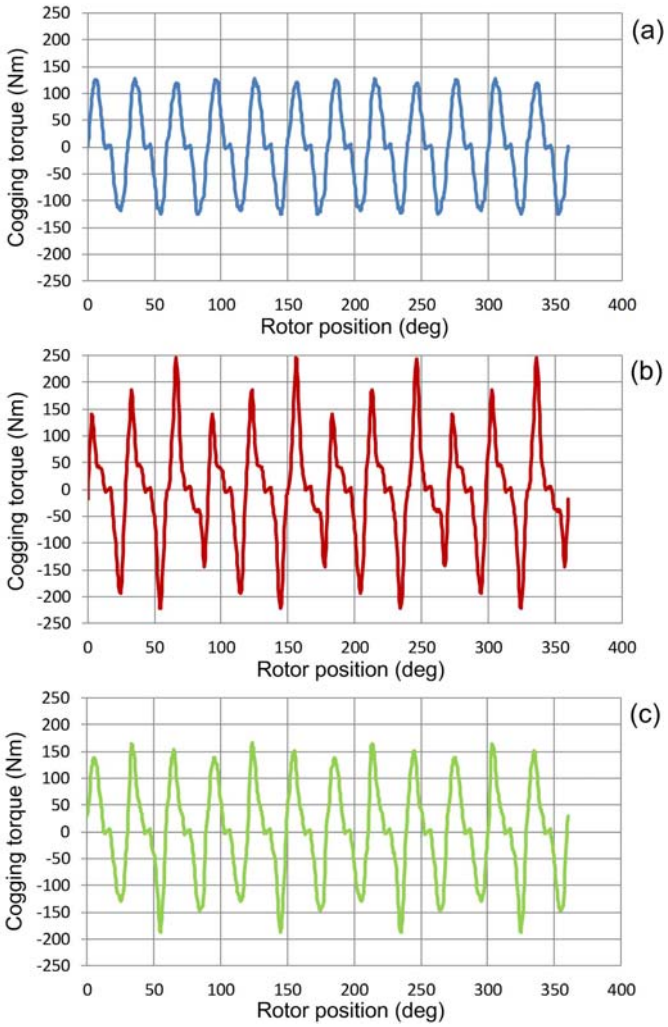

Fig. 10. Cogging torque waveforms for: (a) optimal design; (b) worst design; (c) generic non-optimal design.

The cogging torque waveforms corresponding to the three designed mentioned above are reported in Fig. 10.

From a physical point of view, the optimal design determines a univocal distribution of groove positions around machine air-gap. Such distribution is illustrated in Fig. 8.

Such configuration is the one which can minimize the cogging torque. It may be interesting to note that, from Fig. 9 and Fig. 11 the optimal solution does not seem to be characterized by any particular recognizable pattern, which suggests that finding it without a genetic optimization program would not be possible or, at least, intuitive. Nevertheless, one can also observe from Fig. 10 one can see that the optimal solution leads to a surprisingly “regular” (i.e. periodic) cogging torque waveform, unlike non-optimal solutions.

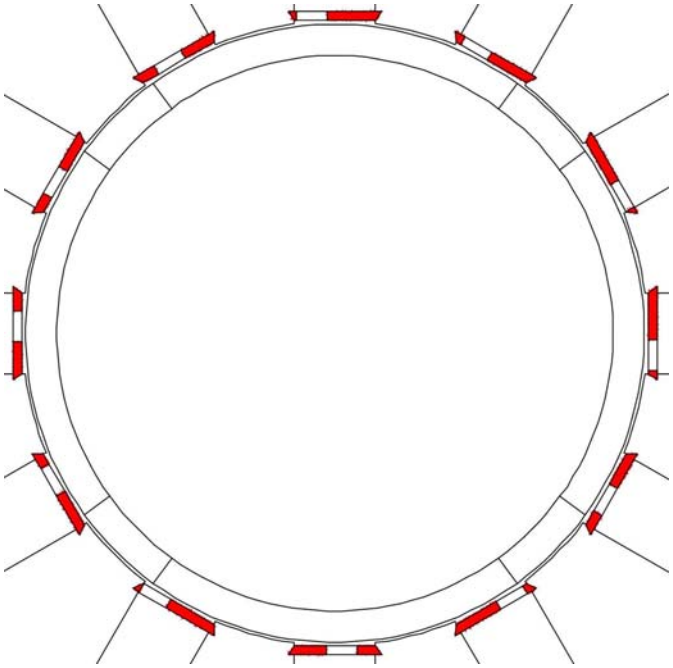

Fig. 11. Oprimal distribution of magnetic wedge grooves resulting from the optimization.

3.5 Conclusion

Cogging torque is a well known disadvantage of permanent-magnet machines, especially if designed with open stator slots. In a previous paper, a special magnetic groove design had been proposed to reduce cogging torque effects. In this chapter, such wedge design has been considered in more detail with the specific aim of finding its optimal design, which minimized the cogging torque amplitude. For this purpose, a genetic optimization algorithm, available in the modeFrontier software environment, has been employed. As a result of the optimization process, an optimal machine design with grooved wedges has been finally identified. Such optimal design does not exhibit any apparent feature such as to enable its recognition also without an optimization procedure. However, it has been also noted that the cogging torque waveform corresponding to the optimal design is not only the one with minimum amplitude, but also shows a periodic waveform which cannot be found, in general, in non-optimal design solutions.

3.6 References

[1] Y. Takeda, T. Yagisawa, A. Suyama, M. Yamamoto, "Application of magnetic wedges to large motors," *IEEE Transactions on Magnetics,* vol. 20, no. 5, pp. 1780- 1782, Sep 1984.

[2] Di Napoli, O. Honorati, E. Santini, L. Solero, "The use of soft magnetic materials for improving flux weakening capabilities of axial flux PM machines", *IEEE Industry Applications Society Annual Meeting 2000*, Oct. 2000, vol. 1, pp. 8-12.

[3] Daohan Wang, Xiuhe Wang, Dongwei Qiao, Ying Pei; Sang-Yong Jung, "Reducing cogging torque in surface-mounted permanent-magnet motors by nonuniformly distributed teeth method", *IEEE Transactions on Magnetics,* vol.47, no.9, pp.2231-2239, Sept. 2011.

[4] F. Luise, A. Odorico, A. Tessarolo, "Extending the speed-range of surface permanent-magnet axial-flux motors by flux-weakening characteristic modification", *International Conference on Electric Machines*, *ICEM 2010*, 6-9 Sept. 2010, Rome, Italy, CD-ROM paper RF-008893.

[5] A. Tessarolo, F. Luise, M. Mezzarobba, "A new magnetic wedge design for enhancing the performance of open-slot electric machines", *ESARS 2012*.

[6] F. Luise, A. Calonico, "Bietta magnetica per macchine elettriche rotanti" (Magnetic wedge for rotating machines slots), International patent pending, P03894/PCT, March 2012.

[7] D. Zarko, D. Ban, T.A. Lipo, “Analytical calculation of magnetic field distribution in the slotted air gap of a surface permanent-magnet motor using complex relative air-gap permeance”, *Magnetics, IEEE Transactions on* , vol.42, no.7, pp. 1828- 1837, July 2006.
[8] D. Meeker, Finite Element Method Magnetics (FEMM): A Free Magnetic Finite Element Package for Windows [Online]. Available: http://www.femm.foster-miller.net.
[9] *ESTECO, modeFrontier*, www.esteco.it.
[10] A. J. Mitcham, G. Antonopoulos, J. J. A. Cullen, "Favourable slot and pole number combinatio for fault-tolerant PM machines", *IEE Proceedings - Electric Power Applications,* vol.151, no.5, pp. 520- 525, 9 Sept. 2004.

4 Special Magnetic Wedge Design Optimization with Genetic Algorithms for Cogging Torque Reduction in Permanent-Magnet Synchronous Machines Based on Winding Function Theory

4.1 Introduction

Also already mentioned in previous chapter, magnetic wedges are often used to improve the flux-density profile in the air-gap by reduction of slotting harmonics [1], [2], [3]. This problem can practically occur in high-torque permanent-magnet motors for traction applications, which are characterized by small voltage and high current values and are therefore designed with flat-turn windings and open stator slots [4].

In [5], a new magnetic wedge design is proposed for reducing the cogging torque of open-slot permanent-magnet machines and contemporarily controlling phase inductance values. In [5] finite-element analyses are used to show how the change in the proposed wedge design can significantly affect machine behavior and parameters in terms of phase inductance and cogging torque.

In the previous chapter, the purpose is to find the optimal wedge geometry in order to minimize the cogging torque amplitude for a given surface permanent-magnet machine structure. The problem is numerically solved by means of a genetic optimization algorithm combined with a finite-element code for automatic cogging torque calculation.

In this chapter, the purpose is the same, but the problem is solved by means of a genetic optimization algorithm combined with a MATLAB code for automatic cogging torque calculation.

The cogging torque calculation are based on winding function theory as well described in the chapter 2 . It allows to obtain results immediately and with no machine geometric model preparation.

4.2 Optimization problem implementation in the modefrontier environment

The optimization problem is a single-objective problem with twelve constrained design variables. The single objective function is the cogging torque peak T_{peak} to be minimized. The constrained design variables are the twelve real numbers δ_i which are allowed to vary in the [–1, 1] interval. In mathematical terms the problem can be stated as follow:

$$\begin{cases} \text{minimize}\, T_{peak}(\delta_1, \delta_2, \delta_2, \delta_4, ..., \delta_{11}, \delta_{12}) \\ \delta_k \in [-1, 1] \quad \forall k = 1,2,3..12 \end{cases}$$

The function T_{peak} which links the cogging torque amplitude to the twelve design variables δ_k could be expressed analytically by a fast computational method based on winding function theory. Usually, due to the well known inaccuracy in analytical methods for cogging torque computation, it is considered more reliable,

although more time consuming, to implement the numerical method, that is by means of a sequence of finite-element analysis.

The cogging torque calculation for any vector $\delta_1,\ldots\delta_{12}$ of design variables is performed by means of a program written in MATLAB language which implements the flowchart drawn in fig 4.

The program calculates the Cogging torque T_k throw analytical method as follow:

$$T_k = -\frac{\pi R L z (\delta + h)^2}{2\mu_0} \sum_{\substack{m=0,1,2,\ldots \\ n=0,1,2,\ldots}} b_m p_n n \, \delta_{nz,2pm} \sin(z n k \Delta x) \qquad (1)$$

Where p_n and b_m are permeance and winding function Fourier series parameters respectively.

Pearmeance function obtained by comformal mapping[8][9], whereas slot open equivalent to the wedge groove width. In addition wedge permeability equal the lamination one($\mu_r = \infty$) .Indeed the wedge permeability $\mu_r = 100$. The proposed method doesn't allow different permeability between lamination and wedge. This approximation does not imply a limit to the attainment of the objective.

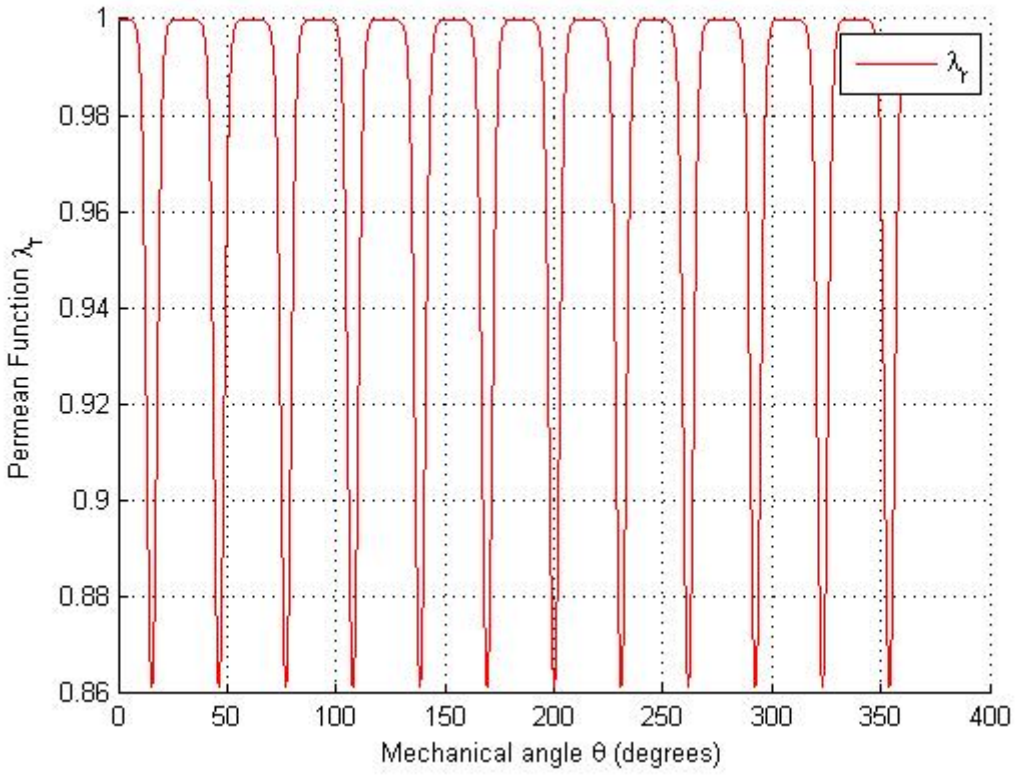

Fig. 1. Analytic Permeance function of magnetic wedge grooves centered respect to the center of wedges.

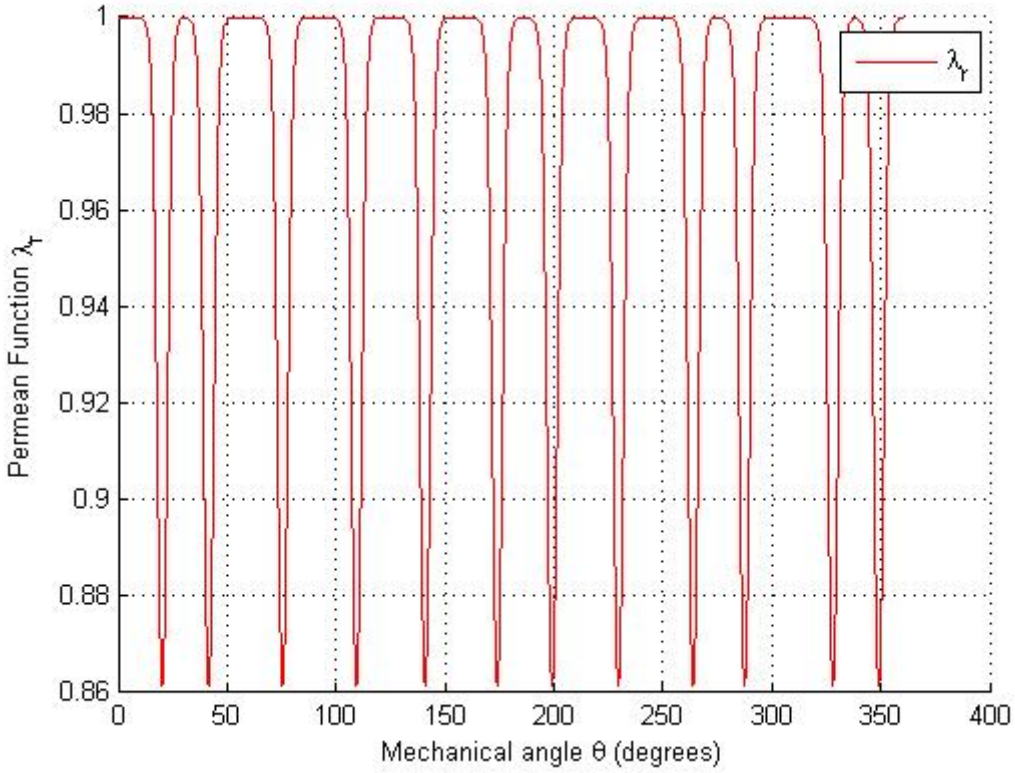

Fig. 2. Analytic Permeance function of optimal configuration.

Winding function[6] can be obtained by radial component of airgap flux density defined in (3)[7][8] .

$$W_f(\theta) = \frac{h+\delta}{I_f}\frac{B_r(\theta)}{\mu_0} \qquad (2)$$

$$B_r(\theta) = \sum_{n=1,3,5,..}^{\infty} \frac{B_r(\theta)}{\mu_r}\frac{4}{n\pi}\sin\left(\frac{n\pi\alpha_p}{2}\right)\cdot\frac{np}{(np)^2-1}\left[\left(\frac{R}{R_s}\right)^{np-1}\left(\frac{R_m}{R_s}\right)^{np+1}+\left(\frac{R_m}{R}\right)^{np+1}\right]$$
$$\times\left\{\frac{np-1+2\left(\frac{R_r}{R_m}\right)^{np+1}-(np+1)\left(\frac{R_r}{R_m}\right)^{2np}}{\frac{\mu_r+1}{\mu_r}\left[1-\left(\frac{R_r}{R_s}\right)^{2np}\right]-\frac{\mu_r-1}{\mu_r}\left[\left(\frac{R_m}{R_s}\right)^{2np}-\left(\frac{R_r}{R_m}\right)^{2np}\right]}\right\}\cos(np\theta) \qquad (3)$$

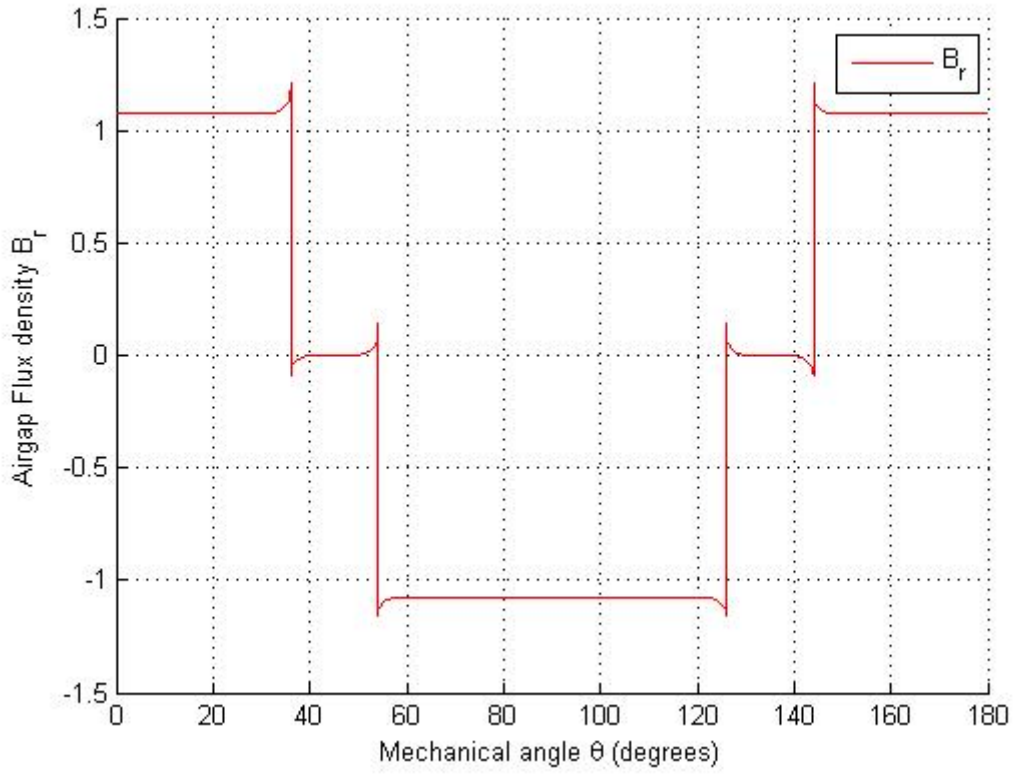

Fig. 3. Analityc Airgap radial Flux density(Slotless)

The program searches for the maximum in the vector | T_k | of cogging torque amplitudes and sets T_{peak} equal to such maximum value. The objective function T_{peak} thus calculated is then fed into the optimizer which, based on genetic algorithms, will appropriately decide the following vector of design variables ($\delta_1,\ldots\delta_{12}$) to be explored. The optimization process described has been implemented in the modeFrontier® environment [9] through the workflow diagram reported in Fig. 5. The workflow illustrates how the twelve input variables $\delta_1,\ldots\delta_{12}$ are separately treated and, at any optimization step, transferred into the input file. The application node, at each iteration, launches the MATLAB program which performs the cogging torque computation through the flowchart shown in Fig. 4. The MATLAB program writes the results (cogging samples) in an output file and the cogging torque absolute peak in a further file which is intended to contain the number to be minimized.

The overall optimization process employs the MOGA II algorithm (Modified Genetic Algorithm[9]). The inizialization of the optimization process is performed by a DOE (Design of Experiments) section which used the simplex algorithm to indentify the initial designs to be explored which form the set from which the genetic algorithm search is started.

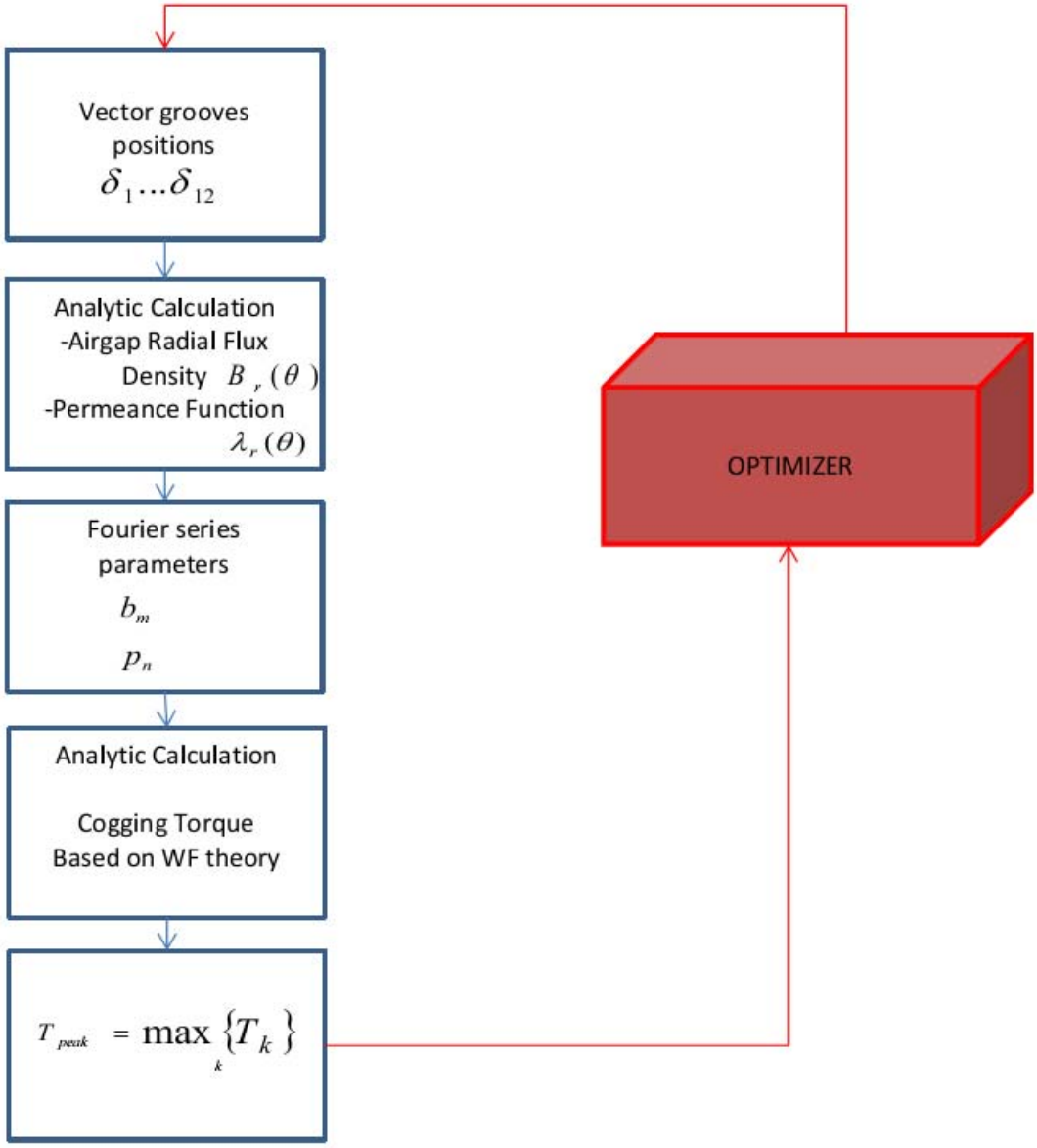

Fig. 4. Flow chart for the analytical calculation of the cogging torque by winding funtion method.

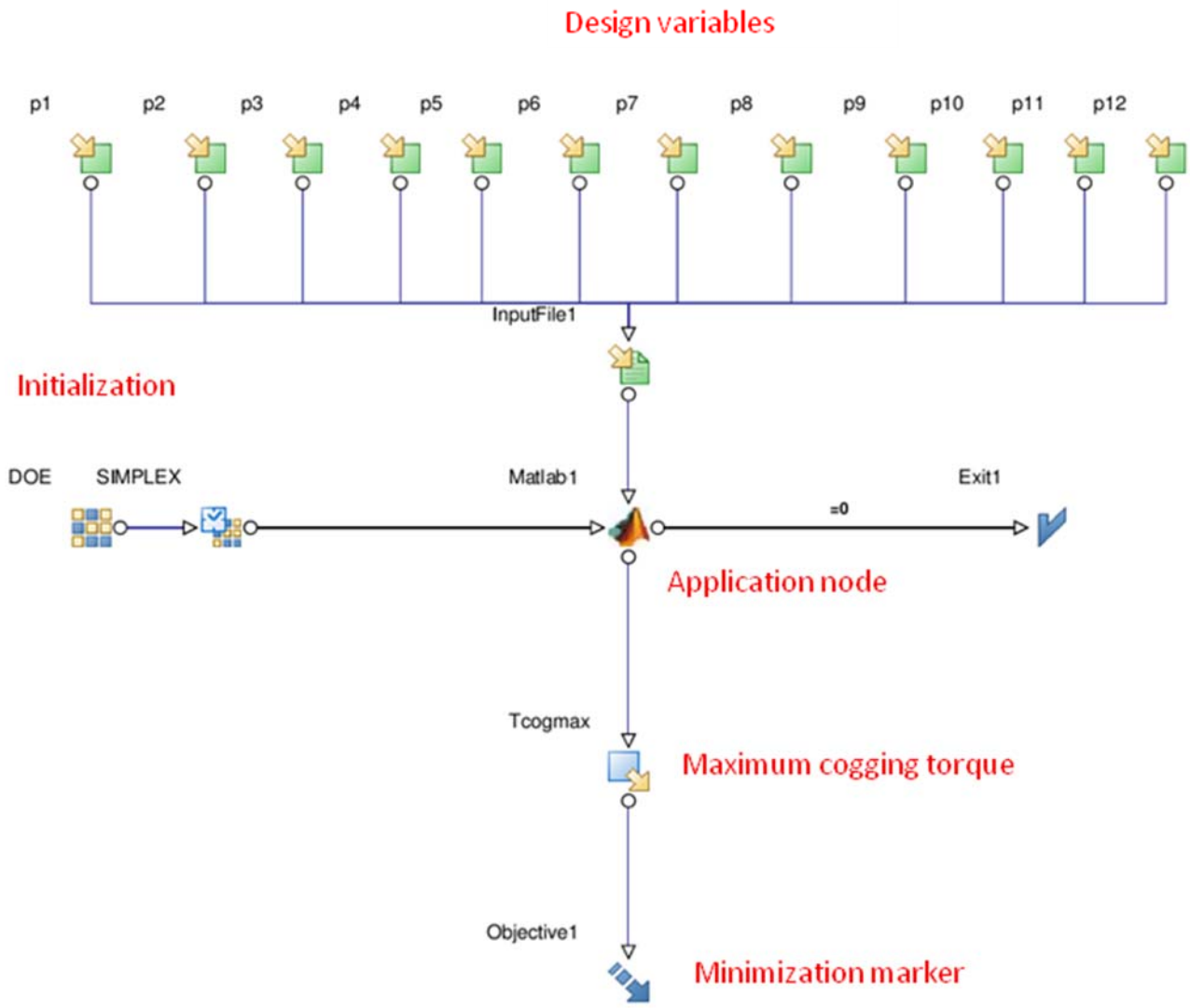

Fig. 5. Workflow that implements the optmization in the modeFrontier environment.

4.3 Optimization results

In the optimization process, more than one hundred configurations have been explored. Each configuration is simply called "design" and is assigned a progressive design ID. Each design is univocally determined by the order set of the twelve design variables $\delta_1,\ldots\delta_{12.}$

The diagram, in Fig. 6, can be used to visualize the optimization process output. It represents the cogging torque amplitudes computed for all the explored design, ordered by design ID. It can be seen that, as in the numerical analysis in chapter 3, at the beginning (low design ID values) the amplitudes are relatively high and quite randomly distributed. As the optimization process continues (i.e. for increasing design ID values), the genetic algorithm tends to select only the "fittest" designs, whose cogging torque amplitude, in fact, tends to a value around 110 Nm. This value can be treated as the lowest amplitude that can be achieved, provided that the optimization algorithm has worked properly identifying a

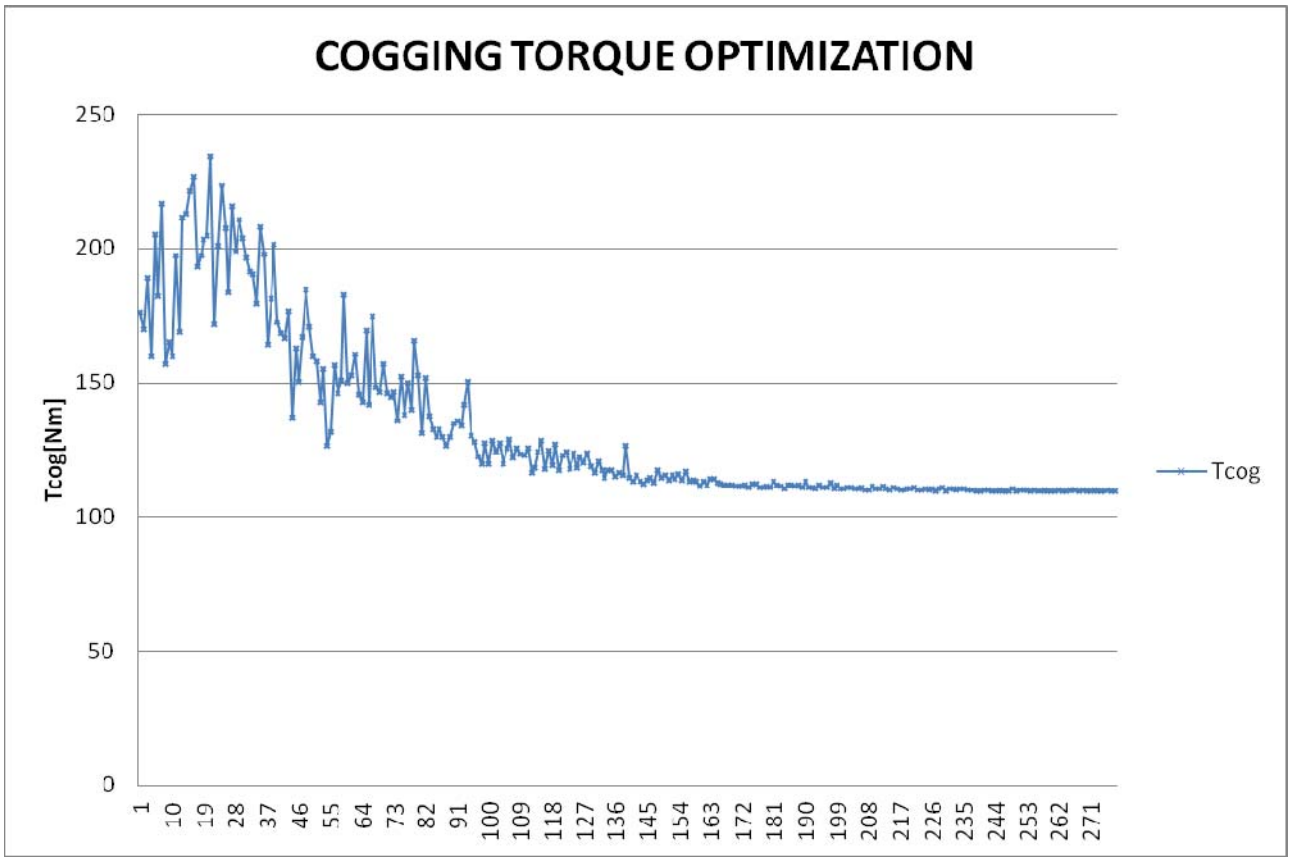

Fig. 6 Peak torque values found throughout the optimization and plotted versus design ID.

global and not only local minimum for the given problem.

For the sake of comparison, two design solutions are considered in the figure, i.e. the centered groove positions design (which gives the high torque ripple amplitude) and the optimal solution.

The cogging torque waveforms corresponding to the two designed mentioned above are reported in Fig. 9-10.

From a physical point of view, the optimal design determines a univocal distribution of groove positions around machine air-gap.

Such configuration is the one which can minimize the cogging torque.

It may be interesting to note that, as mentioned in the previous chapter, the optimal solution does not seem to be characterized by any particular recognizable pattern, which suggests that finding it without a genetic optimization program would not be possible or, at least, intuitive. Nevertheless, one can also observe from Fig. 10 one can see that the optimal solution leads to a surprisingly “regular” (i.e. periodic) cogging torque waveform, unlike non-optimal solutions.

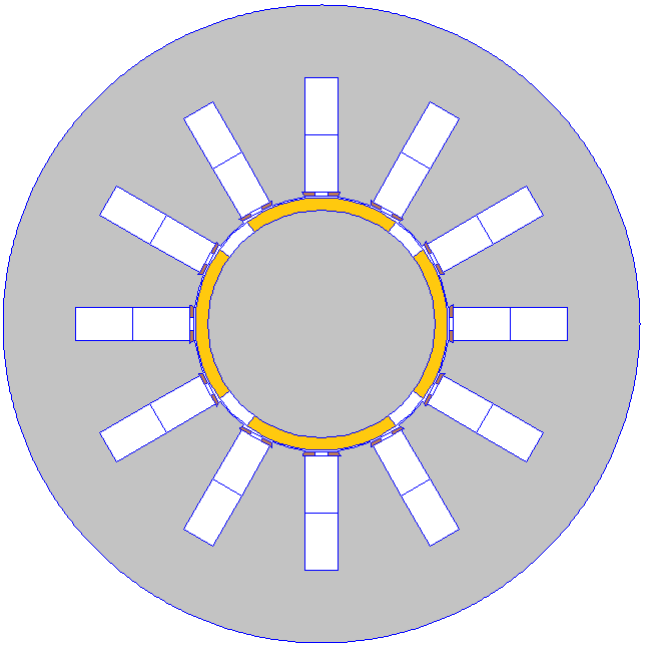

Fig. 7. Wedge grooves centered respect to the center of wedges connfiguration.

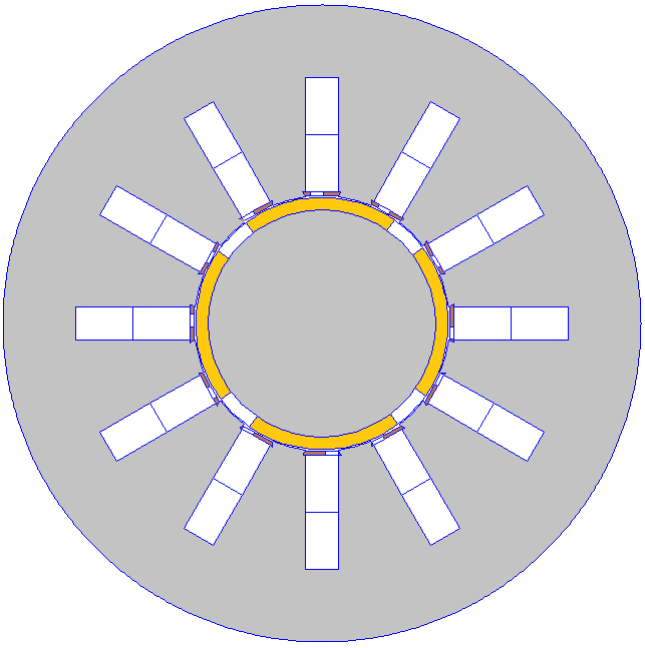

Fig. 8. optimal wedge grooves configuration.

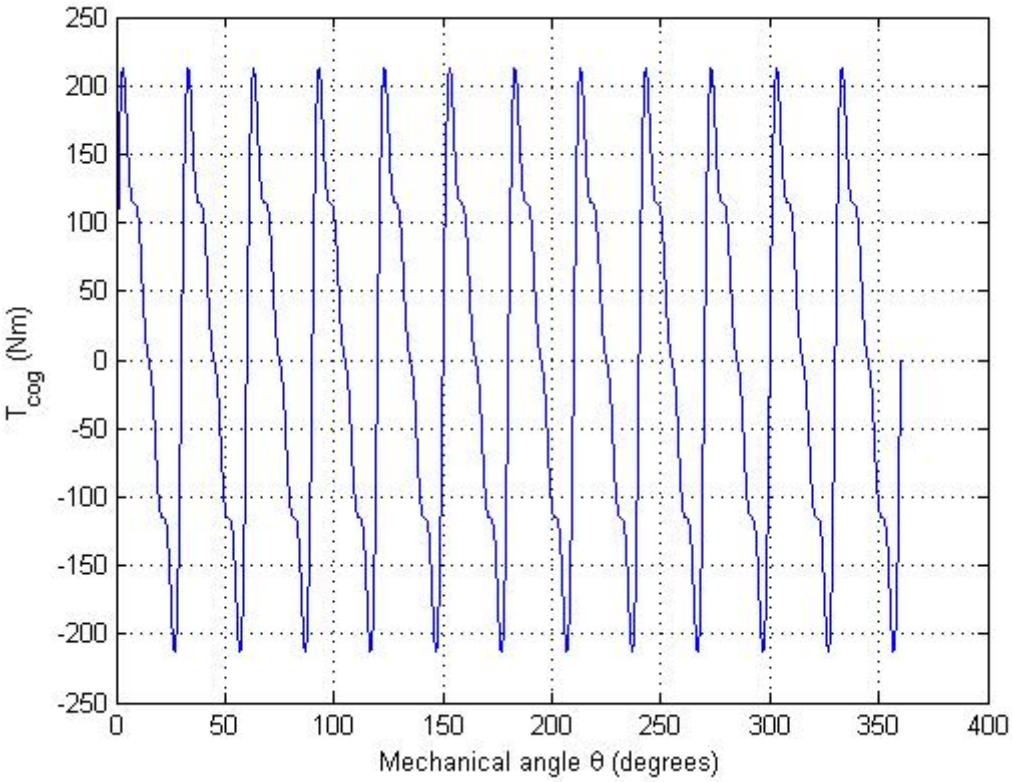

Fig. 9. Analytic Cogging torque of centered wedge grooves configuration

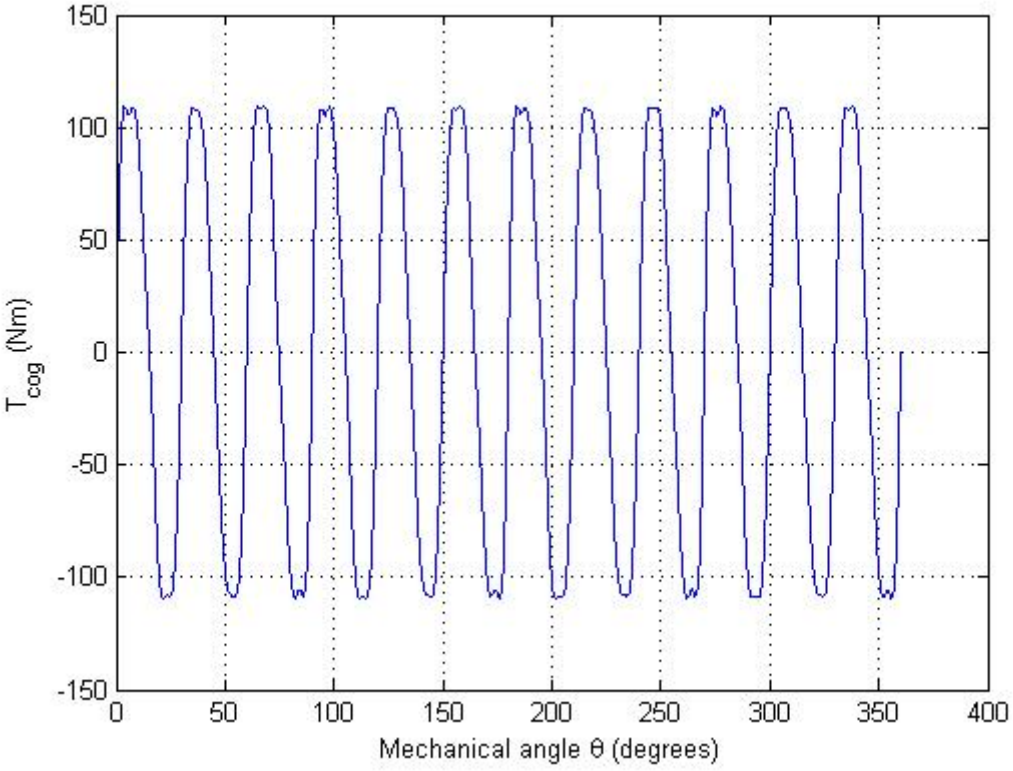

Fig. 10. analytic Cogging torque of optimal wedge grooves configuration

Also as shown in follows fig.(11-12-13) It can be seen really good agreement between the analytic an numerical Cogging Torque in optimal and no-optimal configuration.

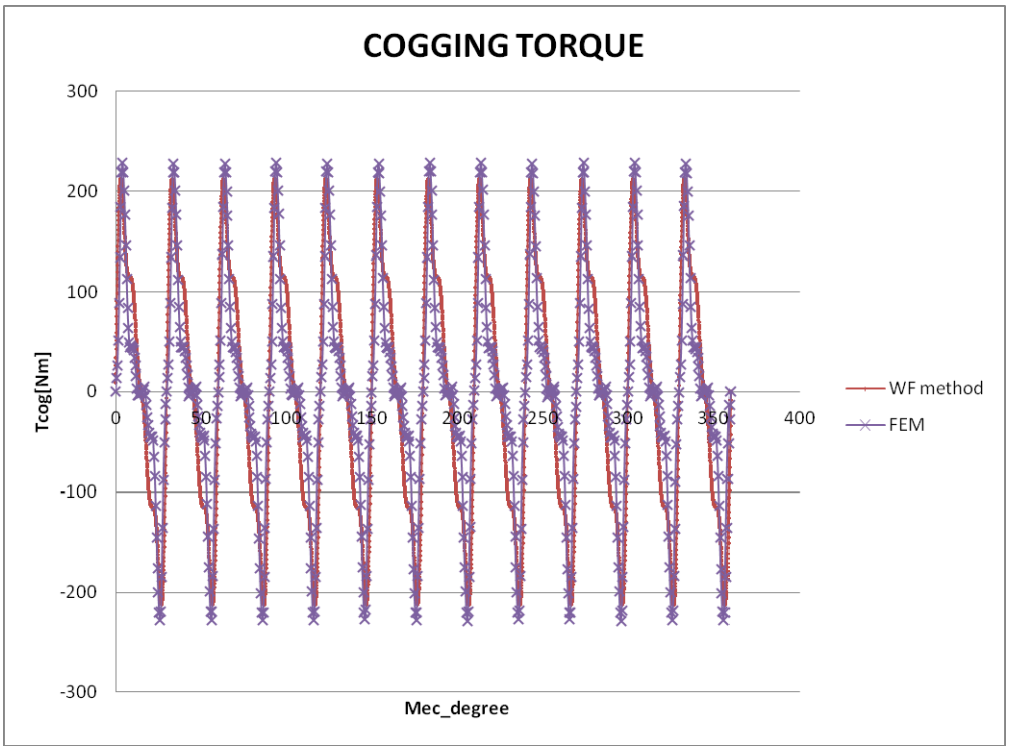

Fig. 11. Analytic and FEM Cogging torque comparison of centered wedge grooves configuration

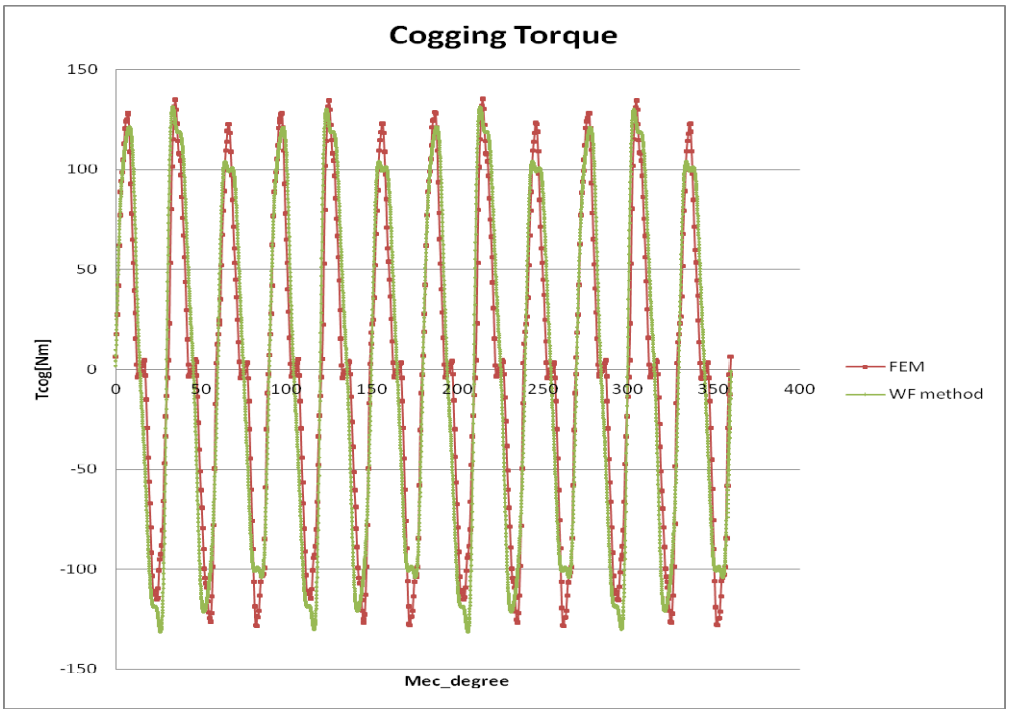

Fig. 12 Analytic and FEM Cogging torque comparison of one no-optimal configuration

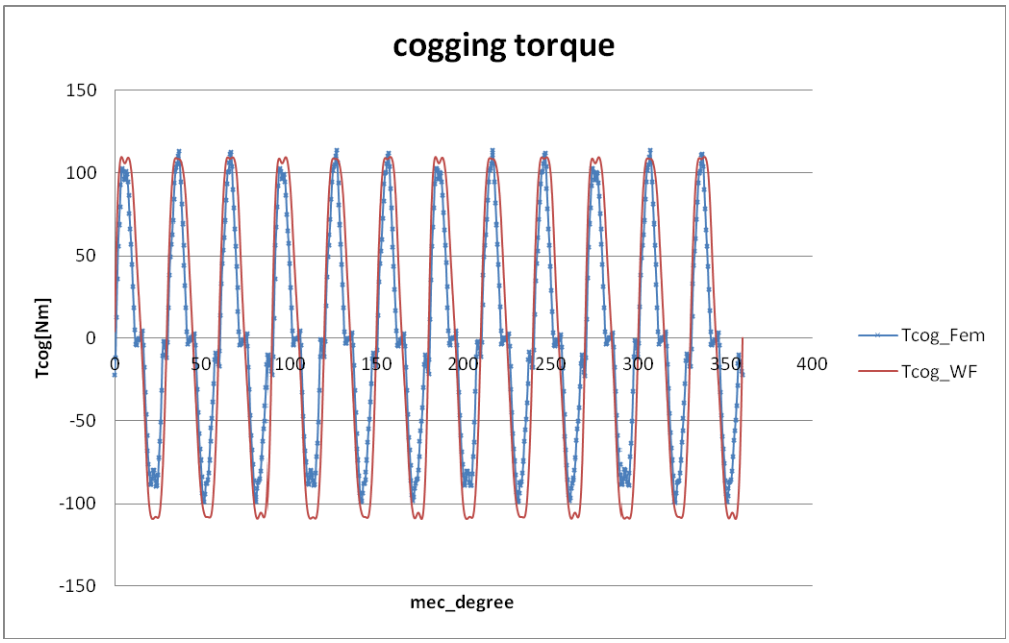

Fig. 13. Analytic and FEM Cogging torque comparison of optimal configuration

Fig. 14 shown the effect due to neglect permeability diffrence between wedge and lamination. The proposed method doesn't allow to consider it. Nevertheless This approximation does not imply a limit to the attainment of the objective. In fact the peak value of Cogging Torque is the same obtained in previous chapter (123Nm).

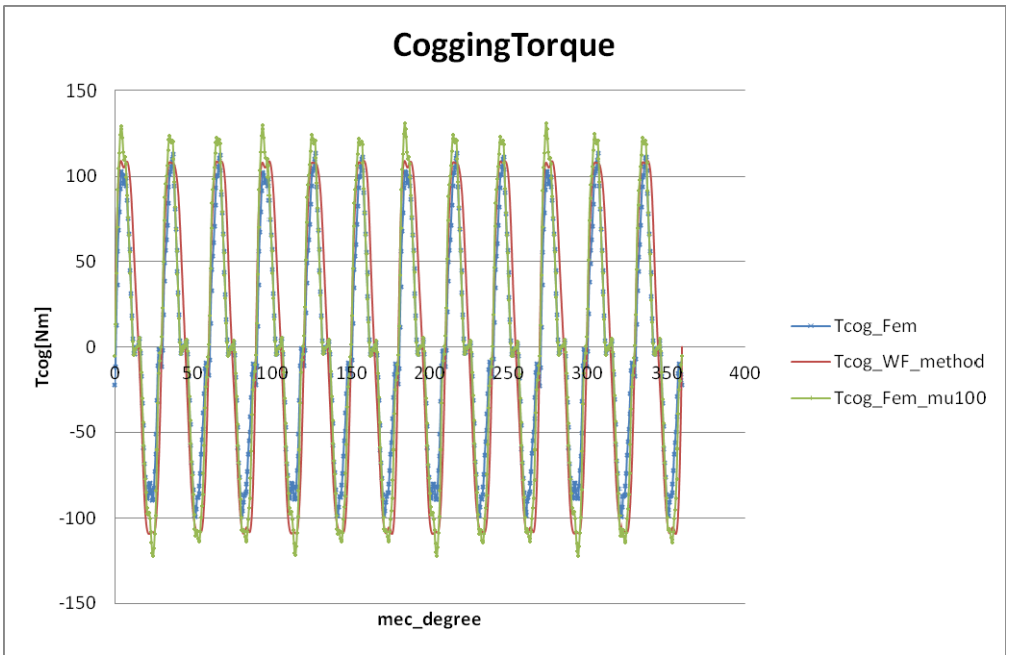

Fig. 14. Analytic μr=∞, FEM μr=∞ and FEM μr=100 Cogging torque comparison of optimal configuration

4.4 Conclusion

Cogging torque is a well known disadvantage of permanent-magnet machines, especially if designed with open stator slots. In [5], wedge design has been considered in more detail with the specific aim of finding its optimal design, which minimized the cogging torque amplitude. For this purpose, a genetic optimization algorithm, available in the modeFrontier software environment, has been employed. As a result of the optimization process, an optimal machine design with grooved wedges has been finally identified. In this chapter the numerical calculations of Cogging Torque has been replaced by analytical method .Which is quite accurate and it allow to obtain more rapidly results than numerical one. In addition the proposed method doesn't need a geometric machine model and it's enough few minutes to solve each iteration. This application has allowed once again to show performance of cogging torque analytical calculation method proposed on chapter 2.

Such optimal design does not exhibit any apparent feature such as to enable its recognition also without an optimization procedure. However, it has been also noted that the cogging torque waveform corresponding to the optimal design is not only the one with minimum amplitude, but also shows a periodic waveform which cannot be found, in general, in non-optimal design solutions.

4.5 References

[1]Y. Takeda, T. Yagisawa, A. Suyama, M. Yamamoto, "Application of magnetic wedges to large motors," IEEE Transactions on Magnetics, vol. 20, no. 5, pp. 1780- 1782, Sep 1984.

[2]Di Napoli, O. Honorati, E. Santini, L. Solero, “The use of soft magnetic materials for improving flux weakening capabilities of axial flux PM machines”, IEEE Industry Applications Society Annual Meeting 2000, Oct. 2000, vol. 1, pp. 8-12.

[3]Daohan Wang, Xiuhe Wang, Dongwei Qiao, Ying Pei; Sang-Yong Jung, "Reducing cogging torque in surface-mounted permanent-magnet motors by nonuniformly distributed teeth method", IEEE Transactions on Magnetics, vol.47, no.9, pp.2231-2239, Sept. 2011.

[4]F. Luise, A. Odorico, A. Tessarolo, “Extending the speed-range of surface permanent-magnet axial-flux motors by flux-weakening characteristic modification”, International Conference on Electric Machines, ICEM 2010, 6-9 Sept. 2010, Rome, Italy, CD-ROM paper RF-008893.

[5]A. Tessarolo, F. Luise, M. Mezzarobba, “A new magnetic wedge design for enhancing the performance of open-slot electric machines”, ESARS 2012.

[6]Tessarolo A. (2012, in press), “Accurate Computation of Multiphase Synchronous Machine Inductances Based on Winding Function Theory”, *IEEE Transactions on Energy Conversion*.

[7]Z. Q. Zhu, Member, David Howe, Ekkehard Bolte, and Bemd Ackermann (1993), “Instantaneous Magnetic Field Distribution in Brushless Permanent Magnet dc Motors, Part I: Open-circuit Field”, *IEEE Transactions on Magnetics*, vol. 29, no. 1.

[8]Z. Q. Zhu, David Howe (1993), “Instantaneous Magnetic Field Distribution in Brushless Permanent Magnet dc Motors, Part III: Effect of Stator Slotting”, *IEEE Transactions on Magnetics*, vol. 29, no. 1.

[9]Zarko, D., Ban, D., Lipo, T.A. (2008), “Analytical Solution for Cogging Torque in Surface Permanent-Magnet Motors Using Conformal Mapping”, *IEEE Transactions on Magnetics,* vol. 44, no. 1, pp. 52-65

5 Analytical Calculation of the No-Load Flux Density in the Stator Core of Slotless SPM Machines

5.1 Introduction

Surface Permanent Magnet (SPM) machines may be equipped with either a slotted or slotless stator core. In the latter case, the stator laminations form a ferromagnetic hollow cylinder whose inner surface is smooth. To this surface, stator coils are attached, instead of being embedded in slots as in the ordinary construction. The slotless stator design leads to a lower power density compared to the slotted one and is used where some parasitic effects relating to the slotting effects are to be eliminated. Typical examples of such parasitic effects are the cogging torque and rotor additional losses. The minimization or cancelation of the cogging torque is required, for instance, in some wind generators in order to let them work even at very small torque and speed values. Additional loss minimization, on the other side, may be required in some very high-efficiency high-speed applications.

Thanks to the absence of teeth, slotless SPM machine geometry allows for a relatively easy analytical solution for the magnetic fields in active parts. Formulations of the magnetic field in the air-gap due to both permanent magnets and armature windings have been presented. In this chapter, an analytical exact formulation is derived for the flux density in the stator core of unsaturated SPM slotless machines. The solution is derived based on the analytical expression of the vector potential in the air-gap by solving the Laplace's differential equation for the vector potential in the core domain subject to suitable boundary conditions. The accuracy of the results obtained is assessed by comparison with finite element analysis.

This chapter also shows how the formulation derived can be used for the analytical computation of no-load core losses of SPM slotless machines including rotational eddy current effects.

Finally, it is empathized that the same methodology described in the chapter can be used to analytically find stator core flux density due to armature windings and, therefore, the overall flux density at any load condition.

5.2 Geometrical modeling of slotless permanent magnet machines

A typical schematic geometry of a slotless SPM machine is shown in Fig. 1. For the purpose of the chapter, the geometry can be characterized by the dimensions shown in Fig. 2, i.e.:

R_o stator outer radius
R_r rotor core outer radius
R_m radius at permanent magnet external surface
R_s stator bore radius
τ_{pm} permanent magnet span.

A magnet coverage c is also introduced as the ratio between the magnet span and the pole span τ_p:

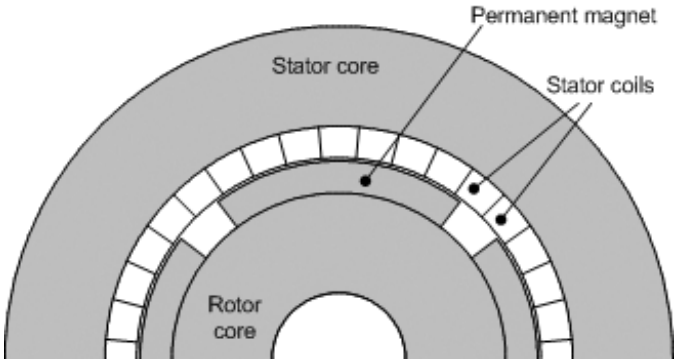

Fig. 1. Geometry of a slotless SPM machine.

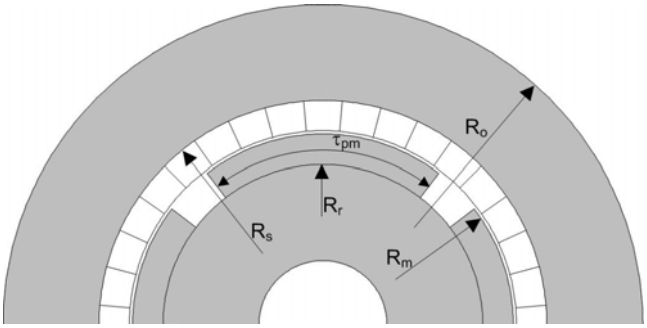

Fig. 2. Characteristic dimensions for a slotless SPM machine.

$$c = \frac{\tau_m}{\tau_p} \qquad (1)$$

The assumption made to solve the field analytically in the active parts of the machine is the stator and rotor cores are subject to negligible magnetic saturation.

Furthermore, end effects are neglected, i.e. the flux density distribution is supposed to be the same over any machine cross section. This implies that the magnetic vector potential inside the machine is anywhere oriented axially and can be treated to a scalar.

Permanent magnets are supposed to be radially magnetized with uniform magnetization.

5.3 Analytical Solution for the no-load airgap field

An analytical formula for the air-gap field produced by permanent magnets can be found by solving the 2-D Poisson's equation:

$$\frac{1}{r}\frac{\partial}{\partial r}\left(r\frac{\partial A_g}{\partial r}\right)+\frac{1}{r^2}\frac{\partial^2 A_g}{\partial^2 \theta} = \frac{1}{\mu_r} div(\mathbf{M}) \qquad (2)$$

where μ_r is permanent magnet relative permeability, r and θ are the radial and azimuthal coordinate in a polar coordinate system centered on machine axis, A is (the axial component of) the vector potential and **M** is the magnetization vector. Outside permanent magnets, the magnetization vector (and therefore its

divergence) is zero; inside radially-magnetized permanent magnets, the magnetization vector is radially oriented and has uniform amplitude given by:

$$|\mathbf{M}| = H_c \mu_r \frac{h+\delta}{h+\mu_r \delta} \cong H_c \mu_r \qquad (3)$$

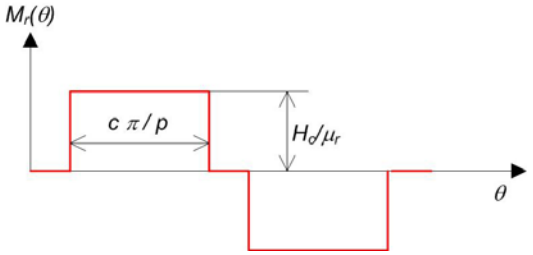

Fig. 3. Radial component of the magnetization as a function of the azimuthal angle along an arbitrary circumference of radius r between R_r and R_m.

where H_c is permanent magnet coercivity, $h=R_m-R_r$ is permanent magnet height and $\delta=R_s-R_m$ [approximation (3) holds because relative permeability μ_r is always very close to unity]. Hence the radial magnetization component M_r along any circumference of radius between R_r and R_m has the diagram shown in Fig. 3 for a machine with p pole pairs, while the tangential component is zero anywhere. Therefore, the divergence inside permanent magnets is:

$$div(\mathbf{M}) = \frac{M_r}{r} + \frac{\partial M_r}{\partial r} + \frac{1}{r}\frac{\partial M_\theta}{\partial \theta}$$
$$= \sum_{n=1,3,5,..} \frac{2H_c \mu_r c}{r} \frac{\sin(n\pi c/2)}{n\pi c/2} \cos(np\theta) \qquad (4)$$

Using (4), Poisson's equation (2) can be solved analytically by separation of variables for the vector potential A_g. In particular, the radial flux density in the gap region not occupied by permanent magnets [i.e. for the region where $R_m \le r \le R_s$ and where div($\mathbf{M}$)=0] can be found from A_g as:

$$B_{gr}(r,\theta) = \frac{1}{r}\frac{\partial A_g}{\partial \theta} = \sum_n K_n f_n(r) \cos(pn\theta) \qquad (4)$$

where:

$$K_n = \frac{\mu_0 M_n}{\mu_r} \frac{np\left(\frac{R_m}{R_s}\right)^2 - \left(\frac{R_r}{R_s}\right)^2 \left[np + 2\ln\frac{R_m}{R_r}\right]}{\frac{1+\mu_r}{\mu_r}\left[1-\left(\frac{R_r}{R_s}\right)^2\right] - \frac{\mu_r - 1}{\mu_r}\left[\left(\frac{R_m}{R_s}\right)^2 - \left(\frac{R_r}{R_m}\right)^2\right]} \qquad (5)$$

$$f_n(r) = 1 + \left(\frac{R_s}{r}\right)^2 \qquad (6)$$

if np=1 and

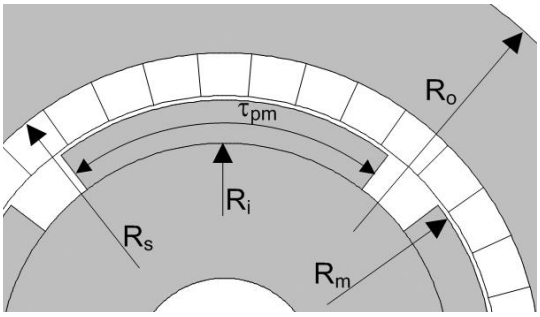

Fig. 2. Characteristic dimensions for a slotless SPM machine.

$$K_n = \frac{\mu_0 M_n}{\mu_r} \frac{np}{n^2 p^2 - 1} \frac{(np-1) + 2\left(\frac{R_r}{R_m}\right)^{np+1} - \left(\frac{R_r}{R_m}\right)^{2np} (np+1)}{\frac{1+\mu_r}{\mu_r}\left[1 - \left(\frac{R_r}{R_s}\right)^{2np}\right] - \frac{\mu_r - 1}{\mu_r}\left[\left(\frac{R_m}{R_s}\right)^{2np} - \left(\frac{R_r}{R_m}\right)^{2np}\right]} \tag{7}$$

$$f_n(r) = \left(\frac{r}{R_s}\right)^{np-1}\left(\frac{R_m}{R_s}\right)^{np+1} + \left(\frac{R_m}{r}\right)^{np+1} \tag{8}$$

if $np \neq 1$.

As a preliminary verification, the air-gap flux density computed by (4)-(8) is assessed against FE analysis on a sample machine geometry characterized by the data given in Table I.

TABLE I

R_r	50 mm	R_o	100 mm
R_m	59.5 mm	μ_r	1.04
R_s	70 mm	H_c	850 kA/m
c	0.917	p	1

As can be seen the matching is definitely satisfactory. The FE solution in Fig. 4 exhibits a ripple-like effect in the permanent magnet region due to the fact that, in the FE model, the radially magnetized magnet had to be approximated as a

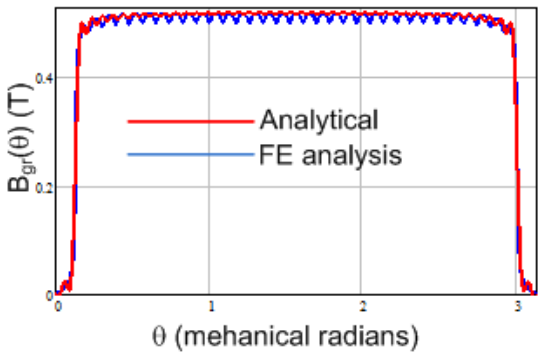

Fig. 4. Comparison of the air-gap radial flux density computed analytically and by FE analysis over a pole span at radius r = 60 mm.

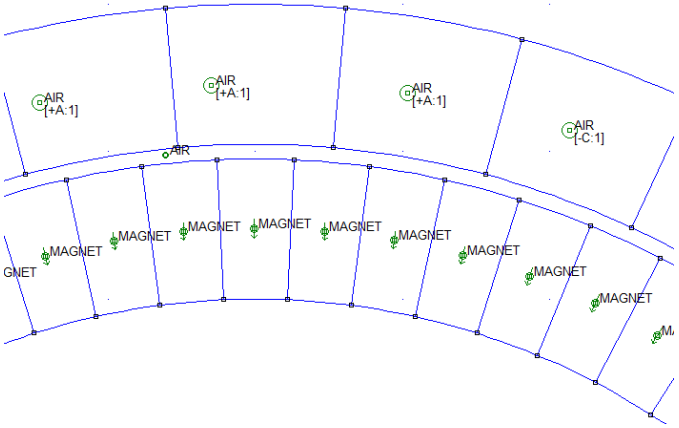

Fig. 5. Modeling of radially magnetized permanent magnets as a sequence of elementary magnets with parallel magnetization.

set of magnets with parallel magnetization for numerical reasons.

5.4 Analytical Solution for flux density inside the stator core

To determine the flux density inside the stator core, the Laplace's equation for the vector potential A_c in the core is first written as:

$$\frac{1}{r}\frac{\partial}{\partial r}\left(r\frac{\partial A_c}{\partial r}\right)+\frac{1}{r^2}\frac{\partial^2 A_c}{\partial^2 \theta}=0 \qquad (9$$

Assuming that separation of variables technique can be used, the general solution has the form:

$$A_c(r,\theta)=\sum_{n=1,3,5,\ldots}\left(A_{c,n}^{+}r^{np}+A_{c,n}^{-}r^{-np}\right)\sin\left(np(\theta-\alpha)\right) \quad (10)$$

for any set of coefficients $A_{c,n}^{+}$, $A_{c,n}^{-}$, α. These coefficients can be determined by imposing boundary conditions. On the stator bore surface (r=R_s), the boundary condition is written considering that the radial flux density component is continuous across the inner stator surface, hence:

$$B_{cr}(R_s,\theta)=\frac{1}{r}\frac{\partial A_c}{\partial \theta}=$$

$$=\sum_{n=1,3,5,\ldots} np\left(A_{c,n}^{+}R_s^{\,np-1}+A_{c,n}^{-}R_s^{\,-np-1}\right)\cos\left(np\left(\theta-\alpha\right)\right)=B_{gr}(R_s,\theta) \quad (11)$$

where B_{cr} indicates the radial flux density in the stator core and B_{gr} the radial flux density in the gap, given by (4).

On the outer stator surface (r=R_o), the Dirichlet boundary conditions (meaning that flux lines are tangent to the external rotor surface) is imposed, i.e.:

$$A_c(R_o,\theta)=\sum_{n=1,3,5,\ldots}\left(A_{c,n}^{+}R_o^{\,np}+A_{c,n}^{-}R_o^{\,-np}\right)\sin\left(np\left(\theta-\alpha\right)\right)=0 \quad (12)$$

From (11) and (12) the unknown coefficients can be found. In particular, α needs to be zero when the polar axis is at θ=0 [which is asumed in (4)]. Otherwise, α represents the polar axis position in the stator reference frame where angles θ are defined.

As to coefficients $A_{c,n}^{+}$, $A_{c,n}^{-}$ the expression they must take to satisfy (11) and (12) is shown below:

$$A_{c,n}^{+}=-\frac{R_s^{\,np+1}}{np\left(R_o^{\,2np}-R_s^{\,2np}\right)}K_n f_n(R_s) \quad (13)$$

$$A_{c,n}^{-}=\frac{R_s^{\,np+1}R_o^{\,2np}}{np\left(R_o^{\,2np}-R_s^{\,2np}\right)}K_n f_n(R_s) \quad (14)$$

with K_n and f_n given by (5)-(8).

Once the vector potential has been determined, the tangential and radial flux density components in the core are immediately known as:

$$B_{cr}(r,\theta)=\frac{1}{r}\frac{\partial A_c}{\partial \theta}=\sum_{n=1,3,5,\ldots} np\left(A_{c,n}^{+}r^{np-1}+A_{c,n}^{-}r^{-np-1}\right)\cos\left(np\left(\theta-\alpha\right)\right) \quad (15)$$

$$B_{ct}(r,\theta)=\frac{\partial A_c}{\partial \theta}=-\sum_{n=1,3,5,\ldots} np\left(A_{c,n}^{+}r^{np-1}-A_{c,n}^{-}r^{-np-1}\right)\sin\left(np\left(\theta-\alpha\right)\right) \quad (16)$$

where α is the polar axis position in the stator reference frame.

The flux density magnitude in the core can be derived from (15)-(16) as:

$$B_c(r,\theta) = \sqrt{B_{cr}(r,\theta)^2 + B_{ct}(r,\theta)^2} =$$

$$= np\sqrt{\left[\sum_{n=1,3,5,\ldots}\left(A_{c,n}^{+} r^{np-1} + A_{c,n}^{-} r^{-np-1}\right)\cos\left(np(\theta-\alpha)\right)\right]^2 +}$$

$$\sqrt{\sum_{n=1,3,5,\ldots}\left[\left(A_{c,n}^{+} r^{np-1} - A_{c,n}^{-} r^{-np-1}\right)\sin\left(np(\theta-\alpha)\right)\right]^2} \quad (17)$$

5.5 FE Validations

The derived formulas for the flux density in the core are assessed by comparison with FE results obtained on the two-pole machine whose data are provided in Table I.

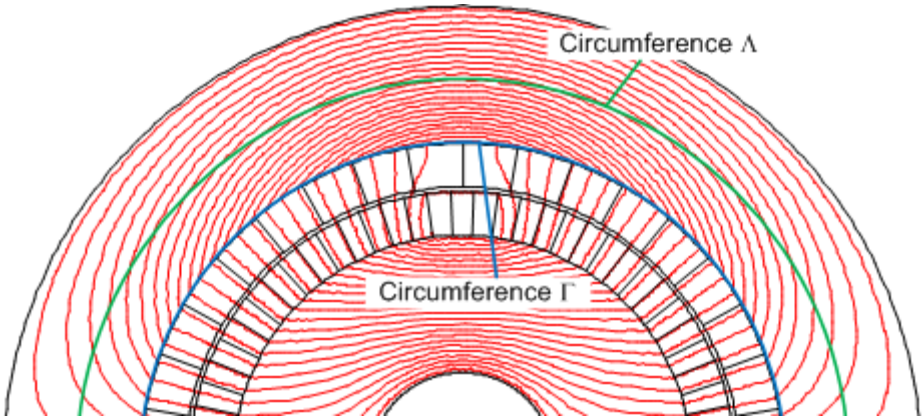

Fig. 6. Positions of circumferences Γ and Λ on which flux density components from FE analysis and analytical computation are compared.

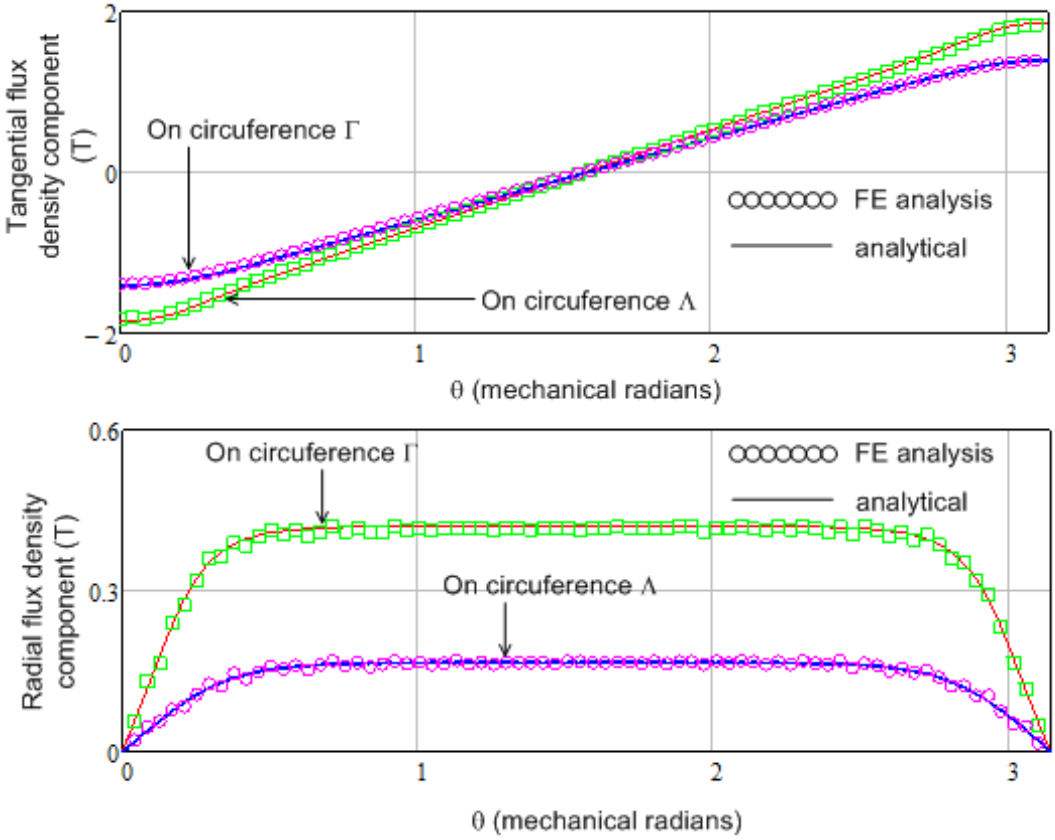

Fig. 7. Comparison of the flux density components in the yoke computed by FE analysis and through the formulas derived.

The comparison is made between flux density values computed by FE analysis and with the analytical formulas above on the two circumferences Γ and Λ shown in Fig. 6: Γ is the stator bore circumference, Λ is the mean yoke circumference.

The comparison is shown in Fig. 7, where a very good agreement between the two methods employed can be observed.

5.6 Application to No-Load Core Loss Evaluation

The knowledge of the flux density values in the stator core in the form of an analytical formula can serve different purposes. Among the other things, it helps compute core losses without FE analysis.

According to [6], the no-load core losses due to the fundamental flux density can be estimated as:

$$P_c = \int_{R_s}^{R_o} \int_{0}^{2\pi} \left[k_H f\, B(r,\theta)^{\alpha} + k_E f^2\, B(r,\theta)^2 \right] \gamma\, \rho\, r\, d\theta\, dr \quad (18)$$

where:

k_H	is the hysteresis loss coefficient
k_E	is the eddy-current loss coefficient
α	is the exponential hysteresis coefficient
$\gamma(r,\theta)$	is the rotational loss coefficient
ρ	is lamination density

The rotational loss coefficient γ at a given core point having coordinates r, θ can be determined as a function of trakectory described by the flux density vector at that point. In general, such trajectory is an ellipse. In fact, let us consider the fundamental flux densities (designated with subscript "1") according to (15)-(16):

$$B_{cr1}(r,\theta) = p\left(A_{c,1}^{+}r^{p-1} + A_{c,1}^{-}r^{-p-1}\right)\cos\left(p(\theta-\alpha)\right) \quad (19)$$

$$B_{ct1}(r,\theta) = -p\left(A_{c,1}^{+}r^{p-1} - A_{c,1}^{-}r^{-p-1}\right)\sin\left(p(\theta-\alpha)\right) \quad (20)$$

Squaring (19)-(20) them we obtain:

$$B_{cr1}{}^{2}(r,\theta) = p^2\left(A_{c,1}^{+}r^{p-1} + A_{c,1}^{-}r^{-p-1}\right)^2\cos\left(p(\theta-\alpha)\right)^2 \quad (21)$$

$$B_{ct1}{}^{2}(r,\theta) = p^2\left(A_{c,1}^{+}r^{p-1} - A_{c,1}^{-}r^{-p-1}\right)^2\left[1-\cos\left(p(\theta-\alpha)\right)^2\right] \quad (22)$$

By substitution of (21) into (22) we obtain that the tangential and radial flux density components must satisfy the equation:

$$\frac{B_{ct1}{}^{2}}{p^2\left(A_{c,1}^{+}r^{p-1} - A_{c,1}^{-}r^{-p-1}\right)^2} + \frac{B_{cr1}{}^{2}}{p^2\left(A_{c,1}^{+}r^{p-1} + A_{c,1}^{-}r^{-p-1}\right)^2} = 1 \quad (23)$$

which is the equation of an ellipse having axes equal to

$$a(r) = p\left|A_{c,1}^{+}r^{p-1} - A_{c,1}^{-}r^{-p-1}\right| \quad (24)$$

$$b(r) = p\left|A_{c,1}^{+}r^{p-1} + A_{c,1}^{-}r^{-p-1}\right| \quad (25)$$

Equations (24)-(25) clearly show that the shape of the ellipse described by the flux density vector point (Fig. 8) depends only on the radial coordinate r.

The rotational loss coefficient appearing in (18) can be thus evaluated for any radius r as a function of the axes of the flux density ellipse at that radius, i.e.:

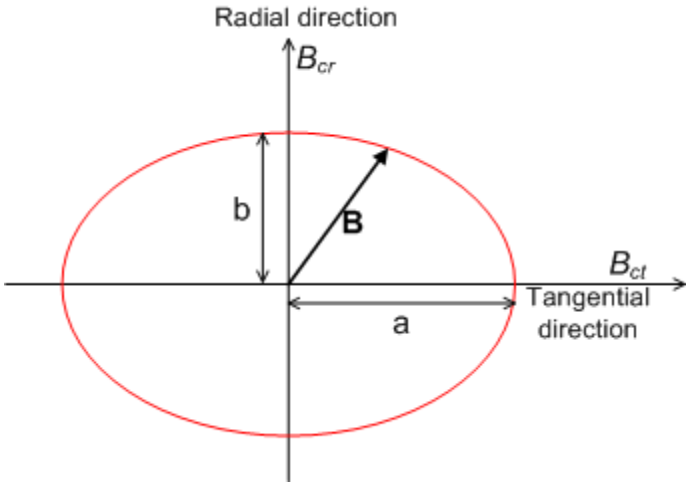

Fig. 8. Ellipse described by the point of the flux density vector **B** in a given point of the stator core.

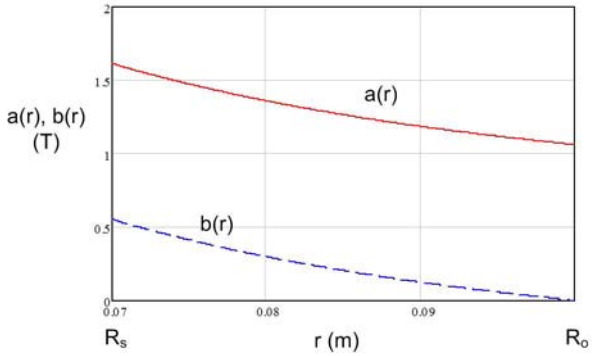

Fig. 9. Flux density ellipse axes computed analytically as a function of the radius in the stator core.

$$\gamma = \gamma\left(\max\left(a(r),b(r)\right), \frac{\min\left(a(r),b(r)\right)}{\max\left(a(r),b(r)\right)}\right) \quad (26)$$

A diagram of the function γ is provided in [6].

An example of analytical computation of the flux density ellipse axes in the stator core is provided in Fig. 9, which implements equations (24)-(25) for the machine whose data are given in Table I. In particular, it can be seen how the ellipses axis in the radial direction (b) tends to zero as the radius r approach the outer stator radius R_o. In fact, at r=R_o a purely tangential flux density (Dirichlet condition) has been imposed.

5.7 Extension to Analytical coumputation of the core Flux Density due to Armature Currents

The methodology described in this chapter can be naturally extended for the computation of the flux density that originates in the slotless stator core due to armature currents. For this purpose, one can start from the armature reaction field analytical expression in the air-gap domain and use the flux density values on the stator bore circumference as a boundary condition to solve Laplace's equation in the core domain.

5.8 Conclusion

In this chapter an analytical expression has been derived for the no-load flux density in the stator core of a slotless SPM machine. The expression has been derived by solving Laplace's equation in the core domain and applying suitable boundary conditions. The expression has been verified by comparison with FE analysis results on a sample machine and found to be extremely accurate. Finally, the use of the derived formula for the computation of no-load core losses has been discussed. In particular, it has been shown how, using the proposed analytical approach, rotational eddy current effects can be easily taken into account in the core loss computation. Extension of the computation method proposed to the core flux density due to armature currents has been finally discussed.

5.9 References

[1] Zhu, Z.Q.; Howe, D.; Chan, C.C.; , "Improved analytical model for predicting the magnetic field distribution in brushless permanent-magnet machines," Magnetics, IEEE Transactions on, vol.38, no.1, pp.229-238, Jan 2002.D

[2] Atallah, K.; Zi Qiang Zhu; Howe, D.; , "Armature reaction field and winding inductances of slotless permanent-magnet brushless machines," Magnetics, IEEE Transactions on, vol.34, no.5, pp.3737-3744, Sep

1998.

[3] Pfister, P.-D.; Perriard, Y.; , "Slotless Permanent-Magnet Machines: General Analytical Magnetic Field Calculation," Magnetics, IEEE Transactions on, vol.47, no.6, pp.1739-1752, June 2011.

[4] Tessarolo, A.; Luise, F.; Raffin, P.; Venuti, V.; , "Multi-objective design optimization of a surface permanent-magnet slotless alternator for small power wind generation," Clean Electrical Power (ICCEP), 2011 International Conference on, vol., no., pp.371-376, 14-16 June 2011.

[5] Luise, F.; Tessarolo, A.; Pieri, S.; Raffin, P.; Di Chiara, M.; Agnolet, F.; Scalabrin, M.; , "Design and technology solutions for high-efficiency high-speed motors," Electrical Machines (ICEM), 2012 XXth

International Conference on, vol., no., pp.157-163, 2-5 Sept. 2012.

[6] Komeza, K.; Dems, M.; , "Finite-Element and Analytical Calculations of No-Load Core Losses in Energy-Saving Induction Motors," Industrial Electronics, IEEE Transactions on, vol.59, no.7, pp.2934-2946, July 2012.

[7] Tessarolo, A.; Agnolet, F.; Luise, F.; Mezzarobba, M.; , "Use of Time-Harmonic Finite-Element Analysis to Compute Stator Winding Eddy-Current Losses Due to Rotor Motion in Surface Permanent-Magnet Machines," Energy Conversion, IEEE Transactions on, vol.27, no.3, pp.670-679, Sept. 2012.

6 A Compact Analytical Expression for the Load Torque in Surface Permanent-Magnet Machines with Slotless Stator Design

6.1 Introduction

Surface Permanent Magnet (SPM) machines may be equipped with either a slotted or slotless stator core [1], [2], [3]. In the latter case, the stator laminations form a ferromagnetic hollow cylinder whose inner surface is smooth. Stator coils are attached to this surface, instead of being embedded in slots as in the ordinary construction.

The slotless stator design leads to a lower power density compared to the slotted one and is used where some parasitic effects relating to the slotting effects are to be eliminated. Typical examples of such parasitic effects are the cogging torque and rotor additional losses. The minimization or cancelation of the cogging torque is required, for instance, in some wind generators in order to let them work even at very small torque and speed values [4]. Additional loss minimization, on the other side, may be required in some very high-efficiency high-speed applications [5].

Thanks to the absence of teeth, slotless SPM machine geometry allows for a relatively easy analytical solution for the magnetic fields in active parts [3]. Formulations of the magnetic field in the air-gap due to both permanent magnets and armature windings have been presented [1], [2]. In this chapter, an analytical exact formulation is derived for the load torque of slotless SPM machines. The proposed formula has the advantage of explicitly showing how machine torque relates to every single construction detail, i.e. to active part dimensions and permanent magnet characteristics. Therefore, it can be of practical usefulness in the dimensioning and design optimization stage as a fast alternative to time-consuming Finite Element (FE) analysis [4], [5].

With respect to the existing literature, the method proposed in the chapter for torque computation does not rely on Maxwell's stress tensor technique [1]-[3] (which is known to lead to quite involved formulation) but employs an alternative approach where rotor permanent magnets are modeled as equivalent current sheet [7]. Such a modeling makes it possible to compute the force acting on them (and thus the rotor torque) from the vector product of the armature reaction field and the equivalent current density representing permanent magnets.

6.2 Geometric Model of Slotless Spm Machines

A typical schematic geometry of a slotless SPM machine is shown in Fig. 1. For the purpose of the chapter, the geometry can be characterized by the dimensions shown in Fig. 2, i.e.:

R_w	winding inner radius
R_r	rotor core outer radius
R_m	outer permanent magnet radius
R_s	stator bore radius
τ_{pm}	permanent magnet span

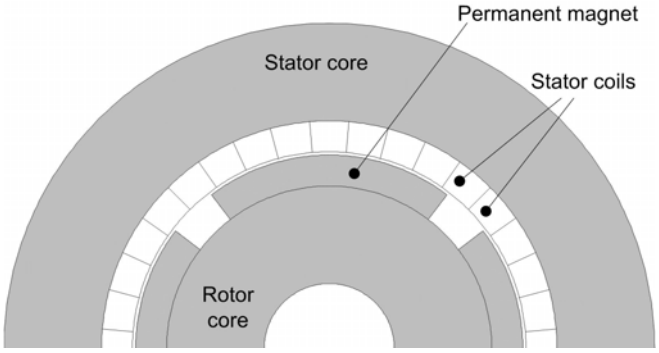

Fig. 1. Geometry of a slotless SPM machine.

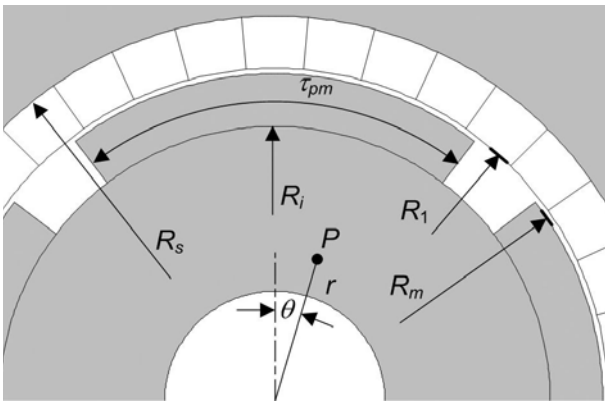

Fig. 2. Characteristic dimensions for a slotless SPM machine.

A magnet coverage c is also introduced as the ratio between the magnet span and the pole span τ_p:

$$c = \tau_m / \tau_p \quad (1)$$

The assumption made to solve the field analytically in the air-gap is that stator and rotor cores are subject to negligible magnetic saturation. Furthermore, end effects are neglected, i.e. the flux density distribution is supposed to be the same over any machine cross section. This implies that the magnetic vector potential inside the machine is anywhere oriented axially and can be treated as a scalar.

Permanent magnets are supposed to be radially magnetized with uniform magnetization. They are characterized through a relative permeability μ_r and a coercivity H_c. Residual flux density is thereby determined as $\mu_0\mu_r H_c$ where $\mu_0=4\pi\times10^{-7}$ H/m is air magnetic permeability.

The stator coils are supposed to be organized in a single-layer three-phase winding arrangement (as in usual construction 0, 0) where each phase has a 60-electrical-degrees span (phase belt). In each phase belt, a uniform current density distribution is assumed.

Currents in phases a, b, c are supposed to be sinusoidal and shifted by 120 electrical degrees in time, so that

$$i_a(t) = I\cos(\omega t) \quad (2)$$

$$i_b(t) = I\cos(\omega t - 2\pi/3) \quad (3)$$

$$i_c(t) = I\cos(\omega t - 4\pi/3) \quad (4)$$

The winding is characterized by the following data:

N_c	number of turns per coil
p	number of pole pairs
q	number of coils per pole per phase
I	peak phase current
ω	stator current pulsation
b	number of parallel ways per phase

For machine field analysis, a polar coordinate system (r,θ) is introduced where a generic point *P* in the machine cross section is identified with a radius vector of length *r* starting from rotation axis and forming an angle θ with the vertical as shown in Fig. 2. One phase belt of phase "*a*" is assumed centered at θ=0.

6.3 Geometric Model of Slotless Spm Machines

Based on the assumptions and definitions fixed in previous section, the procedure followed in this chapter for analytical load torque derivation consists of the following steps:

-The armature reaction field due to stator currents over time is computed analytically by solving Maxwell equation for the magnetic vector potential in the air-gap domain. The accuracy of the computation is checked by comparison with FE analysis.

-Permanent magnets are modeled through appropriate current sheets. The surface current required for exactly modeling their effect is calculated and the accuracy of the modeling approach is verified by FE analysis.

-The instantaneous torque is computed as resulting from the interaction between the armature reaction field and the equivalent current sheets introduced to model permanent magnets. The derived torque expression is checked against FE analysis.

The three steps mentioned above will be developed in next sections.

6.4 Computation of Armature Reaction Field

The armature reaction field in the air-gap domain is first computed. By air-gap domain in this context reference is made to all the machine region not occupied by ferromagnetic cores; the air-gap in this sense therefore includes permanent magnet and stator winding regions as well.

The armature reaction field is being computed by solving Maxwell equation for the magnetic vector potential in the air-gap domain. The field solution in the winding region ($R_1 \le r \le R_s$) is indicated in the following by subscript "*w*", while the solution in the remaining part of the air-gap (mainly occupied by permanent magnets, $R_i \le r \le R_1$) will be denoted by subscript "*m*".

If only stator current energize the machine, the vector potential in the winding and permanent magnet domain (A_w, A_m, respectively), satisfy the following differential equations in polar coordinates r, θ:

$$\nabla A_w = \frac{1}{r}\frac{\partial}{\partial r}\left(r\frac{\partial A_w}{\partial r}\right)+\frac{1}{r^2}\frac{\partial^2 A_w}{\partial^2 \theta} = -\mu_0 J(\theta,t) \quad (5)$$

$$\text{for } R_1 \le r \le R_s$$

$$\nabla A_m = \frac{1}{r}\frac{\partial}{\partial r}\left(r\frac{\partial A_m}{\partial r}\right)+\frac{1}{r^2}\frac{\partial^2 A_m}{\partial^2 \theta} = 0 \quad (6)$$

$$\text{for } R_i \le r \le R_1$$

where $J(\theta, t)$ indicates the current density at instant t at angular position θ in the winding region.

Solving (5)-(6) enables one to find the radial and tangential components of the flux density in the winding region (B_{wr}, $B_{w\theta}$) as well as the radial and tangential components of the flux density in the permanent magnet region (B_{mr}, $B_{m\theta}$) as follows:

$$B_{wr} = \frac{1}{r}\frac{\partial A_w}{\partial \theta}, \quad B_{w\theta} = \frac{\partial A_w}{\partial r} \quad (7)$$

$$\text{for } R_1 \le r \le R_s$$

$$B_{mr} = \frac{1}{r}\frac{\partial A_m}{\partial \theta}, \quad B_{m\theta} = \frac{\partial A_m}{\partial r} \quad (8)$$

$$\text{for } R_i \le r \le R_1$$

6.4.1 Definition of current density function

The current density function $J(\theta, t)$ is a piece-wise constant function that accounts for the current density being uniform over each phase belt. By simple geometric considerations, it can be shown that the function $J(\theta, t)$ can be expressed as the following series expansion:

$$J(\theta,t) = \sum_{h=1,7,13,19,\ldots} J_h \cos(ph\theta - \omega t) + \sum_{k=5,11,17,23,\ldots} J_k \cos(pk\theta + \omega t) \quad (9)$$

where coefficients J_n, for any odd positive integer n, have the form:

$$J_n = \frac{36}{\pi^2} \frac{N_c I\, p\, q}{b\left(R_s^{\,2} - R_1^{\,2}\right)} \frac{\sin\left(\frac{\pi n}{6}\right)}{n} \quad (10)$$

Indices k and h in (7) respectively take odd integer values given by $k=6q+1$ (with $q=0, 1, 2, \ldots$) and $h=6q-1$ (with $q=1, 2, 3, \ldots$).

Fig. 3 shows the plot of current density function $J(\theta, t)$ for a two-pole machine over a double pole span ($0 \le \theta \le 2\pi$) at three instants of time, namely at $t=0$, $t=T/12$ and $t=T/6$, where T is the period of stator currents ($T=2\pi/\omega$). The data of the sample SPM slotless machine taken into account to draw the plots in Fig. 3 are reported in Table I.

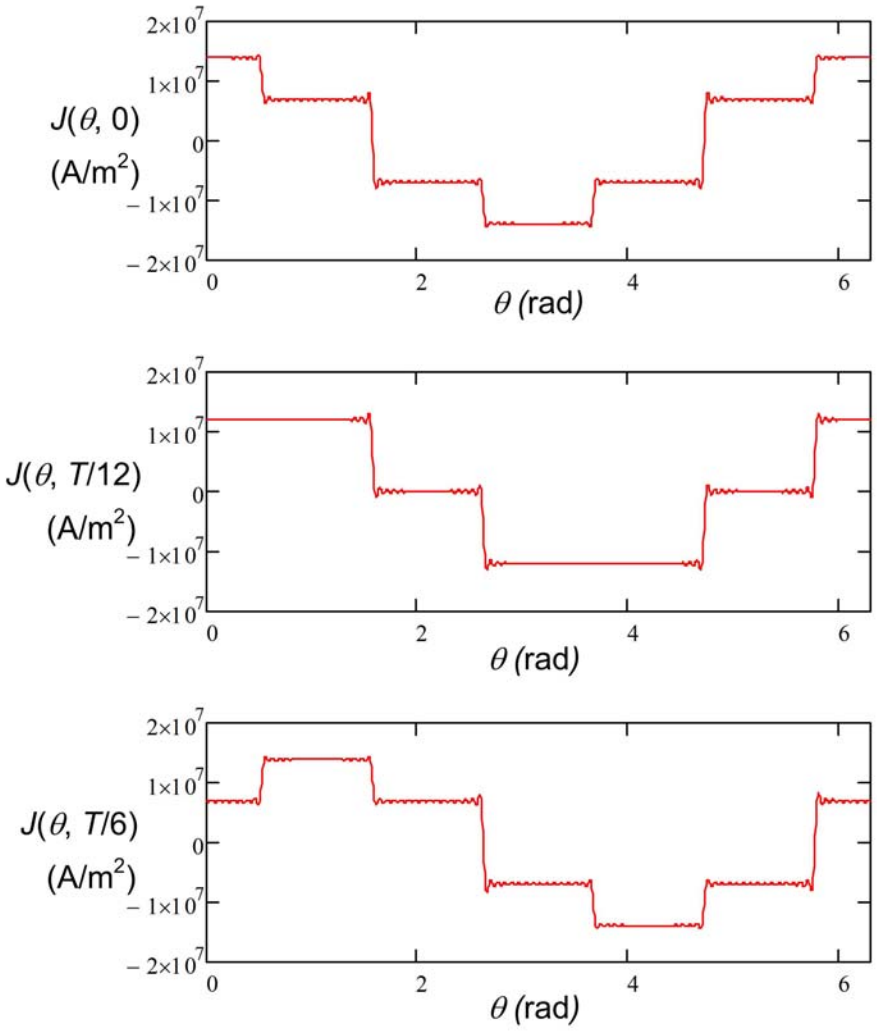

Fig. 3. Current density function plot over a two-pole span at time t=0, t=T/12 and t=T/6.

TABLE I. SAMPLE SPM SLOTLESS MACHINE DATA			
q	6	μ_r	1.05
p	1	H_c	850×10^{3} A/m
I	1500 A	L	80.0×10^{-3} m
N_c	1	R_i	50.0×10^{-3} m
b	1	R_1	60.5×10^{-3} m
R_i	0.050 m	R_s	70.0×10^{-3} m
f	50 Hz	c_m	0.917

6.4.2 Definition of current density function

Once the current density function has been defined as discussed in the previous subsection, what is still required to solve differential equations (5)-(6) is to define suitable boundary conditions. Two homogeneous Neumann boundary conditions can be established on the outer and inner air-gap circumferences (at radii $r=R_i$ and $r=R_s$), imposing that the flux density must have zero tangential component on them (due to the assumed infinite core permability):

$$B_{w\theta}\big|_{r=R_s} = \left.\frac{\partial A_w}{\partial r}\right|_{r=R_s} = 0 \quad (11)$$

$$B_{m\theta}\big|_{r=R_i} = \left.\frac{\partial A_m}{\partial r}\right|_{r=R_i} = 0 \quad (12)$$

for any θ. Two further boundary conditions can be fixed by imposing that the flux density must be continuous at $r=R_1$ in both its radial and tangential components:

$$B_{w\theta}\big|_{r=R_1} = \left.\frac{\partial A_w}{\partial r}\right|_{r=R_1} = B_{m\theta}\big|_{r=R_1} = \left.\frac{\partial A_m}{\partial r}\right|_{r=R_1} \quad (13)$$

$$B_{wr}\big|_{r=R_1} = \frac{1}{R_1}\left.\frac{\partial A_w}{\partial \theta}\right|_{r=R_1} = B_{mr}\big|_{r=R_1} = \frac{1}{R_1}\left.\frac{\partial A_m}{\partial \theta}\right|_{r=R_1} \quad (14)$$

6.4.3 General solution for air-gap magnetic potential

To determine the vector potential in the air-gap domain, boundary conditions (11)-(14) are to be applied to the general solutions of (5)-(6). By separation of variables, such general solutions can be expressed as follows:

$$A_w(r,\theta,t) =$$

$$= \sum_{h=5,11,17,\ldots} \left(A^{+}_{w,h} r^{hp} + A^{-}_{w,h} r^{-hp} + A^{\circ}_{w,h} r^{2}\right)\cos\left(hp\theta + \omega t\right)$$

$$+ \sum_{k=1,7,13,\ldots} \left(A^{+}_{w,k} r^{kp} + A^{-}_{w,k} r^{-kp} + A^{\circ}_{w,k} r^{2}\right)\cos\left(kp\theta - \omega t\right) \quad (15)$$

$$A_m(r,\theta,t) =$$

$$= \sum_{h=5,11,17,\ldots} \left(A^{+}_{m,h} r^{hp} + A^{-}_{m,h} r^{-hp} \right) \cos\left(hp\theta + \omega t \right)$$

$$+ \sum_{k=1,7,13,\ldots} \left(A^{+}_{m,k} r^{kp} + A^{-}_{m,k} r^{-kp} \right) \cos\left(kp\theta - \omega t \right) \quad (16)$$

where $A^{+}_{w,n}$, $A^{-}_{w,n}$, $A^{\circ}_{w,n}$, $A^{+}_{m,n}$, $A^{-}_{m,n}$ are suitably defined constants.
By direct substitution and partial derivative expansion, one can prove that (15)-(16) always satisfy (5)-(6) on condition that, for any odd integer *n*, the constant $A^{\circ}_{w,n}$ is defined as:

$$A^{\circ}_{w,n} = -\frac{\mu_0 J_n}{4 - n^2} \quad (17)$$

6.4.4 Solution for the air-gap magnetic vector potential

The only action to determine the magnetic vector potential in the air-gap domain is to fix the constants $A^{+}_{w,n}$, $A^{-}_{w,n}$, $A^{+}_{m,n}$, $A^{-}_{m,n}$ for any odd integer *n*. This can be done by imposing boundary conditions (11)-(14).
Substitution of (15)-(16) into (11)-(14) gives in fact:

$$\sum_{h=5,11,17,\ldots} \left(hpA^{+}_{w,h} R_s^{\,hp-1} - hpA^{-}_{w,h} R_s^{\,-hp-1} + 2A^{\circ}_{w,h} R_s \right) \cos\left(hp\theta + \omega t \right)$$

$$+ \sum_{k=1,7,13,\ldots} \left(kpA^{+}_{w,k} R_s^{\,kp-1} - kpA^{-}_{w,k} R_s^{\,-kp-1} + 2A^{\circ}_{w,k} R_s \right) \cos\left(kp\theta - \omega t \right) = 0 \quad (18)$$

$$\sum_{h=5,11,17,\ldots} \left(hpA^{+}_{m,h} R_i^{\,hp-1} - hpA^{-}_{m,h} R_i^{\,-hp-1} \right) \cos\left(hp\theta + \omega t \right)$$

$$+ \sum_{k=1,7,13,\ldots} \left(kpA^{+}_{m,k} R_i^{\,kp-1} - kpA^{-}_{m,k} R_i^{\,-kp-1} \right) \cos\left(kp\theta - \omega t \right) = 0 \quad (19)$$

$$\sum_{h=5,11,17,\ldots} \left(hpA^{+}_{w,h} R_1^{\,hp-1} - hpA^{-}_{w,h} R_1^{\,-hp-1} + 2A^{\circ}_{w,h} R_1 \right) \cos\left(hp\theta + \omega t \right)$$

$$+ \sum_{k=1,7,13,\ldots} \left(kpA^{+}_{w,k} R_1^{\,kp-1} - kpA^{-}_{w,k} R_1^{\,-kp-1} + 2A^{\circ}_{w,k} R_1 \right) \cos\left(kp\theta - \omega t \right)$$

$$= \sum_{h=5,11,17,\ldots} \left(hpA^{+}_{m,h} R_1^{\,hp-1} - hpA^{-}_{m,h} R_1^{\,-hp-1} \right) \cos\left(hp\theta + \omega t \right)$$

$$+ \sum_{k=1,7,13,\ldots} \left(kpA^{+}_{m,k} R_1^{\,kp-1} - kpA^{-}_{m,k} R_1^{\,-kp-1} \right) \cos\left(kp\theta - \omega t \right) = 0 \quad (20)$$

$$- \sum_{h=5,11,17,\ldots} hp \left(A^{+}_{w,h} R_1^{\,hp-1} + A^{-}_{w,h} R_1^{\,-hp-1} + A^{\circ}_{w,h} R_1 \right) \sin\left(hp\theta + \omega t \right)$$

$$- \sum_{k=1,7,13,\ldots} kp \left(A^{+}_{w,k} R_1^{\,kp-1} + A^{-}_{w,k} R_1^{\,-kp-1} + A^{\circ}_{w,k} R_1 \right) \sin\left(kp\theta - \omega t \right)$$

$$= - \sum_{h=5,11,17,\ldots} hp \left(A^{+}_{m,h} R_1^{\,hp-1} + A^{-}_{m,h} R_1^{\,-hp-1} \right) \sin\left(hp\theta + \omega t \right)$$

$$- \sum_{k=1,7,13,\ldots} kp \left(A^{+}_{m,k} R_1^{\,kp-1} + A^{-}_{m,k} R_1^{\,-kp-1} \right) \sin\left(kp\theta - \omega t \right) = 0 \quad (21)$$

Since (18)-(21) must hold for any θ and t, they imply the following equalities:

$$npA^{+}_{w,n} R_s^{\,np-1} - npA^{-}_{w,n} R_s^{\,-np-1} + 2A^{\circ}_{w,n} R_s = 0 \quad (22)$$

$$A^{+}_{m,n} R_i^{\,np-1} - A^{-}_{m,n} R_i^{\,-np-1} = 0 \qquad (23)$$

$$npA^{+}_{w,n} R_1^{\,np-1} - npA^{-}_{w,n} R_1^{\,-np-1} + 2A^{\circ}_{w,n} R_1 =$$

$$= npA^{+}_{m,n} R_1^{\,np-1} - npA^{-}_{m,n} R_1^{\,-np-1} \qquad (24)$$

$$A^{+}_{w,n} R_1^{\,np-1} + A^{-}_{w,n} R_1^{\,-np-1} + A^{\circ}_{w,n} R_1 =$$

$$= A^{+}_{m,n} R_1^{\,np-1} + A^{-}_{m,n} R_1^{\,-np-1} \qquad (25)$$

to be satisfied for any odd integer n. Equations (22)-(25) constitute a linear system of equations in the unknowns $A^{+}_{w,n}$, $A^{-}_{w,n}$, $A^{+}_{m,n}$, $A^{-}_{m,n}$ [$A^{\circ}_{w,n}$ are still known from (17)]. Such a system can be solved yielding:

$$A^{+}_{w,n} = \frac{\mu_0 J_n}{2n(R_s^{\,2n} - R_i^{\,2n})} \left[\frac{R_s^{\,n+2} - R_i^{\,2n} R_1^{\,2-n}}{2-n} + \frac{R_s^{\,n+2} - R_1^{\,2+n}}{2+n} \right] \quad (26)$$

$$A_{w,n}^{-} = \frac{\mu_0 J_n}{2n(R_i^{-2} - R_s^{-2n})}\left[\frac{R_s^{2-n} - R_i^{-2n} R_1^{2+n}}{2+n} + \frac{R_s^{2-n} - R_1^{2-n}}{2-n}\right] \quad (27)$$

$$A_{m,n}^{+} = \frac{(A_{w,n}^{-} + A_{w,n}^{+} R_1^{2n})(n^2-4) + \mu_0 J_n R_1^{n+2}}{(R_1^{2n} + R_i^{2n})(n^2-4)} \quad (28)$$

$$A_{m,n}^{-} = \frac{(A_{w,n}^{-} + A_{w,n}^{+} R_1^{2n})(n^2-4) + \mu_0 J_n R_1^{n+2}}{(R_1^{2n} + R_i^{2n})(n^2-4)} R_i^{n+2} \quad (29)$$

6.4.5 Air-gap flux linkage determination

Once coefficients in (15)-(16) are fully determined through (17) and (26)-(29), the flux density in the air gap can be computed from (7)-(8) at any point (r, θ) and at any instant of time t. In particular, what will be used for torque computation is only the radial flux density component in the permanent magnet region (B_{mr}), whose explicit expression in therefore provided explicitly below:

$$B_{mr}(r,\theta,t) = \frac{1}{r}\frac{\partial A_m}{\partial \theta}(r,\theta,t) =$$

$$= -\sum_{h=5,11,17,\ldots} hp\left(A_{m,h}^{+} r^{hp-1} + A_{m,h}^{-} r^{-hp-1}\right)\sin\left(hp\theta + \omega t\right)$$

$$-\sum_{k=1,7,13,\ldots} kp\left(A_{m,k}^{+} r^{kp-1} + A_{m,k}^{-} r^{-kp-1}\right)\sin\left(kp\theta - \omega t\right) \quad (30)$$

The accuracy of the expression found for the radial magnetic field is assessed against FE analysis. Comparisons between analytical and FE results are made on the sample SPM slotless machine whose data are provided in Table I. The comparison is made at two instant of times, namely at t=0 and t=T/12, being T the period of stator currents given by (2)-(4). The FE analysis solution referring to the two instants of time are provided in Fig. 4 and Fig. 6 respectively. In the same figures, three contours are shown where the radial flux density values resulting from FE analysis and analytical computation are compared. The comparison shows a very good matching between analytical and FE-computed results.

6.5 Modeling Permanent Magnets with Equivalent Current Sheets

In order to facilitate load torque computation, the approach proposed in this chapter consists of replacing each

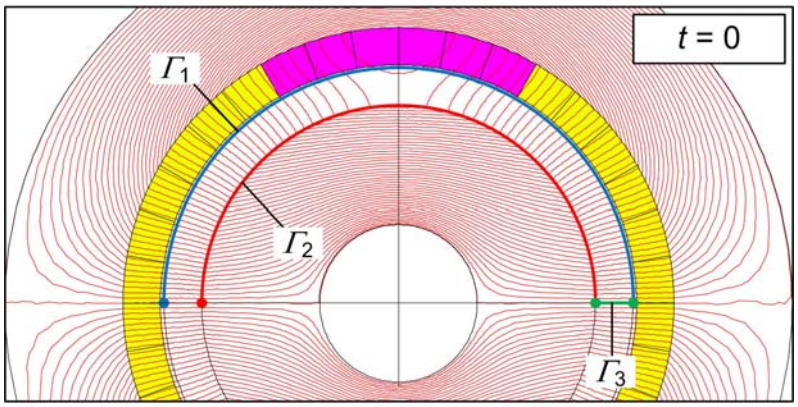

Fig. 4. FE analysis output for the sample SPM slotless machine at instant $t=T/12$, when conductors in magenta carry a current I and conductors in yellow carry a current $-I/2$.

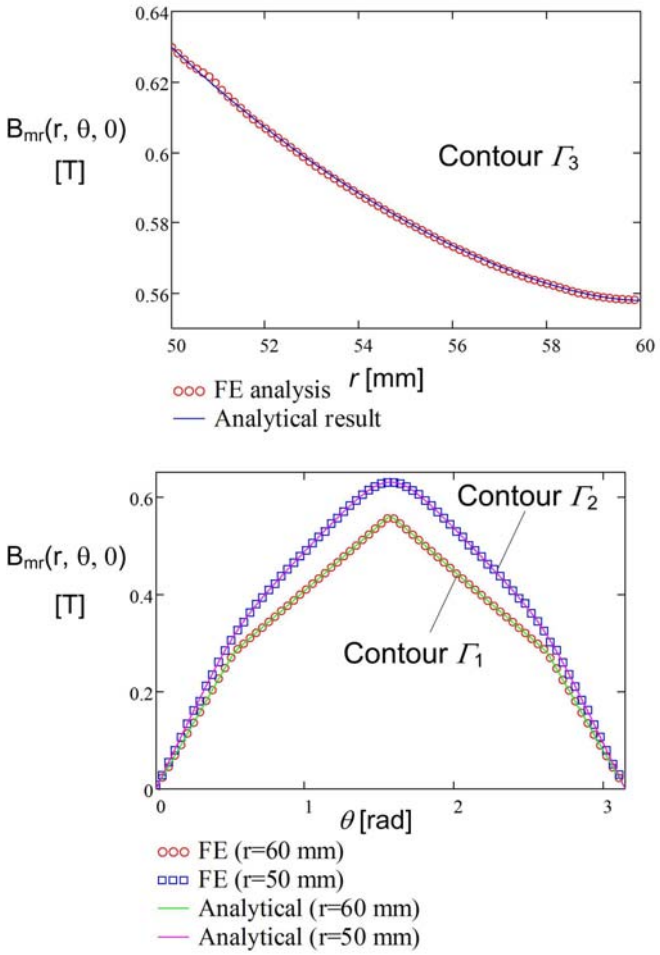

Fig. 5. Radial flux density plotted over contours Γ_1, Γ_2, Γ_3 (Fig. 4) at instant $t=0$, according to analytical calculation and FE analysis.

permanent magnet with a couple of current sheets capable of generating exactly the same field. The concept is illustrated in Fig. 8, which shows how the permanent magnet with uniform radial magnetization M is replaced by a surface current density j_s flowing through its radially-oriented sides.

The equivalent current density j_s has the same value as the radial magnetization M 0, hence we can write:

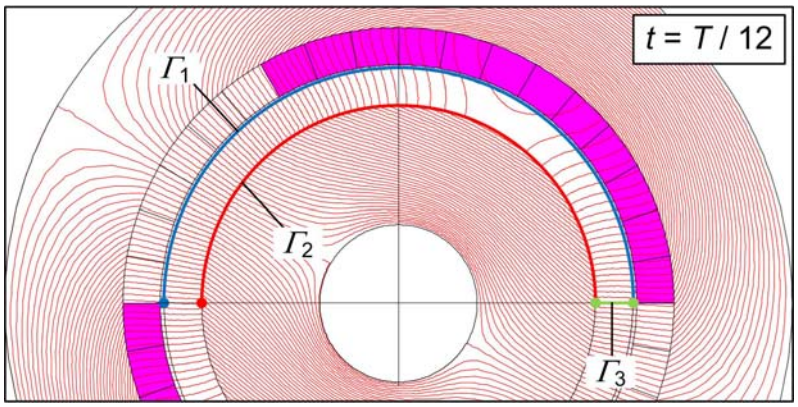

Fig. 6. FE analysis output for the sample SPM slotless machine at instant $t=T/12$, when conductors in magenta carry a current $0.866\times I$ and the other ones carry no current.

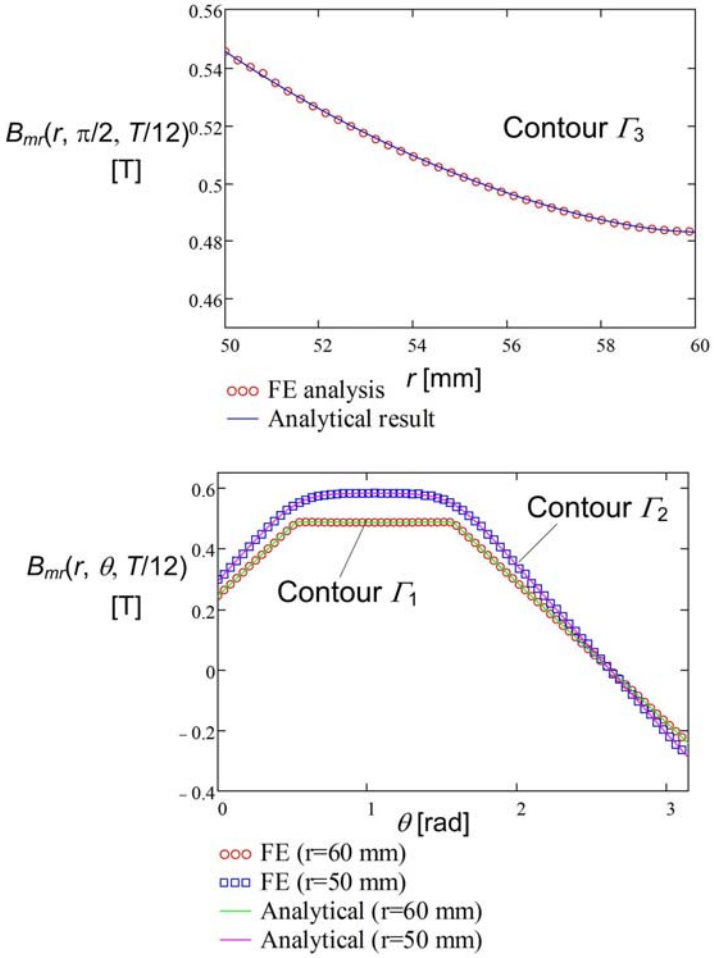

Fig. 7. Radial flux density plotted over contours Γ_1, Γ_2, Γ_3 (Fig. 6) at instant $t=T/12$, according to analytical calculation and FE analysis.

$$j_s = M = \mu_r H_c \frac{h+\delta}{h+\mu_r \delta}$$

$$= \mu_r H_c \frac{R_1 - R_i}{R_m - R_i + \mu_r (R_1 - R_m)} \quad (31)$$

where H_c is permanent magnet coercivity, h is magnet height $h = R_m - R_i$ (Fig. 2), μ_r its relative permability and δ is the air-gap width $\delta = R_1 - R_m$.

The accuracy of replacing permanent magnets with their equivalent current sheets computed as per (31) is assessed

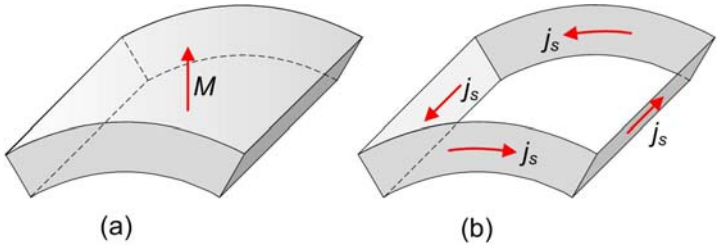

Fig. 8. (a) Surface permanent magnet. (b) Equivalent surface current density.

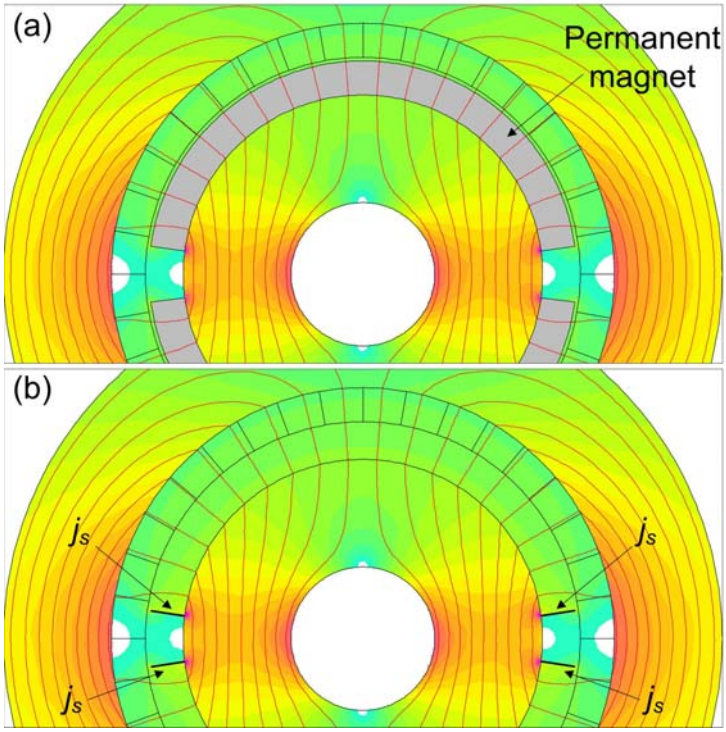

Fig. 9. FE analysis output for the no-load operation (a) with fully-modeled permanent magnets; (b) with equivalent current sheets in place of permanent magnets.

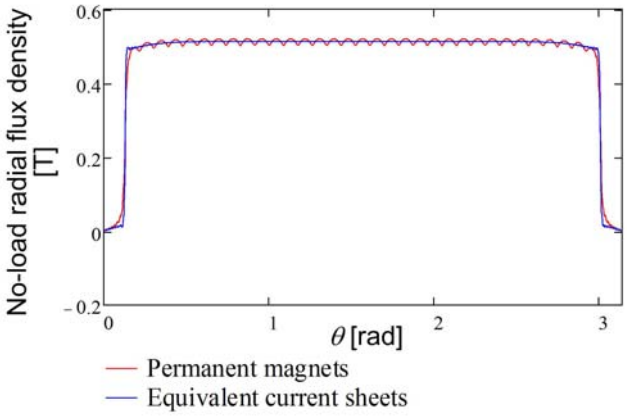

Fig. 10. Comparison between the radial flux density produced on the mean air-gap circumference $r=(R_1+R_m)/2$ by permanent magnets and equivalent current sheets, both computed by FE analysis.

on the sample SPM machine characterized by the data given in Table I. For this machine, the no-load flux distribution is computed by FE analysis using two models as shown in Fig. 9. For one simulation permanent magnets are included in their usual form (Fig. 9a), for the other they are removed and replaced by the surface current j_s, given by (31) and placed on the radial segments shown in Fig. 9b. Flux line distribution and flux density color map (plotted in equal scale) as shown in Fig. 9a and 9b suggest that the magnetic field produced in the machine in the two simulations is practically identical. As a further check, the radial flux density component is plotted over the semi-circumference placed in middle of the mechanical air-gap [$r = (R_m + R_1)/2$]. The radial flux density plots resulting from the two simulations are compared in Fig. 10. It can be seen that the two plots are in good accordance except for the small ripple-like effect observed in the simulation output when permanent magnets are modeled in the conventional way. Such a ripple is due to the fact that, to model a radially-magnetized permanent magnet, the FE simulation software needs to subdivide it into several parallel-magnetized magnet segments.

6.6 Load Torque Computation

As a final step, the machine torque in load condition is computed. For this purpose, a machine model is assumed where the armature reaction field produced by stator currents over time is computed as per Section 6.4 and rotor permanent magnets are replaced by their equivalent surface current density computed as per Section 6.5.

Let us consider a generic instant of time t, when stator currents are given by (2)-(4) and the rotor pole axis, under the hypothesis of synchronous operation, is placed at:

$$\theta_r = \theta_0 + \frac{\omega}{p} t \quad (32)$$

where θ_0 indicates the initial rotor position. It is incidentally noted that, based on the conventions specified in Section 6.2, θ_0 is the complementary of the angle between armature reaction field and permanent magnet field axes; hence, the maximum torque operation for the machine occurs when θ_0=0.

From Fig. 11 it is clear that the equivalent current sheets replacing permanent magnets in the model (segments *PQ* and *RS* for one pole) are located at angles:

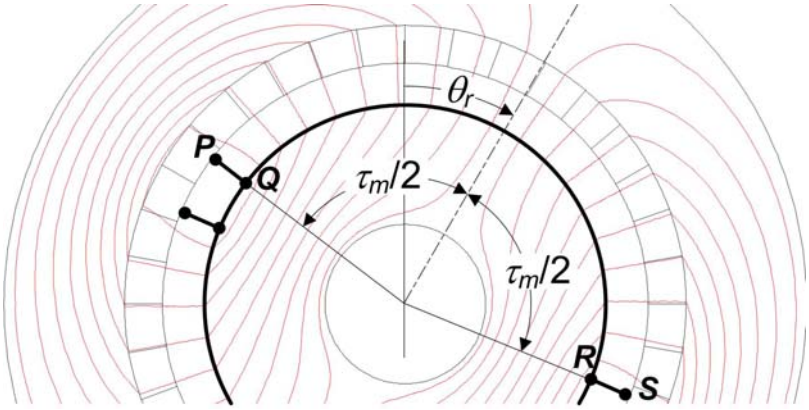

Fig. 11.Example machine with polar axis placed at generic position θ_r. .

$$\theta_r \pm \frac{\tau_m}{2} = \theta_0 + \frac{\omega}{p} t \pm \frac{\pi\, c_m}{2p} \quad (33)$$

where τ_m is permanent magnet angular span and c_m is permanent magnet coverage in per unit (i.e. magnet to pole span ratio).

The torque acting on the rotor is due to the force that originates along the current sheets replacing permanent magnets. For example, considering an infinitesimal element *ds* lying on segment *PQ* and placed at radius *r* (Fig. 11), the Laplace force acting on it will have a tangential component equal to $dF = LB_r j_s dr$, where *L* is machine core length and B_r is the total radial flux density on element *ds*. This will give an electromagnetic torque contribution equal to $dT_{em} = dF\, r$. Hence the total electromagnetic torque on the rotor will be (Fig. 11):

$$T_{em} = 2pL\left(\int_Q^P B_r j_s r dr - \int_R^S B_r j_s r dr\right) \quad (34)$$

The total radial flux density B_r results from two contributions, respectively accounting for rotor permanent magnet and armature reaction field, namely:

$$B_r = B_{mr} + B_{nl} \quad (35)$$

where B_{mr} is the radial flux density due to stator currents, given by (30), and B_{nl} is the no-load radial flux density due to permanent magnets.

Substitution of (35) into (34) gives:

$$T_{em} = 2pL\left(\int_Q^P B_{mr} j_s r dr - \int_R^S B_{mr} j_s r dr\right)$$

$$+ 2pL\left(\int_Q^P B_{nl} j_s r dr - \int_R^S B_{nl} j_s r dr\right) \quad (36)$$

where sign "–" is due to the fact that, on the two current sheets PQ, RS, the surface current j_s has opposite direction.

The sum of integrals in the second bracketed term is certainly zero for slotless SPM machines where, due to the perfect circular symmetry of air-gap boundaries, the two integrals on PQ and RS cancel each other. In fact, the no load flux density B_{nl} has an identical distribution on segments PQ and RS. It is to be observed that, in slotted SPM machines, this is not true, in general, as a consequence of slotting effects. In other words, the second term of (36) gives (in general) the cogging torque, which is known to be zero in slotless SPM machines.

In conclusion, for the machine type under study, (36) can be written as:

$$T_{em} = 2pL\left(\int_Q^P B_{mr} j_s r dr - \int_R^S B_{mr} j_s r dr\right) \quad (37)$$

Considering that B_{mr} is given by (30) and segments PQ, RS are placed at angular positions (33), the torque expression above can be expanded as:

$$T_{em} = 2pL\left[\int_{R_i}^{R_m} B_{mr}\left(r,\theta_r + \frac{\tau_m}{2},t\right) j_s r dr\right.$$

$$\left. - \int_{R_i}^{R_m} B_{mr}\left(r,\theta_r - \frac{\tau_m}{2},t\right) j_s r dr\right] =$$

$$= \sum_{s=-1,1} 2spL\left[\int_{R_i}^{R_m} B_{mr}\left(r,\theta_r + \frac{s\tau_m}{2},t\right) j_s r dr\right] =$$

$$= \sum_{s=-1,1} 2spL\left[\int_{R_i}^{R_m} \frac{\partial A}{\partial \theta}\left(r,\theta_r + \frac{s\tau_m}{2},t\right)\frac{1}{r} r\, j_s dr\right] =$$

$$= -2pL \sum_{\substack{h=5,11,17,\ldots \\ s=1,-1}} shp\, j_s F_h \sin\left(hp\left(\theta_r + \frac{s\tau_m}{2}\right) + \omega t\right)$$

$$-2pL \sum_{\substack{k=1,7,13,\ldots \\ s=1,-1}} sk\, p\, j_s F_k \sin\left(kp\left(\theta_r + \frac{s\tau_m}{2}\right) - \omega t\right) \quad (38)$$

where the constant F_n is defined for any odd integer n as:

$$F_n = \int_{R_i}^{R_m} A^+_{m,n} r^{np} + A^-_{m,n} r^{-np} dr \quad (39)$$

The integral in (39) takes two different solved forms depending on whether np=1 or np≠1, i.e.:

$$F_n =$$

$$\begin{cases} \frac{1}{2} A^+_{m,n}(R_m{}^2 - R_i{}^2) + A^-_{m,n} \ln(R_m / R_i) & \text{if } np = 1 \\ \dfrac{A^+_{m,n}(R_m{}^{np+1} - R_i{}^{np+1})}{np+1} + \dfrac{A^-_{m,n}(R_m{}^{-np+1} - R_i{}^{-np+1})}{-np+1} & \text{if } np \neq 1 \end{cases} \quad (40)$$

It can be noted that the case np=1 occurs only for two-pole machines when n=1.

As a final step, by expressing t as a function of θ_r according to (32), we can write the electromagnet torque (38) as:

$$T_{em} = -2p^2 j_s L \sum_{\substack{h=5,11,... \\ s=1,-1}} shF_h \sin\left(p\theta_r(h+1) + \frac{hps\tau_m}{2} - p\theta_0 \right)$$

$$- 2p^2 j_s L \sum_{\substack{k=1,7,13,... \\ s=1,-1}} skF_k \sin\left(p\theta_r(k-1) + \frac{kps\tau_m}{2} - p\theta_0 \right) \quad (41)$$

Equation (41) gives the exact torque expression as a function of the rotor position θ_r during synchronous operation with an angle displacement $\pi/2-\theta_0$ between the d axis and the armature reaction field [setting $\theta_0=0$ in (41) we have the maximum-torque operating condition].

It might be useful to isolate the mean torque T_{mean} (which is the useful torque) from the torque ripple T_{harm} in (41):

$$T_{em}(\theta_r) = T_{mean} + T_{harm}(\theta_r) \quad (42)$$

The mean torque is given by the θ_r-independent term, which is obtained for $k=1$ in the second sum of (41):

$$T_{mean} = -2p^2 j_s L \sum_{s=1,-1} sF_1 \sin\left(\frac{ps\tau_m}{2} - p\theta_0 \right)$$

$$= -4p^2 j_s L F_1 \sin\left(\frac{p\tau_m}{2} \right) \cos(p\theta_0)$$

$$= -4p^2 j_s L F_1 \sin\left(\frac{\pi}{2} c_m \right) \cos(p\theta_0) \quad (43)$$

which clearly shows how the maximum torque occurs for $c_m=1$ (i.e. when the magnet fully covers the pole span) and for $\theta_0=0$, i.e. in case of stator and rotor fields placed in quadrature position.

As to the ripple torque component, it collects all the θ_r-dependent terms in (41), namely:

$$T_{harm}(\theta_r) =$$

$$= -2p^2 j_s L \sum_{\substack{h=5,11,... \\ s=1,-1}} shF_h \sin\left(p\theta_r(h+1) + \frac{hps\tau_m}{2} - p\theta_0 \right)$$

$$-2p^2 j_s L \sum_{\substack{k=7,13,... \\ s=1,-1}} skF_k \sin\left(p\theta_r(k-1) + \frac{kps\tau_m}{2} - p\theta_0 \right) \quad (44)$$

The torque ripple (44) would be zero in the ideal case of sinusoidal winding distribution. In this case, in fact, coefficients J_n would be zero for $n \neq 1$ in (9) and, consequently, also coefficients $A^+_{m,n}$, $A^-_{m,n}$ would be zero for $n \neq 1$, [see (26)-(29)], as well as coefficients [see (40)]. Conversely, due to the winding being not sinusoidally

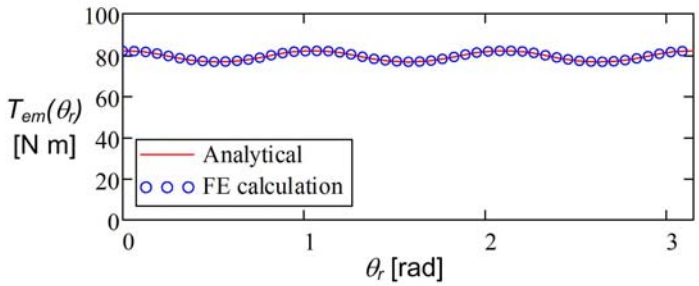

Fig. 12.Electromagnetic torque computed by FE analysis and with the proposed analytical method during synchronous operation .

distributed (see Fig. 3 showing the actual current density distribution), coefficients F_n are not negligible, in practice, which leads to non-negligible torque ripple even in case of sinusoidal current-versus-time waveforms.

As a numerical validation of (42)-(44), a comparison is made between the instantaneous torque values computed through such formulas and by FE analysis on the sample machine with characteristic data given in Table I. The FE simulation is made by successive magnetostatic analyses where the rotor is moved in synchronism with stator currents. The comparison, shown in Fig. 12, highlights that the instantaneous torque can be very accurately predicted through the analytical formulation presented in the chapter. Such model can be therefore used as a fast computationally-efficient alternative to FE analysis if the hypotheses discussed in Section 6.2 are acceptable. The diagram in Fig. 12 also clarifies how the non-sinusoidal stator winding distribution, although in presence of sinusoidal current-versus-time waveform, gives rise to a non-negligible torque ripple amplitude.

As a concluding remark, it is observed that, for the purpose of machine dimensioning, the interesting quantity is only the useful torque developed by the machine, given by (43). This expression is quite compact and easy-to-evaluate compared to those obtained by Maxwell stress tensor method. In fact, using (26)-(29)

and (40), T_{mean} given by (43) can be easily expanded to show the explicit dependence of machine torque on all the construction parameters. This can be very useful in the dimensioning stage as well as in the machine design optimization.

6.7 Conclusion

Slotless SPM machines are used as electric motors and generators in some high-performance applications where torque disturbances and additional losses due to slotting effects need to be minimized. In this chapter, a compact exact analytical expression for the load torque of slotless SPM machines has been derived and validated by FE analysis. The expression proposed has been found by solving Maxwell equations in the air-gap domain to determine armature reaction field and by replacing permanent magnets with equivalent surface current distributions. The torque has been thus computed as the result of the interaction between armature reaction field and rotor equivalent current sheets. Compared to the involved implicit formulations resulting from Maxwell stress tensor methods, the approach proposed in the chapter has led to simple torque expression that can be easily evaluated as a function of machine design quantities. This may be very useful as an alternative method to FE computations in the machine dimensioning and design optimization processes.

6.8 References

[1] Zhu, Z.Q.; Howe, D.; Chan, C.C.; , "Improved analytical model for predicting the magnetic field distribution in brushless permanent-magnet machines," *Magnetics, IEEE Transactions on* , vol.38, no.1, pp.229-238, Jan 2002.D

[2] Atallah, K.; Zi Qiang Zhu; Howe, D.; , "Armature reaction field and winding inductances of slotless permanent-magnet brushless machines," *Magnetics, IEEE Transactions on* , vol.34, no.5, pp.3737-3744, Sep 1998.

[3] Pfister, P.-D.; Perriard, Y.; , "Slotless Permanent-Magnet Machines: General Analytical Magnetic Field Calculation," *Magnetics, IEEE Transactions on* , vol.47, no.6, pp.1739-1752, June 2011.

[4] Tessarolo, A.; Luise, F.; Raffin, P.; Venuti, V.; , "Multi-objective design optimization of a surface permanent-magnet slotless alternator for small power wind generation," *Clean Electrical Power (ICCEP), 2011 International Conference on* , vol., no., pp.371-376, 14-16 June 2011.

[5] Luise, F.; Tessarolo, A.; Pieri, S.; Raffin, P.; Di Chiara, M.; Agnolet, F.; Scalabrin, M.; , "Design and technology solutions for high-efficiency high-speed motors," *Electrical Machines (ICEM), 2012 XXth International Conference on* , vol., no., pp.157-163, 2-5 Sept. 2012.

[6] Komeza, K.; Dems, M.; , "Finite-Element and Analytical Calculations of No-Load Core Losses in Energy-Saving Induction Motors," *Industrial Electronics, IEEE Transactions on* , vol.59, no.7, pp.2934-2946, July 2012.

[7] Tessarolo, A.; Agnolet, F.; Luise, F.; Mezzarobba, M.; , "Use of Time- Harmonic Finite-Element Analysis to Compute Stator Winding Eddy-Current Losses Due to Rotor Motion in Surface Permanent-Magnet Machines," *Energy Conversion, IEEE Transactions on* , vol.27, no.3, pp.670-679, Sept. 2012.

7 Analytical Modeling of Split-Phase Synchronous Reluctance Machines

7.1 Introduction

Synchronous reluctance (SynRel) motors are gaining increasing attractiveness as vehicle traction motor drives thanks to their rugged, cheap and magnet-free rotor construction [1]-[3]. Promising applications of SynRel motors, possibly assisted by permanent magnets, in the automotive field have been recently reported in the literature [4], [5]. An effective way to cope with the strict reliability requirements proper to vehicle traction drives is to equip the electric motor with a split-phase (or multiple three-phase) winding, consisting of two or more three-phase winding sections, each fed by an inverter independently [6]. In this chapter, a SynRel motor with a split-phase stator winding is in fact considered as a possible interesting electric machine topology for fault-tolerant magnet-free vehicle traction applications.

SynRel motors are usually characterized by a round rotor in which magnetic anisotropy (required for reluctance torque production) is achieved by suitably shaped flux barriers [7], [8]. Flux barrier geometry is often defined through an iterative optimization procedure [8] with different possible goals, such as torque ripple enhancement [9], [10] and core loss reduction [11] or in a multi-objective framework [8]. In the optimization procedures, hundreds or thousands of design solutions need to be explored within a reasonable timeframe, which calls for very fast methods for machine analysis, possibly avoiding time-consuming FEA simulations. For this purpose, analytical techniques based on magnetic equivalent circuits (MEC) have been proposed in the literature [10], [11] for the study of SynRel motors (or permanent-magnet assisted ones) featuring three-phase stator winding and flux barriers of roughly uniform width.

In this chapter, MEC technique is extended to study split-phase SynRel motors with an arbitrary set of stator windings and with flux barriers having a circular shape, which are widely used for purely reluctance (magnet-free) motors [3], [7], [12]. The MEC parameters (namely MMF sources and magnetic reluctances) are analytically computed based on motor design data. The MEC analytical solution is used to obtain an accurate estimation of SynRel motor air-gap flux for any rotor position and supply currents. Accuracy of results is successfully assessed by comparison with FEA simulations on a sample six-phase SynRel motor including magnetic saturation effects.

7.2 Modeling Assumptions

In this chapter, a SynRel motor with a split-phase stator winding which includes a generic number N of three-phase sets is taken into account. As shown in Fig. 1, the phases of the N sets are named (A_0, B_0, C_0), (A_1, B_1, C_1), … (A_{N-1}, B_{N-1}, C_{N-1}) and the three-phase sets are displaced $60/N$ electrical degrees apart. Each three phase set is suitable for being supplied by an inverter independently (Fig. 2). In normal operation, all the winding sets are equally loaded, but under faulty or abnormal conditions it may happen that the output currents I_0, I_1… I_{N-1} are different in the N inverters (possibly being equal to zero).

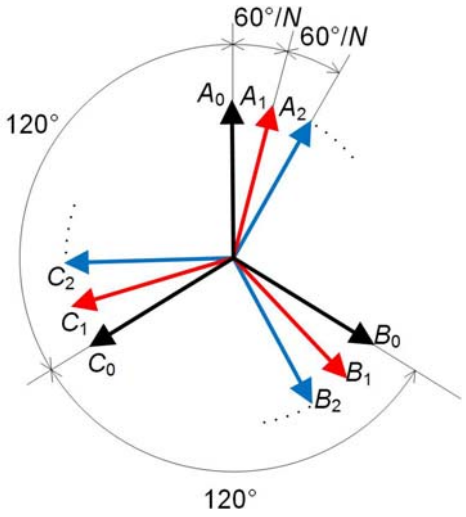

Fig. 1. Phase arrangement and naming for a split-phase winding configuration with *N* three-phase sets.

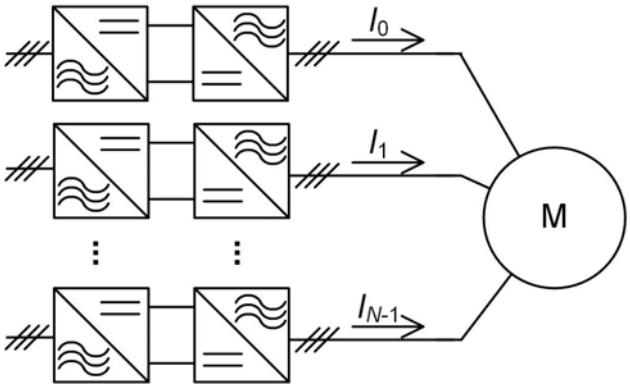

Fig. 2. Overall drive schematic for a split-phase motor with *N* independently fed stator sets.

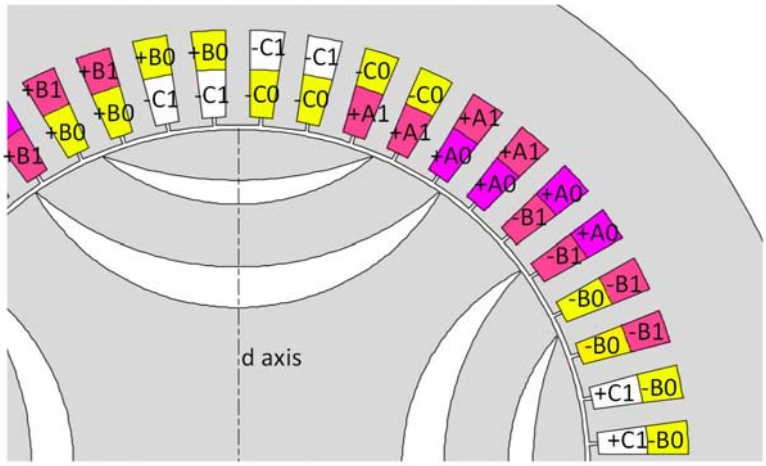

Fig. 3. Example of a four-pole dual-three-phase SynRel motor with two round barriers per pole. Phase arrangement over a pole span.

This brings to the possibility for the drive to operate at reduced power in case of fault on one or more supplying inverters or winding sections. The way in which phases are physically arranged in stator slots is exemplified in Fig. 3, where the case is illustrated of a four-pole dual-three-phase (*N*=2) winding configuration with a dual-layer short-pitch coils with two slots per pole per phase.

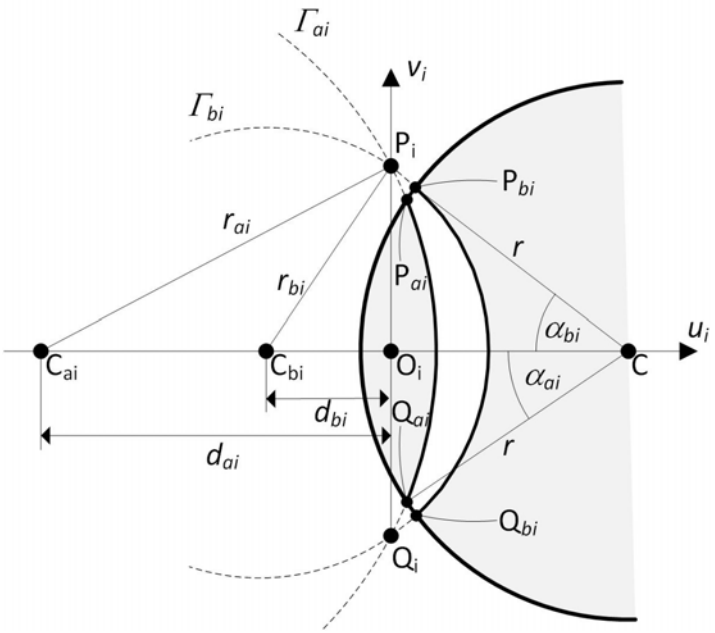

Fig. 4. Characteristic geometric quantities for the i-th flux barrier.

Regarding the rotor, a generic number of flux barriers is assumed (Fig. 3 shows the case of two barriers per pole). For the purpose of MEC definition, the case of uniform-width C-shaped barriers is the most simple and is also addressed in [8], [10], [11] for three-phase machines. The most challenging case of circular flux barriers (Fig. 3, [3], [7], [12]) will be then assumed in the following as it requires a more complex procedure to analytically find the MEC reluctance associated to each barrier. Furthermore, it will be assumed that flux barriers are delimited by circumferential arcs as depicted in Fig. 4. Here, the generic *i*-th flux barrier is represented for example. Its borders lie on circumferences Γ_{ai} (of radius r_{ai} and center C_{ai}) and Γ_{bi} (of radius r_{bi} and center C_{bi}) and intersect the outer rotor circumference (having radius r and center C) at points P_{ai}, Q_{ai} and P_{bi}, Q_{bi}, respectively. These intersection points are identified by the two angles α_{ai} and α_{bi} centered in C, as shown in Fig. 4. The geometry of the *i*-th flux barrier is hence fully determined by the two radii r_{ai}, r_{bi} and by the two angles α_{ai} and α_{bi}. In fact, the centers C_{ai}, C_{bi} are consequently defined by their distance from the rotor center C as follows:

$$\overline{CC_{ai}} = r\cos\alpha_{ai} + \sqrt{r_{ai}^{\,2} - r^2\sin^2\alpha_{ai}} \quad (1)$$

$$\overline{CC_{bi}} = r\cos\alpha_{bi} + \sqrt{r_{bi}^{\,2} - r^2\sin^2\alpha_{bi}} \quad (2)$$

For the following, it is also useful to observe that the two circumferences Γ_{ai} and Γ_{bi} intersect at points P_i, Q_i placed outside the rotor. The intersection of segment P_iQ_i with the barrier symmetry axis is called O_i in Fig. 4 and from elementary geometric calculations one can find the distance of O_i from rotor center C and the length of segment P_iQ_i as follows:

$$\overline{CO_i} = \frac{\overline{CC_{ai}}^2 - \overline{CC_{bi}}^2 - r_{ai}^2 + r_{bi}^2}{2\left(\overline{CC_{ai}} - \overline{CC_{bi}}\right)} \quad (3)$$

$$\overline{P_iQ_i} = \sqrt{\left[\left(\overline{CC_{ai}} - \overline{CC_{bi}}\right) - \frac{\left(r_{ai} - r_{bi}\right)^2}{\overline{CC_{ai}} - \overline{CC_{bi}}}\right]} \times \quad (4)$$

$$\times \sqrt{\left[\frac{\left(r_{ai} + r_{bi}\right)^2}{\overline{CC_{ai}} - \overline{CC_{bi}}} - \left(\overline{CC_{ai}} - \overline{CC_{bi}}\right)\right]}$$

The geometric relationships mentioned above will be used in Section 7.5 for the magnetic field analysis in the flux barriers.

Finally, saturation effects are neglected, or, more precisely, supposed to occur only in the iron bridges between flux barriers and the outer rotor periphery in such a way that no flux passes through these bridges. Such hypothesis is normally assumed in the study of SynRel machines through MEC techniques [10], [11] and is very well matched for sufficiently small bridge widths, as later on confirmed by comparing analytical results with FEA simulations where saturation effects are included (Section 7.7).

7.3 Motor Modeling with MEC Technique

The MEC modeling of the SynRel motor is illustrated in Fig. 5 where, for the sake of clarity and simplicity, the case of a two pole machine with two barriers per pole (indicated as barrier 1 and 2 for one pole, 1' and 2' for the other one) is taken into account. The basic principle for MEC modeling is that the air-gap is subdivided into various regions (sectors), named “11”, “12”, “21”, “22” by the points (Fig. 4) where barriers intersect the rotor outer periphery. For instance, region “11” is delimited by the end points of barrier 1 (or 1'), regions “12” and “21” are delimited by the end points of barriers 1 and 2 (or 1' and 2'), region “22” is delimited by the end points of barriers 2 and 2’. For the generic air-gap region, the relevant air-gap reluctance (R_g) and MMF (F) is naturally defined and computed as discussed in the next Section. Moreover, the reluctances (R_b) associated to rotor flux barriers are defined and, again, reference is made to the next Section for their analytical computation. The nodes of the MEC are identified as S, A, B, A', B', R. Each node represents a portion of the machine (core) where no MMF drop is supposed to occur under the hypothesis (Section 7.2) of disregarding magnetic saturation. The fluxes passing through the various air-gap regions are finally indicated in Fig. 5 (Φ_{11}, Φ_{12}, Φ_{21}, Φ_{22}) as well as the flux (Φ_2) passing through barrier 2.

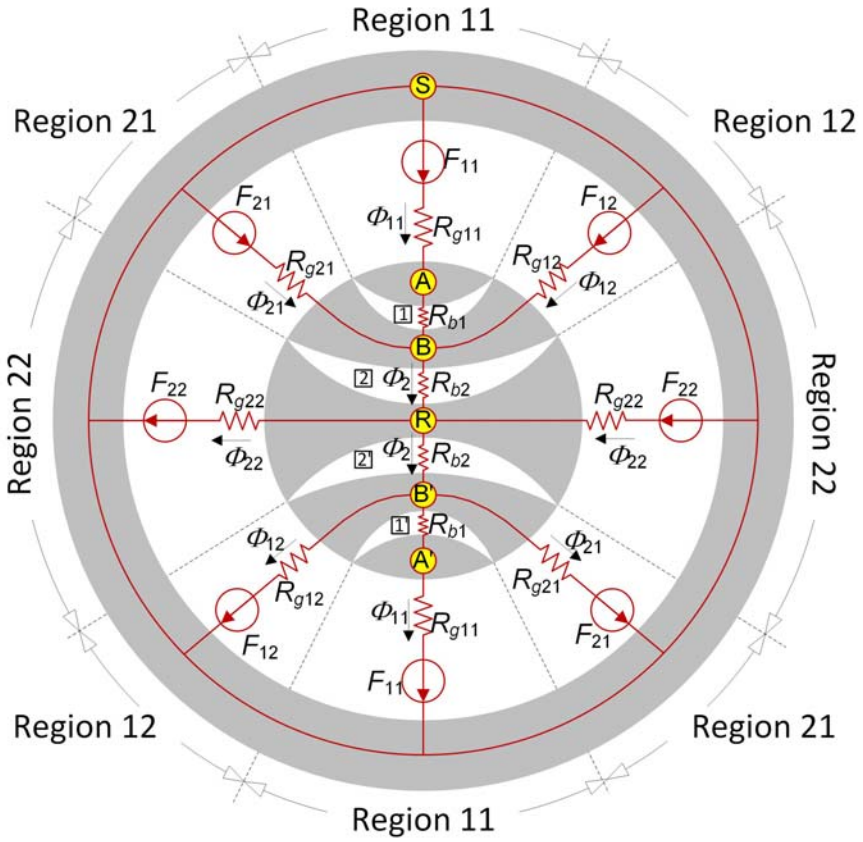

Fig. 5. Schematic of the SynRel MEC for a two-pole motor with two barriers per pole.

The MEC sketched in Fig. 5 can be solved using well known methods of circuit theory analysis [13]. These give the following solution for the fluxes Φ_{11} and Φ_2 passing through barriers 1 and 2:

$$\Phi_2 = F_{eq} / \left(R_{eq} + R_{b2} \right) \quad (5)$$

$$\Phi_{11} = \frac{F_{11} - \left(F_{eq} - R_{eq} \Phi_2 \right)}{R_{g11} + R_{b1}} \quad (6)$$

Where:

$$F_{eq} = \left(\frac{F_{11}}{R_{g11} + R_{b1}} + \frac{F_{12}}{R_{g12}} + \frac{F_{21}}{R_{g21}} \right) R_{eq} \quad (7)$$

$$R_{eq} = \left[\left(R_{g11} + R_{b1} \right)^{-1} + R_{g12}^{-1} + R_{g21}^{-1} \right]^{-1} \quad (8)$$

The two fluxes (5)-(6) will be used in Section 7.6 to compute machine air-gap flux density distribution.

7.4 Computation of Air-gap MMF Sources

In this Section, the MMF sources of the MEC (e.g. F_{11}, F_{12}, F_{21}, F_{22} in Fig. 5) are analytically computed. The computation is based on the analytical expression of the air-gap MMF field produced by a split-phase winding with N three-phase winding sets ([6], Fig. 1). It is assumed that the currents in the w-th three-phase winding (w=0, 1, …, N) is:

$$i_{p,w}(t) = \sum_{h=1}^{\infty} I_{w,h} \cos\left[h\left(\omega t - \frac{2\pi p}{3} - \frac{\pi w}{3N} \right) \right] \quad (9)$$

where p is the phase index ranging from 0 to 2 (0 corresponds to phase "A", 1 to phase "B", 2 to phase "C"), h is the time harmonic order, $I_{w,h}$ is the amplitude of the current in the p-th phase of the w-th winding set in regard to the h-th order time harmonic. Calling x the angular position along the air-gap circumference in electrical radians, measured from the symmetry axis of phase "A0" taken as the zero reference, the air-gap MMF distribution as a function of time (t) and space (x) is [6]:

$$F(t,x) = F^{+}(t,x) + F^{-}(t,x) \quad (10)$$

where $F^{+}(t,x)$ and $F^{-}(t,x)$ are the travelling waves which respectively rotate in the same and opposite sense with respect to the fundamental. They can be written as [6]:

$$F^{+}(t,x) = \mathrm{Re}\left\{ \sum_{h,k=1}^{\infty} M_{h,k}^{+} e^{i(h\omega t - kx)} \right\}, F^{-}(t,x) = \mathrm{Re}\left\{ \sum_{h,k=1}^{\infty} M_{h,k}^{-} e^{i(h\omega t + kx)} \right\} \quad (1)$$

where i denotes the imaginary unit, k is the space harmonic order and coefficients $M_{h,k}^{+}$, $M_{h,k}^{-}$ are:

$$M_{h,k}^{+} = \begin{cases} \frac{6}{\pi} \frac{qnC_k}{k} \sum_{w=0}^{N-1} I_{w,h} e^{-i\left[\frac{(h-k)\pi w}{3N}\right]} & \text{if } \mathrm{mod}(|h-k|,3) = 0 \\ 0 & \text{otherwise} \end{cases} \quad (2)$$

$$M_{h,k}^{-} = \begin{cases} \frac{6}{\pi} \frac{qnC_k}{k} \sum_{w=0}^{N-1} I_{w,h} e^{-i\left[\frac{(h+k)\pi w}{3N}\right]} & \text{if } \mathrm{mod}(|h+k|,3) = 0 \\ 0 & \text{otherwise} \end{cases} \quad (3)$$

In (12)-(13), q is the number of slots per pole per phase, n the number of series-connected turns per coil and coefficients C_k are defined as:

$$C_k = \sin(\pi k r/2)\frac{\sin(\alpha_s q\, k/2)}{q\sin(\alpha_s k/2)} \qquad (4)$$

being $\alpha_s = \pi/(3Nq)$ the slot pitch in electrical radians:

From the air-gap MMF distribution function, calling x_r the position (in electrical radians) of the rotor *d*-axis (taken coincident with flux barrier symmetry axis, Fig. 3) with respect to phase "A0" symmetry axis, we can compute the total MMF that pertain to the various air-gap regions identified in the machine (Fig. 5). For instance, in case of two barriers per pole (Fig. 5), we have:

$$F_{11}(t, x_r) = \frac{1}{2x_r}\int_{x_r - x_1}^{x_r + x_1} F(t,x)dx \qquad (5)$$

$$F_{12}(t, x_r) = \frac{1}{x_2 - x_1}\int_{x_r + x_1}^{x_r + x_2} F(t,x)dx \qquad (6)$$

$$F_{21}(t, x_r) = \frac{1}{x_2 - x_1}\int_{x_r - x_2}^{x_r - x_1} F(t,x)dx \qquad (7)$$

where $2x_i$ denotes the length of the rotor outer circumference arc between points P_i and Q_i for the *i*-th rotor barrier (Fig. 4), namely according to Fig. 4:

$$x_1 = r\alpha_1(P/2), x_2 = r\alpha_2(P/2) \qquad (8)$$

for the two flux barriers (i=1, i=2). The coefficient $P/2$ is needed to pass from mechanical radians (α_i) to electrical radians (x_i).

From a physical viewpoint, (15)-(17) represent the average MMF in the three air-gap regions "11", "12", "21". The value of F_{22} is defined in the same way, but it is not worth being computed as it does not appear in the MEC solution for the interesting unknowns Φ_{11} and Φ_2 as per (5)-(8).

7.5 Computation of Air-gap and Barrier Reluctances

The SynRel MEC shown in Fig. 5 also includes the reluctances (R_g) associated to the various air-gap regions and the ones (R_b) associated to the flux barriers.

7.5.1 Air-gap reluctances

Taking the example case of a SynRel with two barriers per pole (Fig. 3, Fig. 5), air-gap reluctances can be trivially computed as follows:

$$R_{g11} = \frac{1}{\mu_0}\frac{g}{2x_1 rL}\frac{P}{2} \tag{9}$$

$$R_{g12} = R_{g21} = \frac{1}{\mu_0}\frac{g}{(x_2 - x_1) rL}\frac{P}{2} \tag{10}$$

$$R_{g22} = \frac{1}{\mu_0}\frac{g}{(\pi - x_2) rL}\frac{P}{2} \tag{11}$$

where L is machine core length, r the rotor radius, g is the air-gap width, μ_0 is the magnetic permeability of the air and P is the number of machine poles.

7.5.2 Flux barrier reluctance

While for C-shaped flux barriers, with approximately uniform width, the reluctance is easy to compute [10], [11], some complications arise with respect to round or circular-shaped flux barriers (Fig. 3, [3], [7], [12]). The detailed mathematical procedure for reluctance computation in this case will be covered in a dedicated publication and is omitted here for the sake of brevity. What is only recalled, for the purpose of the chapter, is the final expression of the magnetic vector potential in a generic flux barrier and such expression is then used to derive the flux barrier reluctance.

7.5.2.1 Magnetic vector potential and flux density in the i-th barrier

Let us consider the generic *i*-th flux barrier domain (Fig. 4). To compactly write the vector potential expression inside it, it is convenient to fix a Cartesian reference frame having its origin in point O_i and axes u_i, v_i (Fig. 4). In this coordinate system, it is possible to prove that the magnetic vector potential inside the flux barrier can be written in the form:

$$A(u_i, v_i) = \frac{B_0}{4}\ln\frac{(\tau_i/2 + v_i)^2 + u_i^2}{(\tau_i/2 - v_i)^2 + u_i^2} + A_0 \tag{12}$$

where $\tau_i = \overline{P_i Q_i}$ is given by (4), A_0 is an arbitrary additive constant and B_0 is a parameter which depends on the operating point (i.e., in other words, on stator currents and rotor position).

The fact that (22) is the vector potential inside the *i*-th flux barrier can be proved by checking that it satisfies Laplace differential equation in the inner points of the flux barrier and the Neumann boundary conditions on the borders [14]. More precisely, Laplace equativo

$$\frac{\partial^2 A(u_i,v_i)}{\partial^2 u_i}+\frac{\partial^2 A(u_i,v_i)}{\partial^2 v_i}=0 \qquad (13)$$

can be proved to hold by directly substituting the partial derivatives of (22) into (23). The flux density can be consequently derived as [14]:

$$\mathbf{B}(u_i,v_i)=\begin{pmatrix} B_{ui}(u_i,v_i)\\ B_{vi}(u_i,v_i)\end{pmatrix}=\begin{pmatrix} -\partial A(u_i,v_i)/\partial v_i\\ \partial A(u_i,v_i)/\partial u_i\end{pmatrix}= \qquad (14)$$

$$=\frac{B_0\tau_i/2}{\left((\tau_i/2+v_i)^2+u_i^2\right)\left((\tau_i/2-v_i)^2+u_i^2\right)}\begin{pmatrix} v_i^2-u_i^2-(\tau_i/2)^2\\ 2u_iv_i\end{pmatrix}$$

As regards boundary conditions, we can observe that the barrier borders are arcs of circumferences Γ_{ai} and Γ_{bi} whose Cartesian equations in the $u_iO_iv_i$ reference frame are:

$$\Gamma_{ai}:\ (u_i+d_{ai})^2+v_i^{\,2}=r_{ai}^{\,2} \qquad (15)$$

$$\Gamma_{bi}:\ (u_i+d_{bi})^2+v_i^{\,2}=r_{bi}^{\,2} \qquad (16)$$

where $d_{ai}=\sqrt{r_{ai}^{\,2}-(\tau_i/2)^2}$, $d_{bi}=\sqrt{r_{bi}^{\,2}-(\tau_i/2)^2}$ (see Fig. 4 for the geometric meaning of d_{ai}, d_{bi}).

Hence, the tangent vectors ($\mathbf{t}_{ai}$ and $\mathbf{t}_{bi}$) to the two circumferences Γ_{ai} and Γ_{ai} in a point of abscissa u_i are easily found to be:

$$\mathbf{t}_{ai}(u_i)=\begin{pmatrix}\pm 1 & -\dfrac{d_{ai}+u_i}{\sqrt{r_{ai}^{\,2}-(d_{ai}+u_i)^2}}\end{pmatrix}^t \qquad (17)$$

$$\mathbf{t}_{bi}(u_i)=\begin{pmatrix}\pm 1 & -\dfrac{d_{bi}+u_i}{\sqrt{r_{bi}^{\,2}-(d_{bi}+u_i)^2}}\end{pmatrix}^t \qquad (18)$$

Newmann boundary conditions can be written in the form:

$$\mathbf{t}_{ai}(u_i)\bullet\mathbf{B}(u_i,v_i)=0 \ \text{ on } \Gamma_{ai} \qquad (19)$$

$$\mathbf{t}_{bi}(u_i) \bullet \mathbf{B}(u_i, v_i) = 0 \text{ on } \Gamma_{bi} \qquad (20)$$

meaning that the flux density is anywhere orthogonal to the flux barrier border. Actually, (29) can be easily checked to hold for all (u_i, v_i) pairs satisfying (25) and (30) to hold for all (u_i, v_i) pairs satisfying (26).

7.5.2.2 Reluctance calculation for the i-th flux barrier

Once the field inside the *i*-th flux barrier is known, its reluctance R_{bi} can be computed from Hopkinson law as:

$$R_{bi} = \Delta H_{barr} / \Phi_{barr} \qquad (21)$$

where Φ_{barr} is the flux crossing the barrier and ΔH_{barr} is the MMF drop across it. Φ_{barr} can be computed directly using the vector potential (22) as [14]:

$$\Phi_{barr} = L\left[A(u_{Pai}, v_{Pai}) - A(u_{Qai}, v_{Qai})\right] \qquad (22)$$

where (u_{Pai}, v_{Pai}) and (u_{Qai}, v_{Qai}) are the coordinates of flux barrier end points P_{ai}, Q_{ai} (Fig. 4). From the inspection of Fig. 4 we have:

$$v_{Pai} = -v_{Qai} = r \sin \alpha_{a1} \qquad (23)$$

and by substitution of (33) into (25) we have:

$$u_{Pai} = u_{Qai} = \sqrt{r_{a1}{}^2 - r^2 \sin^2 \alpha_{a1}} - d_{a1} \qquad (24)$$

By using (22) we can derive an explicit analytical expression for Φ_{barr}:

$$\Phi_{barr} = L \frac{B_0}{2} \ln \frac{(\tau_i / 2 + r \sin \alpha_{a1})^2 + \left(\sqrt{r_{a1}{}^2 - r^2 \sin^2 \alpha_{a1}} - d_{a1}\right)^2}{(\tau_i / 2 - r \sin \alpha_{a1})^2 + \left(\sqrt{r_{a1}{}^2 - r^2 \sin^2 \alpha_{a1}} - d_{a1}\right)^2} \qquad (25)$$

The MMF drop ΔH_{barr} across the flux barrier can be computed by integration of the magnetic field (24) along a path that goes from one to the other border of the flux barrier. For instance, taking a linear path along the barrier axis of symmetry, we have:

$$\Delta H_{barr} = \frac{1}{\mu_0} \int_{r_{a1}-d_{a1}}^{r_{b1}-d_{b1}} B(u,0)du \qquad (26)$$

Using (24) and performing the integral symbolically, this yields:

$$\Delta H_{barr} = \frac{B_0}{\mu_0} \left[\arctan\left(\frac{2(r_{b1}-d_{b1})}{\tau_i} \right) - \arctan\left(\frac{2(r_{a1}-d_{a1})}{\tau_i} \right) \right] \qquad (27)$$

By substitution of (35) and (37) into (31) we obtain:

$$R_{bi} = \frac{2\left[\arctan\left(\frac{2(r_{b1}-d_{b1})}{\tau_i} \right) - \arctan\left(\frac{2(r_{a1}-d_{a1})}{\tau_i} \right) \right]}{L\mu_0 \ln \frac{(\tau_i/2 + r\sin\alpha_{a1})^2 + \left(\sqrt{r_{a1}{}^2 - r^2 \sin^2 \alpha_{a1}} - d_{a1} \right)^2}{(\tau_i/2 - r\sin\alpha_{a1})^2 + \left(\sqrt{r_{a1}{}^2 - r^2 \sin^2 \alpha_{a1}} - d_{a1} \right)^2}} \qquad (38)$$

We can observe that the analytical expression (38) for the reluctance of the *i*-th flux barrier does not depend on the operating point [parameter B_0 in (22) cancel out] and only depends on the barrier geometry and machine core length L.

7.6 Computation of Air-gap Flux

Once the MEC of the SynRel motor has been evaluated and solved (Section 7.3-7.5), the solution can be used to compute the air-gap flux density distribution in the machine. For this purpose, it is necessary to correct the MMF due to stator currents (Section 7.4) by adding or subtracting the MMF drops due to the flux flowing across rotor barriers. In particular, in the case of two barriers per pole, the following two MMF drops are to be computed:

$$\Delta F_{11} = \Phi_{11} R_{b1} + \Phi_2 R_{b2} \qquad (28)$$

$$\Delta F_{12} = \Phi_2 R_{b2} \qquad (29)$$

The former contribution is to be applied to region "11" and accounts for the MMF drop due to the flux passing through both barriers 1 and 2. The contribution (40) instead, applies to the regions "12" and "21" and accounts for the MMF due to the flux passing across barrier 2 only. Finally, no correction to stator current MMF is to be applied in region "22" because all the flux flowing in such region does not cross any rotor barrier. The total MMF (including stator current contribution and MMF drops through rotor barriers) can be written in the form given in (42) at the bottom of the page. Since (42) represents a total (resultant) MMF acting in the air-gap, the flux density immediately derives from it as:

$$B_{tot}(t,x,x_r) = (\mu_0 / g) F_{tot}(t,x,x_r) \qquad (30)$$

$$F_{tot}(t,x,x_r) = \begin{cases} F(t,x) - \Delta F_{11}(t,x_r) & if \quad \left(0 \le \left|\mathrm{mod}(x-x_r, 2\cdot\pi)\right| \le x_1\right) \vee \left(2\cdot\pi - x_1 \le \left|\mathrm{mod}(x-x_r, 2\cdot\pi)\right| \right. \\ F(t,x) + \Delta F_{11}(t,x_r) & if \quad \left(\pi - x_1 \le \left|\mathrm{mod}(x-x_r, 2\cdot\pi)\right| \le \pi + x_1\right) \\ F(t,x) - \Delta F_{12}(t,x_r) & if \quad \left(x_1 \le \left|\mathrm{mod}(x-x_r, 2\cdot\pi)\right| \le x_2\right) \vee \left(2\cdot\pi - x_2 \le \left|\mathrm{mod}(x-x_r, 2\cdot\pi)\right| \right. \\ F(t,x) + \Delta F_{12}(t,x_r) & if \quad \left(x_1 + \pi \le \left|\mathrm{mod}(x-x_r, 2\cdot\pi)\right| \le x_2 + \pi\right) \vee \left(\pi - x_2 \le \left|\mathrm{mod}(x-x_r, 2\cdot\pi)\right| \right. \\ F(t,x) & otherwise \end{cases} \qquad (42)$$

7.7 Assessment Against FEA Simulation

The methodology proposed in the chapter is next applied to the four-pole dual-three-phase SynRel motor whose cross section is shown in Fig. 3. Its characteristic data are provided in Table I.

Tab1e I. Characteristic data of the example SynRel machines

Rotor outer radius, *r*	212 mm
Air gap width	3 mm
Number of stator slots	48
Number of poles	4
Number of turns per coil	5
Coil to pole pitch ratio	10/12
Number of slots per pole per phase	2
Angles α_{a1}, α_{b1} of barrier 1 (	α_{a1}=22,50°, α_{b1}=22,83°
Angles α_{a2}, α_{b2} of barrier 2 (	α_{a2}=35,36°, α_{b2}=35,68°
Radii r_{a1}, r_{b1} of barrier 1 (	r_{a1}=184,2 mm, r_{b1}=141,9 mm
Radii r_{a2}, r_{b2} of barrier 2 (	r_{a2}=227,3 mm, r_{b2}=128,1 mm
Iron bridge width	1 mm

Stator and rotor cores are characterized by a ferromagnetic material having an ordinary BH curve with a saturation knee located at around H=15.000 A/m and B=1.65 T.

As a first study case, both machine windings are energized with a peak current of 50 A taking its maximum value in phase A0. The currents in the other phases are set according to (9) taking the instant t=0 and setting all current harmonics different from the fundamental to zero ($I_{w,h}$=0 for h≠0). For such a current distribution, the rotor is placed at different positions x_r with respect to phase A0 axis and, for each position, a FEA simulation is run (Fig. 6a). The resulting air-gap field is then plotted and compared to that obtained analytically from (41) where t=0. The comparisons for x_r=0°, x_r=15°, x_r=30° and x_r=60° electrical degrees are shown in Fig. 7, showing an excellent agreement with analytical predictions.

As a second study case, one of the two winding sets is again energized with a 50 A current (the maximum current value being in phase A0), while the other set is at no load [$I_{w,h}$=50 for h=1 and w=0, while $I_{w,h}$=0 for any other w and h in (9)]. FEA simulations are also run in this case for different rotor positions (Fig. 6b). The air-gap flux density obtained from FEA is then compared to the analytical prediction, as depicted in Fig. 8, showing a very good agreement.

7.8 Conclusion

SynRel motors with split-phase stator winding sets supplied by multiple inverters have been investigated in this chapter as an increasingly attractive solution for fault-tolerant, rugged, magnet-free vehicle traction drives. These machines are typically designed through iterative optimization techniques in which thousands of alternatives are evaluated in search for an optimum.

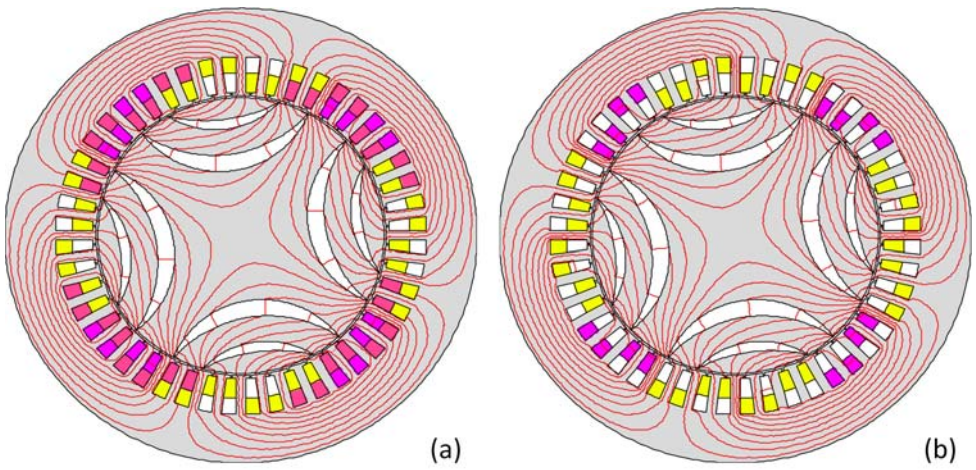

Fig. 6. FEA simulation output for rotor position x_r=15° and for (a) both winding sets energized; (b) only one winding set energized.

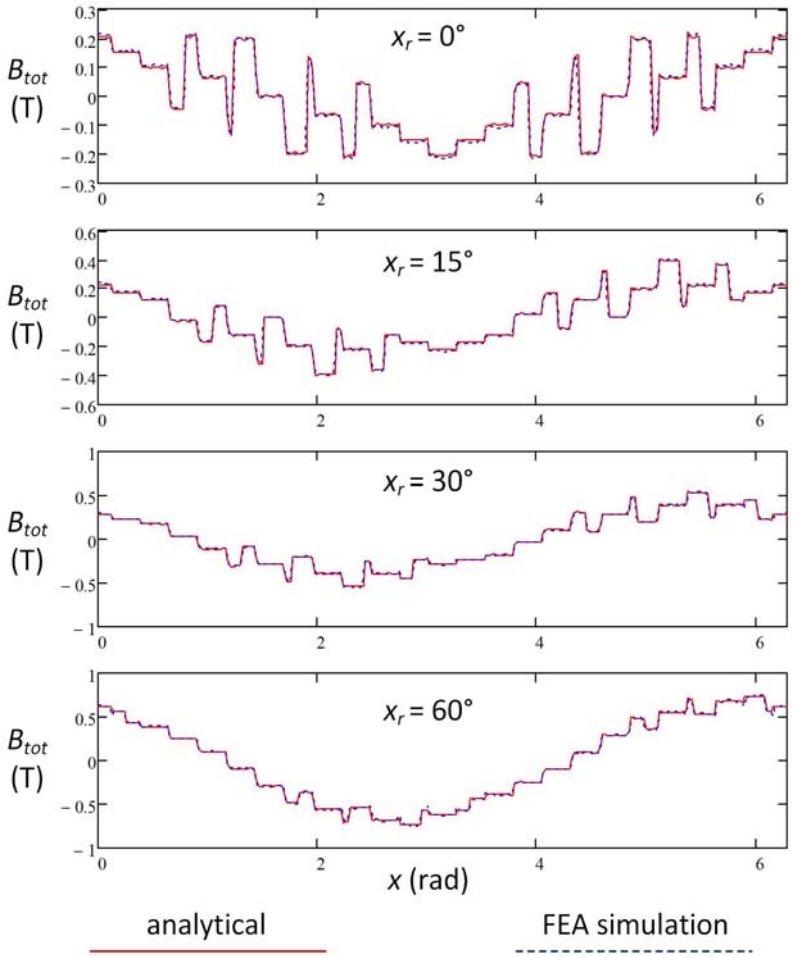

Fig. 7. Air-gap flux density over a pole span, computed analytically and by FEA simulation for both windings energized with 50 A current.

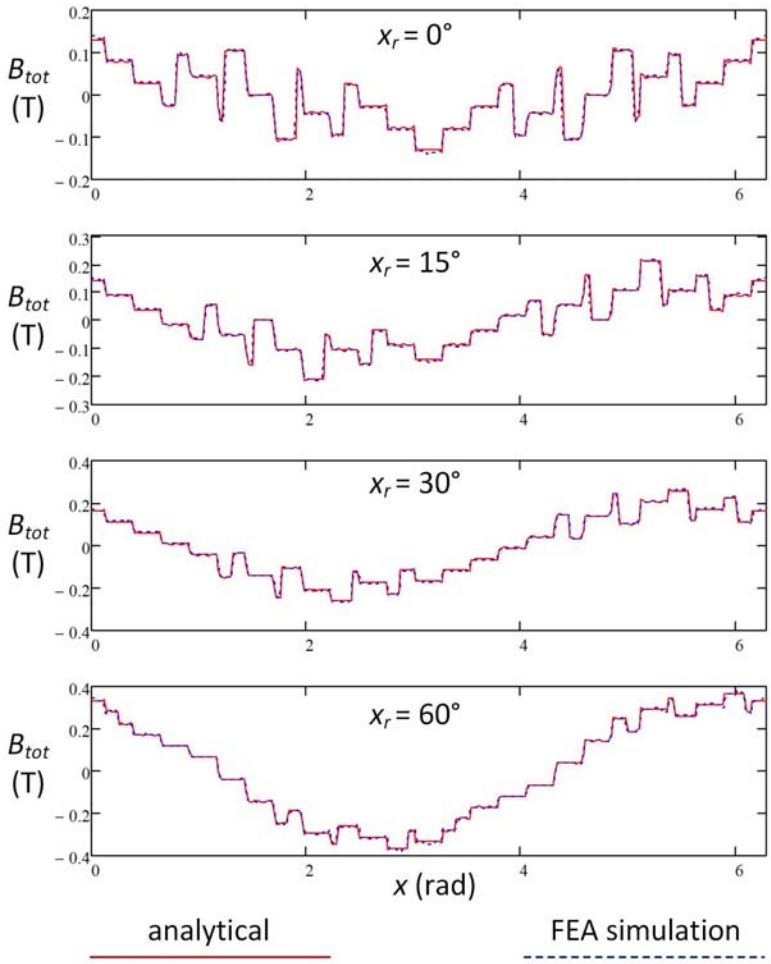

Fig. 8. Air-gap flux density over a pole span, computed analytically and by FEA simulation for unbalanced SynRel motor operation (one winding energized with 50 A current, the other at no load).

This calls for very fast computation approaches to keep optimization procedures within acceptable timeframes. In response to such a need, the chapter has proposed an analytical method for the air-gap computation of split-phase SynRel motors equipped with an arbitrary number of stator three-phase sets and with circular-shaped rotor barriers. The MEC model of the motor has been first defined and analytical procedures have been presented to compute its parameters. The flux density distribution in the air-gap has been then derived based on MEC solution. The accuracy of the proposed methodology has been assessed against FEA simulations (including magnetic saturation) showing a very good agreement between numerical and analytical predictions. This suggests that the proposed approach can be a fast, accurate and reliable alternative to time-consuming FEA simulations for the analysis of the electric machine topology under study. Future investigations, presently in progress or in publication, will address the extensions of the presented model for electromagnetic torque computation and for machine transient analysis and operation with arbitrary (non-sinusoidal) current waveforms.

7.9 References

[1] J.K. Kostko, "Polyphase reaction synchronous motors", *Journal of the American Institute of Electrical Engineers,* vol. 42, no. 11, pp. 1162-1168, Nov. 1923.

[2] T.A. Lipo, "Synchronous reluctance machines. A viable alternative for ac drives?", *Electric Machines and Power Systems*, vol. 19, no. 6, pp. 659–671, 1991.

[3] P. Niazi, H.A. Toliyat, Dal-Ho Cheong, Jung-Chul Kim, "A Low-Cost and Efficient Permanent-Magnet-Assisted Synchronous Reluctance Motor Drive", *IEEE Transactions on Industry Applications,* vol. 43, no. 2, pp. 542-550, March-April 2007.

[4] S. Taghavi, P. Pillay, "A Sizing Methodology of the Synchronous Reluctance Motor for Traction Applications", *IEEE Journal of Emerging and Selected Topics in Power Electronics,* vol. 2, no. 2, pp.329,340, June 2014.

[5] A.A. Arkadan, N. Al-Aawar, and A.A. Hanbali, "Design optimization of SynRM drives for HEV power train applications", *IEEE International Electric Machines and Drives Conference* (*IEMDC '07*), pp. 810–814, May 2007.

[6] A. Tessarolo, "Analysis of split-phase electric machines with unequally-loaded stator windings and distorted phase currents", *2010 XIX International Conference on Electrical Machines (ICEM),* 6-8 Sept. 2010.

[7] G. Pellegrino, F. Cupertino, C. Gerada, "Barriers shapes and minimum set of rotor parameters in the automated design of Synchronous Reluctance machines", *2013 IEEE International Electric Machines & Drives Conference (IEMDC),* pp. 1204-1210, 12-15 May 2013.

[8] R.-R. Moghaddam, F. Gyllensten, "Novel High-Performance SynRM Design Method: An Easy Approach for A Complicated Rotor Topology", *IEEE Transactions on Industrial Electronics,* vol. 61, no. 9, pp. 5058-5065, Sept. 2014.

[9] Jung-Min Park, Sung-Il Kim, Jung-Pyo Hong, Jung-Ho Lee, "Rotor Design on Torque Ripple Reduction for a Synchronous Reluctance Motor With Concentrated Winding Using Response Surface Methodology", *IEEE Transactions on Magnetics,* vol. 42, no. 10, pp. 3479-3481, Oct. 2006.

[10] N. Bianchi, S. Bolognani, D. Bon, M.D. Pré, "Rotor Flux-Barrier Design for Torque Ripple Reduction in Synchronous Reluctance and PM-Assisted Synchronous Reluctance Motors", *IEEE Transactions on Industry Applications,* vol. 45, no. 3, pp. 921-928, May-June 2009.

[11] M. Barcaro, N. Bianchi, "Air-Gap Flux Density Distortion and Iron Losses in Anisotropic Synchronous Motors", *IEEE Transactions on Magnetics,* vol. 46, no. 1, pp. 121-126, Jan. 2010.

[12] H. Kiriyama, S. Kawano, Y. Honda, T. Higaki, S. Morimoto, Y. Takeda, "High performance synchronous reluctance motor with multi-flux barrier for the appliance industry", *Thirty-Third IAS Annual Meeting. The 1998 IEEE Industry Applications Conference, 1998.*, pp.111-117, 12-15 Oct. 1998.

[13] J.W. Nilsson, S.A. Riedel, *Electric Circuits*, 9th edition, Prentice Hall, 2011.

[14] J. D. Jackson, *Classical Electrodynamics*, John Wiley and Sons, New York, 1999.

8 An Accurate Fourier-Series Expansion for Round-Rotor Electric Machine Permeance Function Including Large Eccentricity Effects

8.1 Introduction

One of the key tasks in multiphase AC electric machine modeling is the analytical expression of phase self and mutual inductances as a function of the rotor position [1], [2]. This can be a non trivial issue specially for salient-pole machines [2] as well as for machines subject to rotor eccentricities [3]-[4]. A powerful tool for self and mutual inductance analytical computation is constituted by winding and permeance functions [1]-[4]. Various permeance function approximations have been proposed in the literature to describe eccentricity effects in both round-rotor and salient-pole electric machines [3]-[6]. In most works, eccentricity is supposed to be very small compared to air-gap width, which justifies introducing quite crude approximations, like Taylor series expansions truncated to the first few terms. In this chapter, the general case is instead investigated of a round-rotor machine subject to important eccentricity effects, which requires a certain accuracy to be preserved in the permenace function expression. A further constraint considered in the chapter is that the permeance function expression being sought must be in the form of a Fourier series expansion, which is important for it to be effectively used in multiphase machine analytical models [1], [2]. The problem is solved in the chapter moving from an initial geometric analysis to determine the permeance function expression in a closed form; as s further step, this is turned into a Fourier series form. Throughout this second step, some integrals are encountered that do not allow for a closed-form symbolical solution, so asymptotic-series approximations have to be adopted. Finally, a permenance function expression as a Fourier series expansion is found. Despite of its quite complicated appearance, the proposed formulation is proved to be accurate and computationally efficient as it involves series approximations that very rapidly converge to their asymptotical values. This results in a small number of series terms required for achieving a satisfactory precision.

8.2 Geometric Model

A general geometric model for a round-rotor electric machine with eccentricity is shown in Fig. 9. The rotor eccentricity (which can be either static or dynamic) is identified by the amplitude ε and the angle α, the latter measured with respect to a fixed reference line s attached to the stator (having radius R_s, while rotor radius is R_r). With respect to the same line s, a generic point P along the stator bore circumference is identified by an angle θ. Obviously, the air-gap width at point P is not univocally determined. The concept can be clarified looking at the zoomed view shown in Fig. 2, where the air-gap region around point P is suitably enlarged. Lines AP and BP are the lines passing through P and respectively orthogonal to the stator and rotor surfaces. Distances AP and BP are respectively indicated as g_s and g_r. In absence of eccentricity, we would have that $g_s=g_r=g=R_s-R_r$ being g the univocally-defined air-gap width.

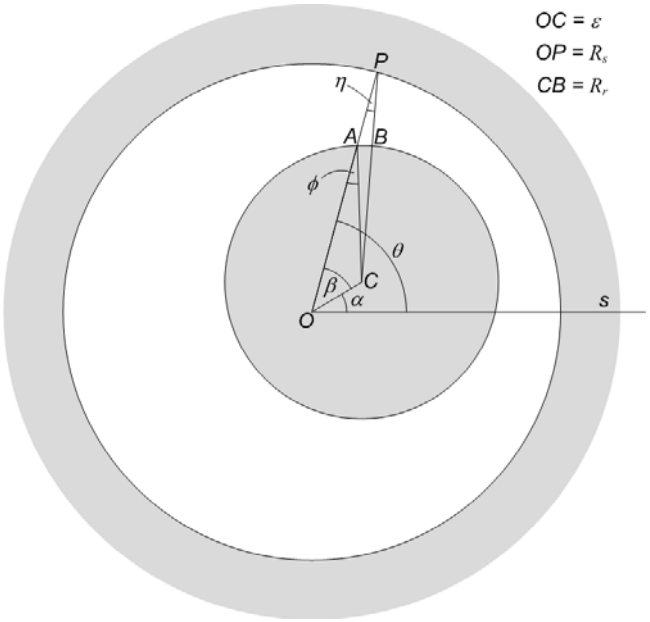

Fig. 9. General geometricl model for a round rotor machine with eccentricity.

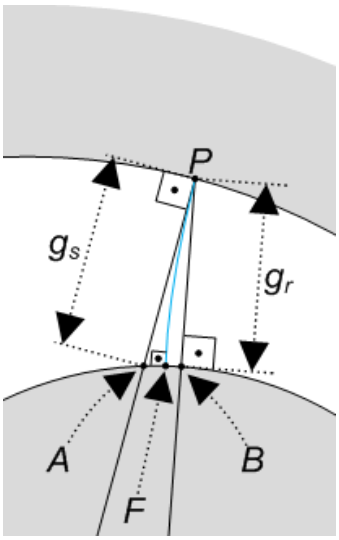

Fig. 10. Zoomed view of the air-gap in the neighborhood of point *P*. Light-blue line *PF* represents the flux line passing for the air-gap field passing through *P*

In presence of eccentricity, we have that

$$g_r < g_s \quad (1)$$

and conceptual uncertainty arises as to how to define the air-gap width at point *P*. Let us also consider the air-gap field flux line *FP* passing through point *P*. In the hypothesis of infinitely permeable stator and rotor cores, this line is orthogonally incident to both stator and rotor surfaces. A simple geometric reasoning thereby suggests that the point *F* must fall between *A* and *B* and, calling g_m ("magnetic" gap width) the length of line *FP*, we have:

$$g_r \le g_m \le g_s \quad (2)$$

From a physical viewpoint, the permeance function aims at quantifying the MMF drop associated to a given gap field line, hence it is reasonable to assume the air-gap width at point *P* coincides with g_m. Since g_m can be exactly determined only through a complete air-gap field computation, the approach followed hereinafter is to separately and exactly estimate g_s and g_r for all points *P*. This will give us a feeling of how g_s and g_r may differ (also in case of very large eccentricities) and of the error that we introduce if we accept to identify the magnetic gap width g_m with either g_s, or g_r, or their average.

8.2.1 Determination of g_r

Setting

$$\beta = \theta - \alpha \quad (3)$$

$$OP = R_s\,,\ AC = R_r\,,\ OC = \varepsilon \quad (4)$$

we can express segment *CP* from Carnot's theorem as:

$$CP = \sqrt{\varepsilon^2 + R_s{}^2 - 2R_s\varepsilon\cos\beta} \quad (5)$$

Hence g_r is simply given by:

$$g_r = BP = CP - R_r = \sqrt{\varepsilon^2 + R_s{}^2 - 2R_s\varepsilon\cos\beta} - R_r \quad (6)$$

8.2.2 Determination of gs

From elementary geometry relationships, we can write:

$$\frac{\varepsilon}{\sin\phi} = \frac{R_r}{\sin\beta} \quad (7)$$

from which:

$$\cos\phi = \sqrt{1 - \frac{\varepsilon^2}{R_r{}^2}\sin^2\beta} \quad (8)$$

Furthermore, the following relationship holds:

$$AO = AC\cos\phi + OC\cos\beta = R_r\cos\phi + \varepsilon\cos\beta \quad (9)$$

and substitution of (8) into (9) gives:

$$AO = \sqrt{R_r{}^2 - \varepsilon^2 \sin^2 \beta} + \varepsilon \cos \beta \quad (10)$$

This leads to estimate gs=AP as:

$$g_s = AP = R_s - AO = R_s - \sqrt{R_r{}^2 - \varepsilon^2 \sin^2 \beta} - \varepsilon \cos \beta \quad (11)$$

8.2.3 Comparison of gs and gr

Example diagrams of g_s and g_r versus β are provided in Fig. 11 for the case where R_s=25 mm, R_r=13.75 mm, R_s=5.83 mm, i.e. for the example geometry illustrated in Fig. 9.
To have an idea of how g_s and g_r differ from each other in the general case, it makes sense to consider the following ratio:

$$f(\beta) = \frac{g_s(\beta) - g_r(\beta)}{\left[g_s(\beta) + g_r(\beta)\right]/2} \quad (12)$$

which results from dividing the difference of the two quantities by their arithmetic mean. It is intuitive and would be easy to prove that the maximum error between g_s and g_r occurs for β=π/2 or β=3π/2 (see Fig. 11). Hence the maximum error could be expressed as:

$$f_{\max} = \frac{g_s(\pi/2) - g_r(\pi/2)}{\left[g_s(\pi/2) + g_r(\pi/2)\right]/2} \quad (13)$$

Substituting (6) and (11) into (13) and dividing both numerator and denominator by R_s gives:

$$f_{\max} = 2 - 4\frac{1 - g' - \sqrt{1+\varepsilon'^2}}{\sqrt{(1-g')^2 - \varepsilon'^2} - \sqrt{1+\varepsilon'^2} - g'} \quad (14)$$

where g' and ε' are adimensional quantities defined as follows:

$$\varepsilon' = \varepsilon / R_s, \; g' = \left(R_s - R_r\right)/R_s \quad (15)$$

which represent the eccentricity and the nominal gap expressed in per unit of the stator bore radius. For obvious physical reasons, the eccentricity cannot exceed the nominal gap, so (13) makes sense for $\varepsilon' \le g'$.
Hence, we can also express (13) as:

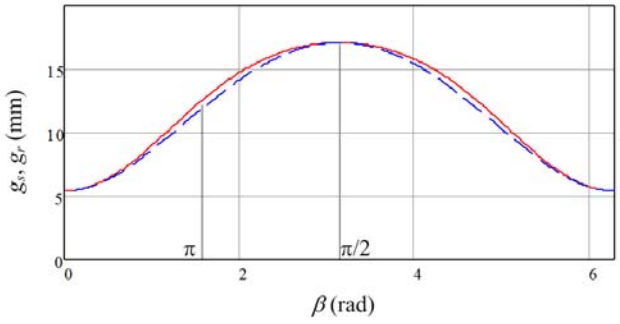

Fig. 11. Diagrams of g_s and g_r as a function of β for R_s=25 mm, R_r=13.75 mm and ε=5.83 mm.

$$f_{\max} = 2 - 4\frac{1 - g' - \sqrt{1 + (\kappa g')^2}}{\sqrt{(1 - g')^2 - (\kappa g')^2} - \sqrt{1 + (\kappa g')^2} - g'} \quad (16)$$

Where

$$\kappa = \varepsilon' / g' = \varepsilon / g \quad (17)$$

is a coefficient less than 1 that quantifies the eccentricity in relative terms with respect to the nominal gap.
The function (16) is plotted versus κ ranging between 0 and 1 for different possible values of normalized gap g', expressed in per unit of the stator bore as per (15). The diagram shows that for values of g' below 0.2 the function f_{max} take values below 0.025 (which means that the error between g_s and g_r, with respect to their arithmetic mean, is lower than 2.5%). Of course, considering values of g' above 0.2 seems definitely unrealistic because this would imply nominal gap widths larger than 20% of the stator bore. From this preliminary brief analysis, we can conclude that, for electric machines of practical interest and even for very large (extreme) rotor eccentricities (κ=1), the discrepancy between gap width estimations g_s and g_r is well below 2.5%. Therefore, in the rest of the chapter the two values will be considered interchangeable and, for the sake of commodity, reference will be made to g_r given its slightly easier mathematical expression.

8.3 Permeance Function Definition

Let us suppose to have a multiphase machine (that can be a conventional three-phase one as a particular case). The self inductance of a phase and the mutual inductance between two arbitrary phases can be computed through the winding function theory as [1], [2]:

$$m_{i,j}(x) = \mu_0 RL \int_0^{2\pi} w_i(\xi) w_j(\xi) p(\xi - x) d\xi \quad (18)$$

where x is an angular coordinate identifying the rotor position, i and j are integer indices that identify the phases (if i=j the self inductance is being computed), R is mean air-gap radius, L the core length, $w_i(x)$ and $w_j(x)$ are the winding functions of phases i, j and $p(x)$ is the permeance function accounting for the gap shape. Computation of inductances through (18) is not convenient as the equation involves an integral to be numerically solved. To overcome the problem, one generally considers the winding function and permenance function expansions in Fourier series:

$$w_i(\theta) = \sum_{n=0}^{\infty} W_n \cos\left(n(\theta - \gamma i)\right), \; p(\theta) = \sum_{n=0}^{\infty} P_n \cos\left(n\theta\right) \quad (19)$$

where γ is the phase progression [1], [2], so that (18) can be symbolically expanded yielding an easy-to-compute expression for $m_{i,j}(\theta)$ including Fourier series coefficients W_n, P_n [1], [2]. All this justifies the need to have the permeance function available as a Fourier series expansion.

By definition, the permenace function is the reciprocal of the gap function, which quantifies the gap width as a function of the angular coordinate θ in the stator reference frame (Fig. 1). In the case of an eccentric machine, it has been decided in the previous Section to identify the gap function with $g_r(\theta)$ given,

in accordance to (3) and (6), by:

$$g_r(\theta) = \sqrt{\varepsilon^2 + R_s{}^2 - 2R_s\varepsilon\cos(\theta - \alpha)} - R_r \quad (20)$$

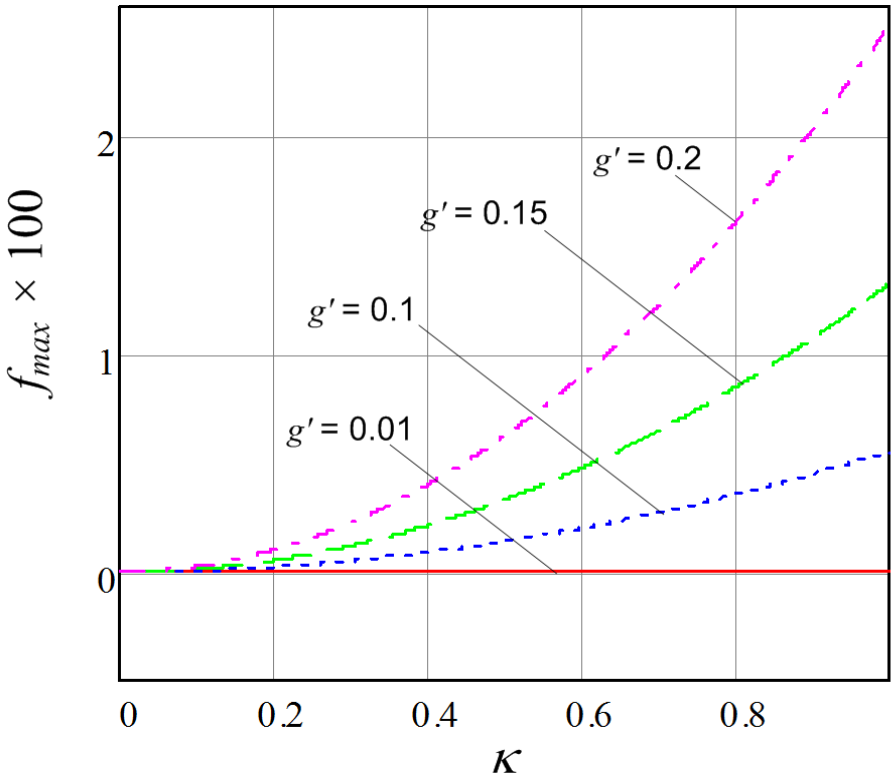

Fig. 12. Diagram of function f_{max} versus κ for various possible values of normalized gap (expressed in per unit of the stator bore).

so

$$p(\theta) = \frac{1}{g_r(\theta)} = \frac{1}{\sqrt{\varepsilon^2 + R_s{}^2 - 2R_s\varepsilon\cos(\theta - \alpha)} - R_r} \quad (21)$$

Since $g_r(\theta)$ is symmetrical with respect to $\theta=\alpha$, the Fourier series expansion for $p(\theta)$ can be expressed as:

$$p(\theta) = \sum_{k=0}^{\infty} P_k \cos(k(\theta - \alpha)) \quad (22)$$

and the problem is substantially to determine Fourier coefficients P_k. The formal definition for P_k is

$$P_0 = \frac{1}{2\pi}\int_0^{2\pi} p(\theta)d\theta \quad (23)$$

$$P_k = \frac{1}{\pi}\int_0^{2\pi} p(\theta)\cos(k\theta)d\theta \text{ , } k=1,2,\ldots \quad (24)$$

Substitution of (21) into (24) leads to integrals for which a symbolic expansion has been found impossible through any integration technique. Therefore, an alternative approach is hereinafter proposed consisting of two successive steps: firstly; a Taylor series expansion is derived for $p(\theta)$; secondly, the Taylor series expansion is plugged into (23)-(24) allowing for a symbolic integral solution, although in an asymptotical series form.

8.4 Expanding the Permeance Function in Taylor Series

For the sake of commodity, let us introduce an auxiliary variable x as follows:

$$x = 2R_s \varepsilon \cos(\theta - \alpha) \quad (25)$$

and redefine (21) as:

$$p(x) = \frac{1}{\sqrt{\varepsilon^2 + {R_s}^2 - x} - R_r} \quad (26)$$

This can be rewritten as:

$$p(x) = \frac{\sqrt{\varepsilon^2 + {R_s}^2 - x} + R_r}{\varepsilon^2 + {R_s}^2 - x - {R_r}^2} = \frac{\sqrt{\varepsilon^2 + {R_s}^2}\sqrt{1 - \frac{x}{\varepsilon^2 + {R_s}^2}} + R_r}{\left(\varepsilon^2 + {R_s}^2 - {R_r}^2\right)\left(1 - \frac{x}{\varepsilon^2 + {R_s}^2 - {R_r}^2}\right)} \quad (27)$$

At this point the following Taylor series expansion identity is recalled:

$$\sqrt{1+y} = \sum_{n=0}^{\infty} \frac{(-1)^n (2n)!}{4^n (1-2n)(n!)^2} y^n \quad (28)$$

Using it (27) becomes:

$$p(x) = \frac{\sqrt{\varepsilon^2 + {R_s}^2}\left[\sum_{m=0}^{\infty} \frac{(2m)!}{4^m (1-2m)(m!)^2}\left(\frac{x}{\varepsilon^2 + {R_s}^2}\right)^m\right] + R_r}{\left(\varepsilon^2 + {R_s}^2 - {R_r}^2\right)\left(1 - \frac{x}{\varepsilon^2 + {R_s}^2 - {R_r}^2}\right)} \quad (29)$$

As to the denominator, we can consider the Taylor series expansion identity:

$$\frac{1}{1-y}=\sum_{n=0}^{\infty}y^{n} \quad (30)$$

So (29) becomes:

$$p(x)=\frac{\sqrt{\varepsilon^{2}+R_{s}{}^{2}}\left[\sum_{m=0}^{\infty}\frac{(2m)!}{4^{m}(1-2m)(m!)^{2}}\left(\frac{x}{\varepsilon^{2}+R_{s}{}^{2}}\right)^{m}\right]+R_{r}}{\left(\varepsilon^{2}+R_{s}{}^{2}-R_{r}{}^{2}\right)}\times\sum_{q=0}^{\infty}\frac{x^{q}}{\left(\varepsilon^{2}+R_{s}{}^{2}-R_{r}{}^{2}\right)^{q}} \quad (31)$$

Equation (31) can be split in the sum of two terms:

$$p(\theta)=p_{1}(\theta)+p_{2}(\theta) \quad (32)$$

where:

$$p_{1}(\theta)=\sqrt{\varepsilon^{2}+R_{s}{}^{2}}\times\sum_{m=0}^{\infty}\sum_{q=0}^{\infty}\frac{(2m)!}{4^{m}(1-2m)(m!)^{2}}\frac{\left(2R_{s}\varepsilon\right)^{m+q}}{\left(\varepsilon^{2}+R_{s}{}^{2}-R_{r}{}^{2}\right)^{q+1}}\cos^{m+q}\left(\theta-\alpha\right) \quad (33)$$

$$p_{2}(\theta)=R_{r}\sum_{q=0}^{\infty}\frac{\left(2R_{s}\varepsilon\right)^{q}}{\left(\varepsilon^{2}+R_{s}{}^{2}-R_{r}{}^{2}\right)^{q}}\cos^{q}\left(\theta-\alpha\right) \quad (34)$$

Equations (32)-(34) provide the Taylor series expansion, in the variable $\cos(\theta-\alpha)$, which we shall use in (23)-(24) as explained in the next Section.

8.5 Determination of Fourier Coefficient for the Permeance Function

Substitution of (32)-(34) into (23)-(24) gives rise to some integrals that, apart from multiplicative coefficients, are:

$$\int_{0}^{2\pi}\cos(k\beta)\cos^{m+q}\beta\,d\beta\,,\ \int_{0}^{2\pi}\cos(k\beta)\cos^{q}\beta\,d\beta \quad (35)$$

These cannot be solved symbolically in a closed form. A solution of this kind of integrals through appropriate asymptotical series expansions is yet possible as derived in the Appendix of this chapter.
Using the results given in Appendix and after some lengthy but elementary algebraic manipulations, Fourier coefficients (23)-(24) can be finally determined as follows:

$$P_{0}=\sum_{m=0}^{M}\sum_{q=0}^{Q}\frac{\left(2\varepsilon R_{s}\right)^{m+q}\Gamma_{q,m}}{\left(\varepsilon^{2}+R_{s}{}^{2}\right)^{m-\frac{1}{2}}\left(\varepsilon^{2}+R_{s}{}^{2}-R_{r}{}^{2}\right)^{q+1}}+\sum_{q=0}^{Q}\frac{R_{r}\left(2\varepsilon R_{s}\right)^{q}\Lambda_{q,m}}{\left(\varepsilon^{2}+R_{s}{}^{2}-R_{r}{}^{2}\right)^{q+1}} \quad (36)$$

$$P_k = \sum_{m=0}^{M}\sum_{q=0}^{Q} \frac{2\left(2\varepsilon R_s\right)^{m+q} \sum_{u=0}^{k}\sum_{j=0}^{m+q+u}\sum_{r=0}^{k-u} \Phi_{k,m,q,j,r,u}}{\left(\varepsilon^2 + {R_s}^2\right)^{m-\frac{1}{2}}\left(\varepsilon^2 + {R_s}^2 - {R_r}^2\right)^{q+1}} + \sum_{q=0}^{Q} \frac{R_r\left(2\varepsilon R_s\right)^{q} \sum_{u=0}^{k}\sum_{j=0}^{q+u}\sum_{r=0}^{k-u} \Theta_{k,q,j,r,u}}{\left(\varepsilon^2 + {R_s}^2 - {R_r}^2\right)^{q+1}} \quad (37)$$

where:

$$\Gamma_{q,m} = \begin{cases} 0 & \text{if m + q is odd} \\ \dfrac{(2m)!(m+q)!}{(1-2m)(m!)^2 2^{3m+q}\left(\dfrac{m+q}{2}!\right)^2} & \text{if m + q is even} \end{cases} \quad (38)$$

$$\Lambda_{q,m} = \begin{cases} 0 & \text{if q is odd} \\ \dfrac{q!}{2^q\left(\dfrac{q}{2}!\right)^2} & \text{if q is even} \end{cases} \quad (39)$$

$$\Theta_{k,q,j,r,u} = \frac{(-1)^r}{i^{r-u}2^{q+k}} \frac{k!(q+u)!}{u!r!(k-u-r)!j!(q+u-j)!} \times \left[\cos\frac{(k-u)\pi}{2}\right]\delta_{q+k-2j-2r,0} \quad (40)$$

$$\Phi_{k,m,q,j,r,u} = \frac{(-1)^r}{(1-2m)4^m i^{k-u}2^{m+q+k}} \times \frac{(2m)!k!(m+q+u)!}{(m!)^2 u!r!(k-u-r)!j!(m+q+u-j)!}$$

$$\times \left[\cos\frac{(k-u)\pi}{2}\right]\delta_{m+q+k-2j-2r,0} \quad (41)$$

Constants M and Q that appear in (36)-(37) should theoretically tend to infinite. However, for the purpose of numerical computation, it is possible to truncate the sums to relatively low values of such constants, so that the practical calculation of (36)-(37) is not a computationally heavy process.

8.6 Numerical Assessment

As a numerical assessment, the permeance function of the machine topology shown in Fig. 9 (R_s=25 mm, R_r=13.75 mm and ε=5.83 mm, α=0.54 rad) is considered and approximated as:

$$p(\theta) = \sum_{k=0}^{K} P_k \cos\left(k(\theta - \alpha)\right) \quad (42)$$

with K being the integer at which the Fourier series is truncated and with Fourier coefficients P_k computed as per (36)-(41) with appropriate choice of integers M, Q. Such Fourier series approximation is then compared

to the actual function given by (21). The comparison is shown in Fig. 13 where the Fourier series approximation is performed using K=4, M=1 and Q=12.

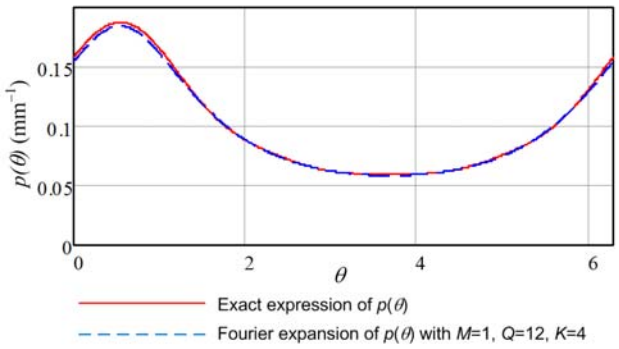

Fig. 13. Permeance function diagram (actual and Fourier-series approximation) for R_s=25 mm, R_r=13.75 mm and ε=5.83 mm, α=0.54 rad.

It can be observed that a very satisfactory matching is achieved even if the Fourier series is truncated to its first four terms and only two values for index m (i.e. m=0, m=1) are considered in (36)-(37). Further tests confirm that a definitely satisfactory Fourier series approximation is obtained with similar index ranges also for other machine topologies. For reduced eccentricity values, also the range for index q (spanning between 0 and Q) in (36)-(37) can be significantly reduced without remarkable precision losses.

8.7 Conclusion

This chapter has addressed the permeance function expansion in Fourier series for round-rotor electric machines subject to large eccentricity values. The reasons why a permenace function expression in the form of a Fourier series has been justified. From elementary geometric considerations, a suitably accurate permeance function expression has been derived for a machine with arbitrary rotor eccentricity. Then, this has been expanded resorting to Taylor series. Finally, Taylor series expansion has been used to calculate the coefficients of the final Fourier series expansion. Numerical assessments have been provided to show that good precision levels can be attained with relatively low computation burden since the series involved in the proposed formulation converge very rapidly to their asymptotical values and can be therefore truncated to the first few terms.

8.8 Appendix

In this appendix the problem is addressed of finding a suitable symbolical solution for the integral having the general form:

$$\int_0^{2\pi} \cos(nz)\cos^m z \, dz \quad (43)$$

where m, n are arbitrary positive integers. To approach the problem let us consider the identity [7]-[8]:

$$\cos(nz)=\sum_{k=0}^{n}\frac{n!}{k!(n-k)!}\left(\cos^{k} z\right)\left(\sin^{n-k} z\right)\cos\frac{(n-k)\pi}{2} \quad (44)$$

This leads (43) to be written as:

$$\int_{0}^{2\pi}\cos(nz)\cos^{n} z\,dz=\sum_{k=0}^{n}\frac{n!}{k!(n-k)!}\cos\frac{(n-k)\pi}{2}\int_{0}^{2\pi}\left(\cos^{m+k} z\right)\left(\sin^{n-k} z\right)dz \quad (45)$$

Using the complex notation for sine and cosine functions, the integrand $\left(\cos^{m+k} z\right)\left(\sin^{n-k} z\right)$ can be expanded as follows:

$$\left(\cos^{m+k} z\right)\left(\sin^{n-k} z\right)=\left(\frac{e^{iz}+e^{-iz}}{2}\right)^{m+k}\left(\frac{e^{iz}-e^{-iz}}{2i}\right)^{n-k} \quad (46)$$

and using binominal coefficient expansions we have:

$$\left(\frac{e^{iz}+e^{-iz}}{2}\right)^{m+k}\left(\frac{e^{iz}-e^{-iz}}{2i}\right)^{n-k}=\sum_{j=0}^{m+k}\left[\frac{1}{2^{m+k}}\frac{(m+k)!}{(m+k-j)!}\left(e^{iz}\right)^{m+k-j}\left(e^{-iz}\right)^{j}\right]\times$$

$$\times\sum_{r=0}^{n-k}\left[\frac{1}{(2i)^{n-k}}\frac{(n-k)!}{(n-k-r)!}\left(e^{iz}\right)^{n-k-r}\left(-e^{-iz}\right)^{r}\right]=\sum_{j=0}^{m+k}\left[\frac{1}{2^{m+k}}\frac{(m+k)!}{(m+k-j)!}e^{iz(m+k-2j)}\right]\times$$

$$\times\sum_{r=0}^{n-k}\left[\frac{(-1)^{r}}{(2i)^{n-k}}\frac{(n-k)!}{(n-k-r)!}e^{iz(n-k-2r)}\right] \quad (47)$$

This leads to the final identity:

$$\left(\cos^{m+k} z\right)\left(\sin^{n-k} z\right)=\sum_{j=0}^{m+k}\sum_{r=0}^{n-k}\left[\frac{(-1)^{r}}{(2i)^{n-k}}\frac{(n-k)!}{(n-k-r)!}\frac{1}{2^{m+k}}\frac{(m+k)!}{(m+k-j)!}e^{iz(m+n-2j-2r)}\right] \quad (48)$$

Equation (48), used in (45), enables us to easily expand the integral:

$$\int_{0}^{2\pi}\left(\cos^{m+k} z\right)\left(\sin^{n-k} z\right)dz \quad (49)$$

considering that:

$$\int_{0}^{2\pi}e^{iz(m+n-2j-2r)}dz=\begin{cases}2\pi & \text{if } m+n-2j-2r=0\\ 0 & \text{otherwise}\end{cases} \quad (50)$$

Hence the symbolical expansion for the integral (43) will be as follows:

$$\int_0^{2\pi} \cos(nz)\cos^n z\, dz =$$

$$= \sum_{k=0}^{n} \left\{ \frac{n!(m+k)!}{k!(2i)^{n-k}\, 2^{m+k}} \cos\frac{(n-k)\pi}{2} \times \sum_{j=0}^{m+k} \sum_{r=0}^{n-k} \left[\frac{(-1)^r}{r!(n-k-r)!(m+k-j)!} 2\pi\, \delta_{m+n-2j-2r,0} \right] \right\} \quad (51)$$

where $\delta_{s,t}$ is the Kroneker symbol defined so that:

$$\delta_{s,t} = \begin{cases} 1 & \text{if } s = t \\ 0 & \text{otherwise} \end{cases} \quad (52)$$

8.9 References

[1] J. Figueroa, J. Cros, and P. Viarouge, "Generalized transformations for polyphase phase-modulated motors," *IEEE Transaction on Energy Conversion*, vol. 21, no. 2, pp. 332–341, Jun. 2006.

[2] A. Tessarolo, "Accurate Computation of Multiphase Synchronous Machine Inductances Based on Winding Function Theory", *IEEE Transactions on Energy Conversion,* vol.27, no.4, pp.895-904, Dec. 2012.

[3] C. Bruzzese, "Diagnosis of Eccentric Rotor in Synchronous Machines By Analysis of Split-Phase Currents - Part I: Theoretical Analysis", *IEEE Transactions on Industrial Electronics,* in press.

[4] C. Bruzzese, "Diagnosis of Eccentric Rotor in Synchronous Machines By Analysis of Split-Phase Currents-Part II: Experimental Analysis", *IEEE Transactions on Industrial Electronics,* in press.

[5] I. Tabatabaei, J. Faiz, H. Lesani, M.T. Nabavi-Razavi, "Modeling and Simulation of a salient-pole synchronous Generator with dynamic eccentricity using modified winding function theory", *IEEE Transactions on Magnetics,* vol. 40, no. 3, pp.1550-1555, May 2004.

[6] N.A. Al-Nuaim, H.A. Toliyat, "A novel method for modeling dynamic air-gap eccentricity in synchronous machines based on modified winding function theory", *IEEE Transactions on Energy Conversion,* vol. 13, no. 2, pp.156-162, Jun 1998.

[7] W. H. Beyer, *CRC Standard Mathematical Tables, 28th ed. Boca Raton*, CRC Press, 1987.

[8] T. J. Bromwich and T. M. MacRobert, *An Introduction to the Theory of Infinite Series, 3rd ed.* New York, Chelsea, pp. 202-207, 1991.

9 Improved Analytical Computation of Rotor Rectangular Slot Leakage Inductance in Squirrel-Cage Induction Motors

9.1 Introduction

Squirrel-cage induction motors represent the most widespread category of electric machines being used in today's industrial [1] and vehicle traction [2]-[3] applications. In order to predict the steady-state performance of these machines, the use of Finite Element Analysis (FEA) [4] or numerical meshless methods [5] is certainly the choice leading to the best accuracy levels. As a faster and simpler alternative to FEA, however, it is still a common practice to solve motor equivalent circuit [6]. This requires equivalent circuit lumped parameters to be estimated, including rotor leakage inductance. In addition to FEA-based approaches [7], simple analytical formulas can be found in the literature for this purpose [8], [9]. This chapter, in particular, focuses on the computation of rotor slot leakage inductance in squirrel-cage induction motors having rectangular rotor bars [10]. The leakage inductance of such rotor bars is determined by direct solution of Poisson's equation in the slot domain, similarly to what is presented in [11] for trapezoidal bar shapes. Differently from [11], however, this chapter arrives at an explicit ready-to-use calculation formula. This is validated against FEA simulations for different rectangular bar aspect ratios and is shown to give very accurate results, with errors in the order of 2%. Conversely, traditional formulas available from the literature [8], [9] are shown to give much larger errors (above 10%), especially for height to width bar ratios lower than 5. A limit of the proposed approach is that it does not account for magnetic saturation which is known to occur especially in the iron bridge region [12] and which could be considered either through heuristic corrections to analytical formulas [8], [9], [12] or by using numerical computation techniques [5], [7].

9.2 Geometric model and physical assumptions

The assumed rotor slot geometry is shown in Fig. 1, where W and H are the rotor bar dimensions and d, w are the air-bridge dimensions. A Cartesian xyz reference frame is introduced as show in Fig. 1, with its origin placed on the bottom-left corner of the rectangular bar.

The physical assumptions made to study the leakage field inside the slot are listed next.

a) The rectangular bar carries a uniform current density J, positive if oriented in the z direction, and, hence, a total current

$$I = J\,H\,W \quad (1)$$

b) The rotor core is infinitely permeable, so magnetic saturation is neglected.
c) The magnetic field in the air bridge is supposed to be uniform and oriented parallel to the x axis.
d) End-effects are neglected, hence the magnetic field is supposed to lie in the xy plane and the vector potential to be aligned along the z axis.

The hypothesis a) limits the applicability of the treatment to the steady-state motor operation close to rated slip values, wherein the rotor current frequency is so small that skin or eddy current effects can be disregarded [8], [9].

The hypothesis b) could make the treatment suitable only for unsaturated machines. Actually, the effects of iron bridge saturation can be, to a certain approximation, taken into account by suitably changing the slot opening width *d* as discussed in [9]. As mentioned in the same reference, the model depicted in Fig. 1 can be also applied to the study of closed slots by treating the slot opening as a fictitious one (of appropriate width) which mimics the effect of the iron bridge saturation [9].

Assumption c) may not be rigorously correct, but can be reasonably accepted as the slot opening is usually very small compared to the overall slot dimensions.

Assumption d) is widely accepted in the study of electric machines and is necessary to reduce the analytical problem to a 2D one.The rotor core is infinitely permeable, so magnetic saturation is neglected.
The magnetic field in the air bridge is supposed to be uniform and oriented parallel to the *x* axis.
End-effects are neglected, hence the magnetic field is supposed to lie in the *xy* plane and the vector potential to be aligned along the *z* axis.

The hypothesis a) limits the applicability of the treatment to the steady-state motor operation close to rated slip values, wherein the rotor current frequency is so small that skin or eddy current effects can be disregarded [8], [9].

The hypothesis b) could make the treatment suitable only for unsaturated machines. Actually, the effects of iron bridge saturation can be, to a certain approximation, taken into account by suitably changing the slot opening width *d* as discussed in [9]. As mentioned in the same reference, the model depicted in Fig. 1 can be also applied to the study of closed slots by treating the slot opening as a fictitious one (of appropriate width) which mimics the effect of the iron bridge saturation [9].

Assumption 0 may not be rigorously correct, but can be reasonably accepted as the slot opening is usually very small compared to the overall slot dimensions.

Assumption 0 is widely accepted in the study of electric machines and is necessary to reduce the analytical problem to a 2D one.

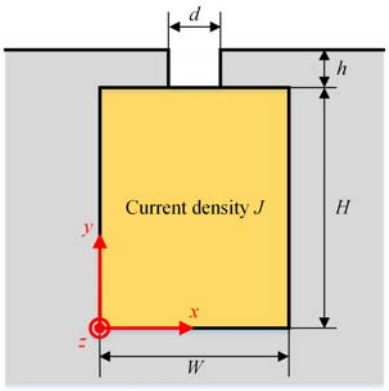

Fig. 14. Rotor slot geometry.

9.3 Poisson's equation and boundary conditions for the slot domain

9.3.1 Field solution in the slot domain

With reference to the geometric model shown in Fig. 1, the vector potential A (z component) in the rectangular bar region must satisfy the following Poisson's equation in Cartesian coordinates [13]:

$$\frac{\partial^2 A}{\partial^2 x}+\frac{\partial^2 A}{\partial^2 x}=-\mu_0 J \quad (2)$$

$$0\le x\le W\ ,\ 0\le y\le H$$

where μ_0 is the magnetic permeability of the air and the vector potential A is related to the magnetic flux density components B_x and B_y along x and y directions through the following relationships [13]:

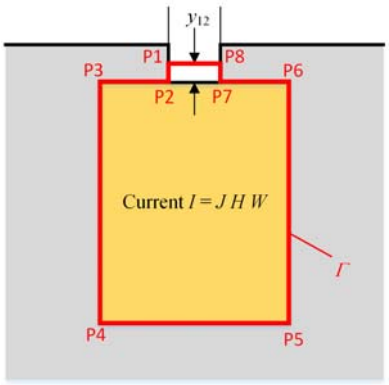

Fig. 2. Closed path used to determine the magnetic field in the air bridge.

$$B_x(x,y)=\frac{\partial A}{\partial y},\ B_y(x,y)=-\frac{\partial A}{\partial x} \quad (3)$$

As regards the magnetic field in the air bridge, it can be determined by applying Ampere's circuital law to the closed loop Γ having vertices P1, …, P8 and shown in Fig. 2, where

$$0\le y_{12}\le h \quad (4)$$

Since the magnetic field is orthogonal to all the points of the contour except for the segment P1-P8, we can write Ampere's circuital law as follows:

$$\oint_{\Gamma}\mathbf{H}\,d\mathbf{s}=\int_{P8}^{P1}\mathbf{H}\,d\mathbf{s}=-H_{bridge}d=-\frac{B_{bridge}}{\mu_0}d=J\,W\,H \quad (5)$$

where H_{bridge} and B_{bridge} are the magnetic field and flux density in the air bridge, positive if pointing in the x axis direction, negative otherwise. From (5) the flux density in the air bridge region can be written as:

$$B_{bridge}=-\mu_0 J\frac{W\,H}{d}=-\mu_0\frac{I}{d} \quad (6)$$

Regarding boundary conditions in the rectangular bar region where (2) is to be solved, the assumed infinite permeability of the core yields:

$$B_y(0,y) = -\frac{\partial A}{\partial x}(0,y) = 0\,,\ 0 \le y \le H \quad (7)$$

$$B_y(W,y) = -\frac{\partial A}{\partial x}(W,y) = 0\,,\ 0 \le y \le H \quad (8)$$

$$B_x(x,0) = \frac{\partial A}{\partial y}(x,0) = 0\,,\ 0 \le x \le W \quad (9)$$

On the top domain border ($y=H$), which includes the slot opening, the tangential flux density takes the form shown in Fig. 3. It can be seen that B_x along such border is zero (due to the infinite core permeability) except for the slot opening region, where it takes the value given by (6). In symbols:

$$f(x) = B_x(x,H) = \frac{\partial A}{\partial y}(x,H) = \begin{cases} B_{bridge} & \text{if } x \in \left[0, \dfrac{W-d}{2}\right] \cup \left[\dfrac{W+d}{2}, W\right] \\ 0 & \text{if } x \in \left]\dfrac{W-d}{2}, \dfrac{W+d}{2}\right[\end{cases} \quad (10)$$

The same function can be expanded in Fourier series as follows:

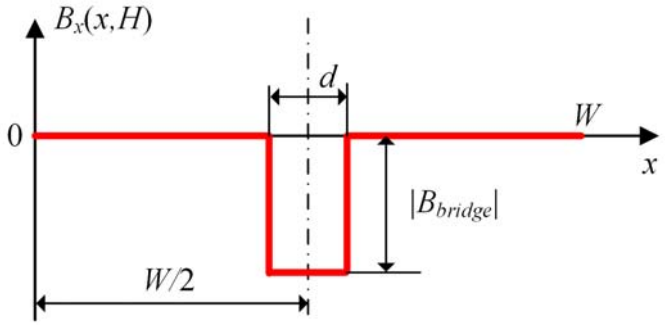

Fig. 3. Tangential flux density diagram, along the top side of the rectangular slot.

$$f(x) = F_0 + \sum_{n=1,2,3,\ldots} F_n \cos\left(\frac{\pi}{W} n x\right) \quad (11)$$

where Fourier coefficients are:

$$F_0 = \frac{B_{bridge}\, d}{W} = -\frac{\mu_0\, I}{W} \quad (12)$$

$$F_n = \frac{4\, B_{bridge}}{\pi\, n} \cos\left(\frac{\pi\, n}{2}\right) \cos\left(\frac{\pi\, d\, n}{2W}\right) = -\frac{4 \mu_0\, I}{\pi\, n\, d} \cos\left(\frac{\pi\, n}{2}\right) \cos\left(\frac{\pi\, d\, n}{2W}\right) \quad (13)$$

having used (6) for B_{bridge}.

Equations (7), (8), (9), (10) define a set of Neumann boundary conditions which enable one to solve Poisson's equation (2) in the rectangular bar domain.

The solution to (2) subject to boundary conditions (7), (8), (9), (10) is sought in this Section in the following form [13]:

$$A(x,y) = A_0 y^2 + \sum_{n=1,2,3,\ldots} A_n \cosh\left(\frac{\pi}{W} n y\right) \cos\left(\frac{\pi}{W} n x\right) \quad (14)$$

Accordingly, the flux density in the slot domain is derived from (3) to have the x, y components below:

$$B_x(x,y) = 2A_0 y + \sum_{n=1,2,3,\ldots} \frac{A_n \pi\, n}{W} \sinh\left(\frac{\pi}{W} n y\right) \cos\left(\frac{\pi}{W} n x\right) \quad (15)$$

$$B_y(x,y) = \sum_{n=1,2,3,\ldots} \frac{A_n \pi\, n}{W} \cosh\left(\frac{\pi}{W} n y\right) \sin\left(\frac{\pi}{W} n x\right) \quad (16)$$

By direct substitution of (14) into (2) and after symbolical expansion of the derivatives, it can be easily seen that (14) satisfies Poisson's equation (2) if and only if the coefficient A_0 takes the following value

$$A_0 = -\frac{\mu_0 J}{2} \quad (17)$$

Furthermore, using (15), (16), one can easily prove that (14) also satisfies the boundary conditions (7), (8), (9) along the bar sides which do not include the slot opening.

In order to determine coefficients A_n, for n=1, 2, 3, …, it is necessary to impose that the additional Neumann boundary condition (10) is satisfied. This leads to write the following equations:

$$2A_0 H = F_0 \quad (18)$$

$$\frac{A_n \pi\, n}{W} \sinh\left(\frac{\pi}{W} n H\right) = F_n, \quad n=1, 2, 3, \ldots \quad (19)$$

with F_0, F_1, F_2, … representing Fourier series coefficients, given by (12)-(13), for the function $f(x)$.

Considering (12) and (1), it can be seen that (18) is automatically satisfied if A_0 is set as per (17).

From (19) and (13), coefficients A_n are finally determined as follows:

$$A_n = -\frac{4\mu_0\, I\, W}{\pi^2\, d\, n^2} \frac{\sin\left(\frac{\pi\, d\, n}{2W}\right)\cos\left(\frac{\pi\, n}{2}\right)}{\sinh\left(\frac{\pi\, H\, n}{2W}\right)},\ n=1, 2, 3, \ldots \quad (20)$$

Equations (15), (16), with coefficients A_0, A_1, A_2, … given by (17) and (20) fully determine the magnetic flux density in the rectangular bar region.

9.3.2 Slot leakage inductance calculation

The slot leakage inductance L_{bar} of an individual rotor bar can be determined by computing the magnetic energy E_m stored in the slot (bar and opening regions) and then writing [8], [9]:

$$L_{bar} = \frac{2\, E_m}{I^2} \quad (21)$$

where I is the total current (1) flowing through the bar. Calling L the machine core length, the magnetic energy in the overall slot region can be written as:

$$E_m = E_{m,op} + E_{m,bar} \quad (22)$$

where $E_{m,op}$ is the energy stored in the slot opening (air bridge) region:

$$E_{m,op} = \frac{L\, d\, h}{2\mu_0} B_{bridge}{}^2 = \frac{L\, d\, h}{2\mu_0}\left(\frac{\mu_0\, I}{d}\right)^2 = \frac{\mu_0\, L\, h\, I^2}{2\, d} \quad (23)$$

and $E_{m,bar}$ is the magnetic energy stored in the bar region:

$$E_{m,bar} = \frac{L}{2\mu_0}\int_0^H\int_0^W \left[B_x(x,y) + B_y(x,y)\right]^2 dxdy \quad (24)$$

After some symbolical expansions and algebraic manipulations which are not included for the sake of brevity, it is possible to found an explicit solution for the double integral in (24) by substituting the flux density components (15), (16) into (24). This leads to the final expression below:

$$E_{m,bar} = \frac{L\, I^2 \mu_0}{2W}\left\{\frac{H}{3} + \frac{W^3}{\pi^3 d^2}\sum_{n=1,2,3\ldots} \frac{\sin^2\left(\frac{\pi\, d\, n}{W}\right)}{n^3\, \tanh\left(\frac{2\,\pi\, d\, n}{W}\right)}\right\} \quad (25)$$

Finally, from (21)-(25) the expression for the bar leakage inductance is obtained in the form below:

$$L_{bar} = \mu_0 L \left\{ \frac{h}{d} + \frac{H}{3W} + \frac{W^2}{\pi^3 d^2} \sum_{n=1,2,3,\ldots} \frac{\sin^2\left(\frac{\pi d n}{W}\right)}{n^3 \tanh\left(\frac{2\pi d n}{W}\right)} \right\} \quad (26)$$

At this point, we can recall that the simplified formula for the leakage inductance of a rectangular bar embedded in a semi-closed slot according to the literature [9] is:

$$L'_{bar} = \mu_0 L \left(\frac{h}{d} + \frac{H}{3W} \right) \quad (27)$$

It therefore appears that the approximated leakage inductance L'_{bar} differs from the more accurate expression (26) derived in this chapter only by the third term between curled brackets in (26), i.e.:

$$L_{bar} - L'_{bar} = \frac{\mu_0 L W^2}{\pi^3 d^2} \sum_{n=1,2,3,\ldots} \frac{\sin^2\left(\frac{\pi d n}{W}\right)}{n^3 \tanh\left(\frac{2\pi d n}{W}\right)} \quad (28)$$

9.4 Accurate model validation through FEA and comparison with the simplified formula

In this Section the proposed accurate formula for the slot leakage computation in rectangular semi-closed slots of squirrel-cage induction motors, given by (26), is assessed by comparison against FEA. Furthermore, it is compared to the simplified formula, given by (27), available from the literature. The model adopted for the FEA assessment is represented in Fig. 4 and is characterized by the dimensions given in Table I, where the meaning of the symbols is illustrated in Fig. 1.

TABLE I

H	50 mm	***W***	10 mm	***h***	1 mm	***d***	2 mm

The bar leakage inductance is estimated by FEA, by the proposed accurate formula (26) and by the simplified one (27), for different bar heights H, while parameters W, d and h are left the same as per Table I. The results are given in Fig. 5, which shows that the proposed approach leads to an excellent accordance with FEA for all bar aspect ratios. Conversely, the values obtained with the approximated formula (27) exhibit a sort of practically constant offset [corresponding to (28)] with respect to FEA and to the new proposed expression (26). Such an offset appears not to change significantly with the bar aspect ratio [(28) does depend on W but not on H, in fact]. In terms of percent error, the situation is illustrated in Fig. 6. This shows that the proposed accurate formula leads to errors below 2% for any bar aspect ratio, while the approximated formula gives errors between 10% and 40% for H/W ratios below 5.5. In general, the accuracy of the simplified formula improves as the H/W ratio increases.

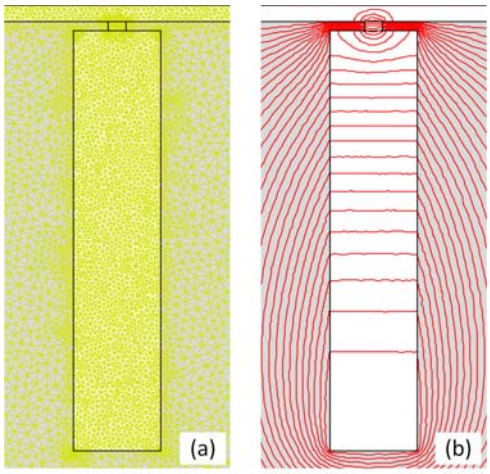

Fig. 4. (a) Slot meshed model; (b) Model FEA solution (H=50 mm).

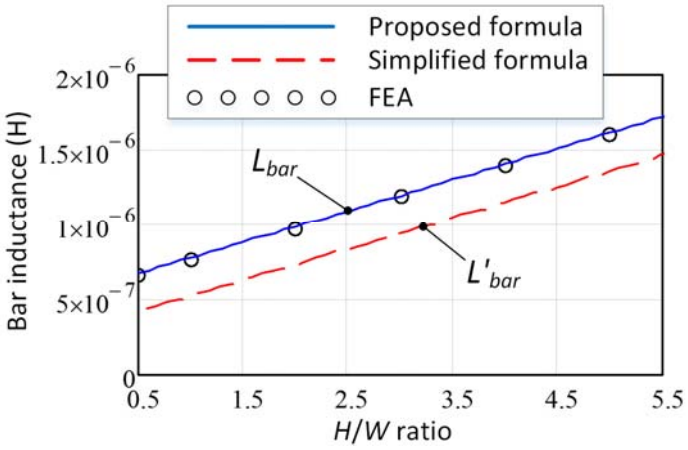

Fig. 5. Rotor bar inductance evaluation with the proposed analytical formula, with the simplified formula available from the literature and with FEA, as a function of the H/W ratio.

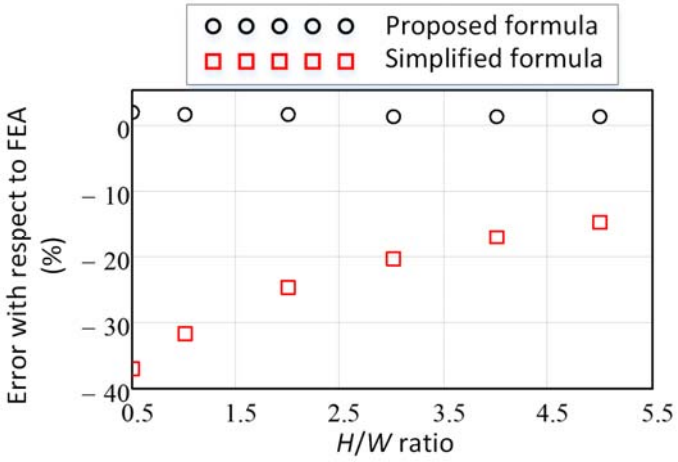

Fig. 6. Percent error (with respect to FEA) of the slot leakage inductance estimation with the proposed and simplified analytical formulas.

9.5 Conclusion

In this chapter the rotor slot leakage inductance of squirrel-cage induction motors with rectangular bars has been investigated through the analytical solution of Poisson's equation for the magnetic vector potential in the rotor slot domain. The analysis has led to identify a new explicit easy-to-use formula for slot leakage inductance estimation. Its accuracy has been successfully assessed by FEA for different slot aspect ratios, showing errors below 2% in all cases. The proposed formula has been also compared to the simplified one available from the literature, showing that the latter yields errors above 10% which increase as the bar height-to-width ratio decreases.

9.6 References

[1] A. Boglietti, A.M. El-Refaie, O. Drubel, A.M. Omekanda, N. Bianchi, E.B. Agamloh, M. Popescu, A. Di Gerlando, J.B. Bartolo, "Electrical Machine Topologies: Hottest Topics in the Electrical Machine Research Community", *IEEE Industrial Electronics Magazine,* vol.8, no.2, pp.18,30, June 2014.

[2] A.M. El-Refaie, "Motors/generators for traction/propulsion applications: A review", *IEEE Vehicular Technology Magazine,* vol.8, no.1, pp.90-99, March 2013.

[3] I. Boldea, L.N. Tutelea, L. Parsa, D. Dorrell, "Automotive Electric Propulsion Systems With Reduced or No Permanent Magnets: An Overview", *IEEE Transactions on Industrial Electronics,* vol.61, no.10, pp.5696-5711, Oct. 2014.

[4] Youpeng Huangfu, Shuhong Wang, Jie Qiu, Haijun Zhang, Guolin Wang, Jianguo Zhu, "Transient Performance Analysis of Induction Motor Using Field-Circuit Coupled Finite-Element Method", *IEEE Transactions on Magnetics,* vol. 50, no. 2, pp.873-876, Feb. 2014.

[5] E.H.R. Coppoli, R.C. Mesquita, R.S. Silva, "Induction Machines Modeling With Meshless Methods", *IEEE Transactions on Magnetics,* vol. 48, no. 2, pp. 847-850, Feb. 2012.

[6] A. Boglietti, A. Cavagnino, M. Lazzari, "Computational Algorithms for Induction-Motor Equivalent Circuit Parameter Determination—Part I: Resistances and Leakage Reactances", *IEEE Transactions on Industrial Electronics,* vol.58, no.9, pp.3723,3733, Sept. 2011.

[7] Zaixun Ling, Libing Zhou, Siyuan Guo, Yi Zhang, "Equivalent Circuit Parameters Calculation of Induction Motor by Finite Element Analysis", *IEEE Transactions on Magnetics,* vol. 50, no. 2, pp. 833-836, Feb. 2014.

[8] P. L. Alger, *Induction Machines*, 2nd ed. New York: Gordon and Breach,1970.

[9] I. Boldea and S. A. Nasar, *The Induction Machine Handbook*. Boca Raton, FL: CRC Press, 2002.

[10] A. Dalal, M.N. Ansari, P. Kumar, "A Novel Steady-State Model of a Hybrid Dual Rotor Motor Comprising Electrical Equivalent Circuit and Performance Equations", *IEEE Transactions on Magnetics,* vol.50, no.12, pp. 1-11, Dec. 2014.

[11] K. Boughrara, N. Takorabet, R. Ibtiouen, O. Touhami, F. Dubas, "Analytical Analysis of Cage Rotor Induction Motors in Healthy, Defective and Broken Bars Conditions", *IEEE Transactions on Magnetics,* 2014, in press, early access article available on IEEEXplore.

[12] A. Boglietti, R.I. Bojoi, A. Cavagnino, P. Guglielmi, A. Miotto, "Analysis and Modeling of Rotor Slot Enclosure Effects in High-Speed Induction Motors", *IEEE Transactions on Industry Applications,* vol.48, no.4, pp.1279-1287, July-Aug. 2012.

[13] J. D. Jackson, *Classical Electrodynamics*, John Wiley and Sons, New York, 1999.

10 An Improved Analytical Expression for Computing the Leakage Inductance of a Circular Bar in a Semi-Closed Slot

10.1 Introduction

Round conductors embedded in semi-closed slots are often used in electric machinery, such as in the squirrel cage of induction motors [1], [2] or in the damper winding of synchronous generators [3]. Under some circumstances, for example to predict the steady-state performance of a squirrel-cage induction motor at rated slip through its equivalent circuit [4], [5], it is useful to determine the leakage inductance of such circular conductors neglecting eddy-current and magnetic saturation effects. The most accurate method to accomplish the task is to use Finite Element Analysis (FEA) [4] or numerical meshless methods [6], but this may results in a significant computational burden in addition to requiring machine geometrical models to be prepared. For the purpose of a fast computation, simple analytical formulas available in the literature [1], [2], [5] are still commonly used. The problem of these formulas is that they assume quite crude simplifying hypotheses about slot leakage flux distribution, resulting in possible remarkable errors. In this chapter, a new improved expression is derived for the leakage inductance of a round conductor embedded in a semi-closed slot. The formulation is obtained by the direct solution of Poisson's equation in the slot domain, similarly to what is done in [7] for a trapezoidal conductor shape. Differently from [7], however, this chapter arrives at an explicit ready-to-use leakage inductance expression that can be readily applied in the engineering practice. The precision of the proposed formula is assessed against FEA considering various possible bar and slot-opening dimensions, showing that a very good accuracy, with errors in the order of 2%, can be achieved in any case. Conversely, the simplified formulas available in the literature [1], [2] are shown to give possibly imprecise results, with errors (with respect to FEA) which can be 20% or higher for some bar and slot opening dimensions.

10.2 Geometric model and physical assumptions

The assumed slot and bar geometry is shown in Fig. 1, where R is the bar radius, O is the bar center and d, h are the slot opening dimensions.

A polar coordinate system, centered in O, is introduced so that any point P in the bar domain is identified by the two coordinates r, θ as indicated in Fig. 1. The angle δ corresponding to the slot opening is defined as:

$$\delta = d / R \quad (1)$$

The physical assumptions made to study the leakage field inside the slot are listed next.

a) The circular bar carries a uniform current density J, positive if pointing out of the page, and, hence, a total current

$$I = J \, \pi \, R^2 \quad (2)$$

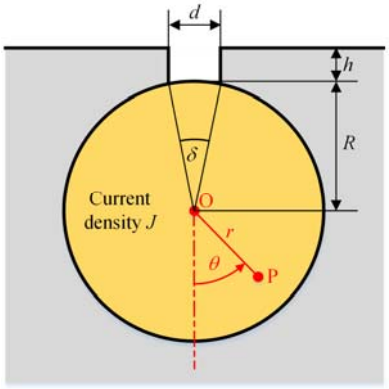

Fig. 15. Rotor slot geometry.

b) The rotor core is infinitely permeable, i.e. magnetic saturation is neglected.
c) The magnetic field in the slot opening is supposed to be uniform and orthogonal to slot opening sides.
d) End-effects are neglected, hence the magnetic field is supposed to lie in the plane and the vector potential is assumed parallel to the bar axis.

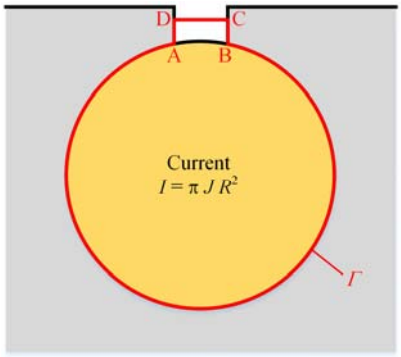

Fig. 2. Closed path used to find the magnetic field in the slot opening.

The hypothesis a) limits the applicability of the treatment to the operating conditions where no significant eddy current or skin effects arise, such as in the induction motor squirrel cage at or near the rated slip [1], [2].

The hypothesis b) could make the treatment suitable only for unsaturated machines. Actually, the effects of iron bridge saturation can be, to a certain approximation, taken into account by suitably changing the slot opening width *d* as discussed in [1]. As mentioned in the same reference, the model depicted in Fig. 1 can be also applied to the study of closed slots by treating the slot opening as a fictitious one (of appropriate width) which mimics the effect of the iron bridge saturation.

Assumption 0 may not be rigorously correct, but can be reasonably accepted as the slot opening is usually very small compared to the overall slot dimensions.

Assumption 0 is widely accepted in the study of electric machines and is necessary to reduce the analytical problem to a 2D one.

10.3 Poisson's equation and boundary conditions in the slot domain

10.3.1 Field solution in the slot domain

With reference to the geometric model shown in Fig. 1, the vector potential A (component along bar axis) in the circular bar region must satisfy the following Poisson's equation in polar coordinates [7], [8]:

$$\frac{1}{r}\frac{\partial}{\partial r}r\frac{\partial A}{\partial r}+\frac{1}{r^2}\frac{\partial^2 A}{\partial^2 \theta}=-\mu_0 J \quad (3)$$

$$0 \le r \le R\,,\ 0 \le \theta \le 2\pi$$

where μ_0 is the magnetic permeability of the air and the vector potential A is related to the radial and azimuthal flux density components B_r and B_θ through the relationships [8]:

$$B_r(r,\theta)=\frac{1}{r}\frac{\partial A}{\partial \theta},\ B_\theta(r,\theta)=-\frac{\partial A}{\partial r} \quad (4)$$

As regards the magnetic field in the slot opening, it can be determined by applying Ampere's circuital law to the closed loop Γ shown in Fig. 2. Since the magnetic field is orthogonal to all the points of the contour except for the segment DC, we can write Ampere's circuital law as follows:

$$\oint_{\Gamma}\mathbf{H}\,d\mathbf{s}=\int_C^D\mathbf{H}\,d\mathbf{s}=H_{op}d=\frac{B_{op}}{\mu_0}d=I=J\,\pi\,R^2 \quad (5)$$

where H_{op} and B_{op} are the magnetic field and flux density in the slot opening. From (5) the flux density in the air bridge region can be written as:

$$B_{op}=\mu_0\frac{I}{d} \quad (6)$$

Regarding boundary conditions in the circular bar region where a solution to (3) is searched for, the assumed infinite permeability of the core causes the tangential flux density B_θ on the bar periphery (r=R) to be everywhere null except for the slot opening region, where it takes the value (6). In symbols the boundary condition can be written as:

$$f(\theta)=B_\theta(R,\theta)=-\frac{\partial A}{\partial r}(R,\theta)=\begin{cases}B_{op} & \text{if } \theta\in\left[0,\pi-\dfrac{\delta}{2}\right]\cup\left[\pi+\dfrac{\delta}{2},2\pi\right]\\ 0 & \text{if } \theta\in\left]\pi-\dfrac{\delta}{2},\pi+\dfrac{\delta}{2}\right[\end{cases} \quad (7)$$

This function (whose diagram is plotted in Fig. 3) can be expanded in Fourier series as follows:

$$f(x) = F_0 + \sum_{n=1,2,3,\ldots} F_n \cos(nx) \quad (8)$$

where Fourier coefficients can be easily found to be:

$$F_0 = \frac{\mu_0 I}{2\pi R} \quad (9)$$

$$F_n = \frac{2\mu_0 I}{\pi n d}(-1)^n \sin\left(\frac{d\, n}{2R}\right) \quad (10)$$

Equation (7) defines a Neumann boundary condition which enables one to solve Poisson's equation (3) in the circular bar domain.

Under the hypothesis that the separation of variable technique applies, the general solution to (3) can be expressed in the following form [7], [8]:

$$A(r,\theta) = A_{s0}\, r^2 + A_{\ell 0} \ln r + \sum_{n=1,2,3,\ldots} \left[A_n^+ r^n + A_n^- r^{-n}\right]\cos(n\theta) \quad (11)$$

with suitable coefficients A_{s0}, $A_{\ell 0}$, A_n^+, A_n^-. By direct substitution of (11) into (3), after symbolical expansion of the partial derivatives, it can be seen that, for (3) to hold, the coefficient A_{s0} must take the following value:

$$A_{s0} = -\frac{\mu_0 J}{4} = -\frac{\mu_0 I}{4\pi R^2} \quad (12)$$

Furthermore, in order for the solution not to diverge at the center of the bar (r=0), it is necessary to suppose that:

$$A_{\ell 0} = A_n^- = 0 \quad (13)$$

for any integer n.

The only unknown which need to be determined are then the coefficients A_n^+. These can be identified by imposing the boundary condition (7), which gives:

$$B_\theta(R,\theta) = -\frac{\partial A}{\partial r}(R,\theta) = -2A_{s0}R - \sum_{n=1,2,\ldots}\left(n\, A_n^+ R^{n-1}\right)\cos(n\theta)$$

$$= f(\theta) = F_0 + \sum_{n=1,2,\ldots} F_n \cos(n\theta) \quad (14)$$

This leads to impose the following identities:

$$F_0 = -2A_{s0}R \quad (15)$$

$$F_n = -n\,A_n^+ R^{n-1} \quad (16)$$

Equation (15) is automatically satisfied based on (9) and (12). Instead, equation (16) fixes the value of A_n^+ as follows:

$$A_n^+ = -\frac{F_n}{n\,R^{n-1}} \quad (17)$$

with F_n given by (10).

In conclusion, the flux density components in the circular bar region are completely known and, using (15) and (17), can be written as:

$$B_r(r,\theta) = \frac{1}{r}\frac{\partial A}{\partial \theta} = \sum_{n=1,2,\ldots} F_n \left(\frac{r}{R}\right)^{n-1} \sin(n\theta) \quad (18)$$

$$B_\theta(r,\theta) = -\frac{\partial A}{\partial r} = F_0\,\frac{r}{R} + \sum_{n=1,2,\ldots} F_n \left(\frac{r}{R}\right)^{n-1} \cos(n\theta) \quad (19)$$

10.3.2 Slot leakage inductance calculation

The slot leakage inductance L_{bar} of an individual round bar can be determined by computing the magnetic energy E_m stored in the slot (bar and slot opening regions included) and then writing [1], [2], [5]:

$$L_{bar} = 2\,E_m / I^2 \quad (20)$$

where I is the total current (2) flowing through the bar. Calling L the machine core length, the magnetic energy in the overall slot region can be written as:

$$E_m = E_{m,op} + E_{m,bar} \quad (21)$$

where $E_{m,op}$ is the energy stored in the slot opening region:

$$E_{m,op} = \frac{L\,d\,h}{2\mu_0} B_{op}^{\ 2} = \frac{L\,d\,h}{2\mu_0}\left(\frac{\mu_0\,I}{d}\right)^2 = \frac{\mu_0\,L\,h\,I^2}{2\,d} \quad (22)$$

and $E_{m,bar}$ is the magnetic energy stored in the bar region:

$$E_{m,bar} = \frac{L}{2\mu_0}\int_0^R \int_0^{2\pi} \left[B_r(r,\theta) + B_\theta(r,\theta)\right]^2 r\,d\theta\,dr \quad (23)$$

The flux density components (18)-(19) can be substituted into (23), with coefficients F_0, F_n given by (9)-(10). After some symbolical expansions and algebraic manipulations, which are not included for the sake of brevity, the double integrals in (23) can be explicitly solved giving:

$$E_{m,bar} = \frac{\mu_0 I^2 L}{16\pi} + \frac{2\mu_0 I^2 L R^2}{\pi d^2} \sum_{n=1,2,\ldots} \frac{1}{n^3} \sin^2\left(\frac{d\,n}{2R}\right) \quad (24)$$

At this point, using (21), (22), (24) in (20), the bar leakage inductance is finally found to be:

$$L_{bar} = \frac{\mu_0 L}{8\pi} + \frac{\mu_0 L h}{d} + \frac{4\mu_0 L R^2}{\pi d^2} \sum_{n=1,2,\ldots} \frac{1}{n^3} \sin^2\left(\frac{d\,n}{2R}\right) \quad (25)$$

It can be observed that the first term in the right-side member of (25) represents the "internal" self-inductance that the round bar would have if it were placed in the free air [8]; the second term accounts for the leakage flux in the slot opening region; the third terms accounts for the field distortion inside the bar due to the surrounding ferromagnetic material.

The accurate expression (25) for a round bar embedded in a semi-closed slot is proposed as an alternative to the following approximated expression L'_{bar} available in the literature to evaluate the same quantity [9]:

$$L'_{bar} = \mu_0 L\left(0.785 - \frac{d}{4R} + \frac{h}{d}\right) \quad (26)$$

10.4 Accurate model validation through FEA and comparison with the simplified formula

In this Section the proposed accurate formula for the slot leakage computation of round bars in semi-closed slots, given by (25), is assessed by comparison against FEA. Furthermore, it is compared to the simplified formula, given by (26), available from the literature. The basic model adopted for FEA simulations is represented in Fig. 4 and is characterized by the dimensions given in Table I, where the meaning of the symbols is illustrated in Fig. 1.

TABLE I

R	5 mm	***d***	1 mm	***h***	0.5 mm

The bar leakage inductance is estimated by FEA, by the proposed accurate formula (25) and by the simplified one (26).

In order to cover a wider variety of possible design configurations, the comparison is first repeated for different bridge heights *h*, while parameters *R* and *d* are maintained the same as shown in Table I. The results are shown in Fig. 5.

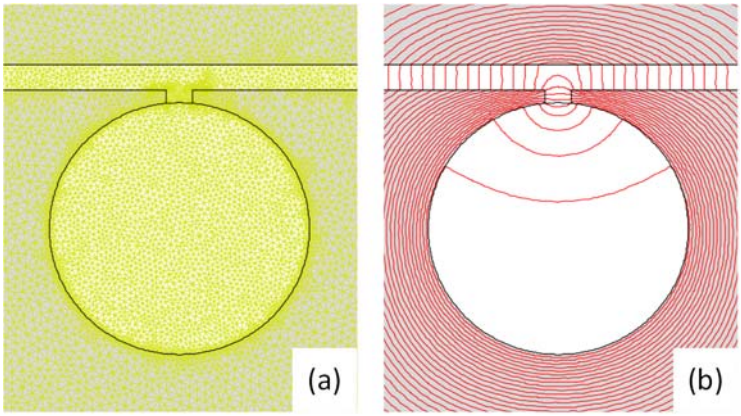

Fig. 4. (a) Slot meshed model and (b) Model FEA solution in the configuration with *R*=5 mm, h=0.5 mm, *d*=1 mm

Here it can be seen that the leakage inductance varies in an approximatively linear fashion with respect to the dimension *h*, as confirmed by both (25) and (26). The bridge height is varied in a range between 0.2 mm and 1 mm. In such a range, the error of the proposed accurate formula (25) with respect to FEA results remains practically unchanged and always below 2%, while the simplified formula leads to underestimate the leakage inductance with an error between 10% and 25%.

As a second study case, the circular bar radius *R* is changed while the slot opening dimensions *h*, *d* are kept the same as shown in Table I. The bar radius is varied between 1.5 mm and 8 mm. Leakage inductance evaluation results over such range are shown in Fig. 6. From Fig. 6 it appears that the proposed accurate formula (25) provides results which are always in very good accordance with FEA simulations, with errors that again keep lower than 2%. Conversely, the simplified expression (26) underestimates the leakage inductance with errors that strongly increase with the bar radius, up to around 25%.

As a final remark, it is worth observing that both the accurate and the simplified inductance expressions being compared hold under the hypothesis of unsaturated core. The effect of magnetic saturation on leakage inductances is highlighted in [9], [10] and, to capture it with an adequate level of accuracy, numerical calculation procedures through FEA [4] or meshless techniques [6] appears to be a mandatory choice.

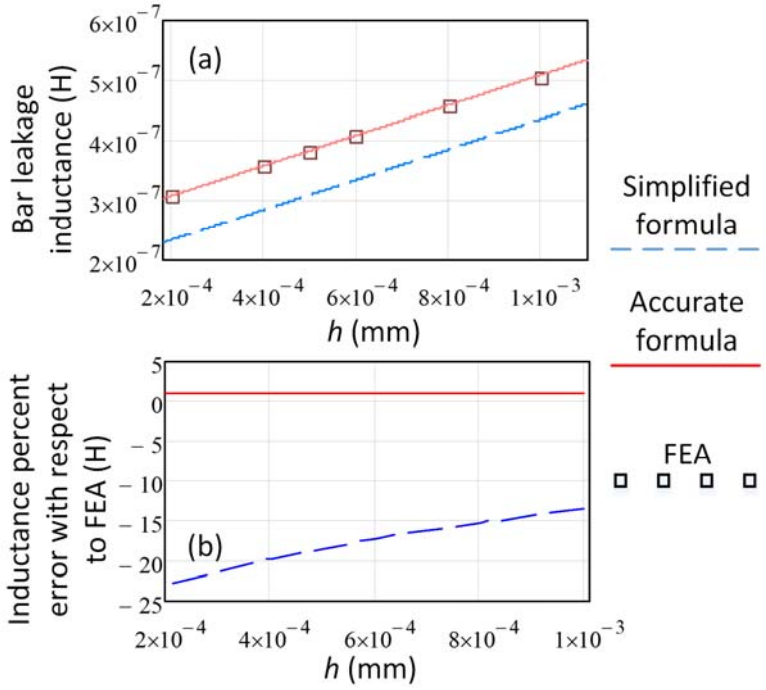

Fig. 5. (a) Rotor bar inductance evaluated with the proposed accurate formula, with the simplified formula available from the literature and with FEA, as a function of the bridge height *h*. (b) Corresponding percent errors with respect to FEA.

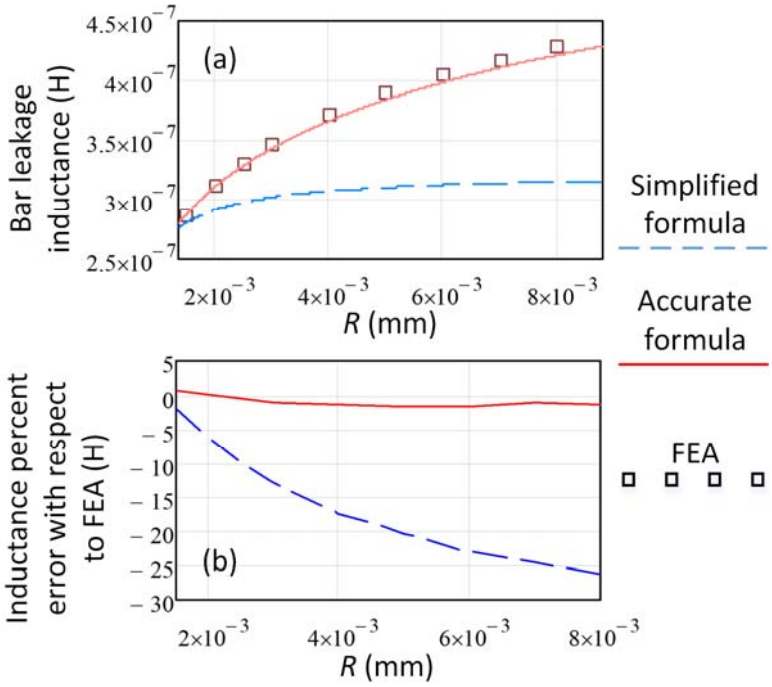

Fig. 6. (a) Rotor bar inductance evaluated with the proposed accurate formula, with the simplified formula available from the literature and with FEA, as a function of the bar radius *R*. (b) Corresponding percent errors with respect to FEA.

10.5 Conclusion

In this chapter the rotor leakage inductance of a circular bar embedded in a semi-closed slot (such as those used in many induction motor squirrel cages or in synchronous generator damper windings) has been investigated. An explicit easy-to-use formula has been derived for evaluating the leakage inductance by solving Poisson's equation for the magnetic vector potential in the semi-closed slot domain. The proposed expression has been validated against FEA and compared to simplified analytical formulas available in the literature. The comparison has been performed for various possible slot geometries characterized by different circular bar radii and different slot opening dimensions. In all the cases taken into account, it has been shown that the proposed expression yields very accurate results, which are in excellent accordance with FEA simulations (errors less than 2%) while the traditional simplified formulas may lead to remarkable errors (in the order of 25%) with respect to FEA estimations.

10.6 References

[1] I. Boldea and S. A. Nasar, *The Induction Machine Handbook*. Boca Raton, FL: CRC Press, 2002.

[2] P. L. Alger, *Induction Machines*, 2nd ed. New York: Gordon and Breach,1970.

[3] M. Wallin, J. Bladh, U. Lundin, "Damper Winding Influence on Unbalanced Magnetic Pull in Salient Pole Generators With Rotor Eccentricity", *IEEE Transactions on Magnetics,* vol. 49, no. 9, pp. 5158-5165, Sept. 2013.

[4] Zaixun Ling, Libing Zhou, Siyuan Guo, Yi Zhang, "Equivalent Circuit Parameters Calculation of Induction Motor by Finite Element Analysis", *IEEE Transactions on Magnetics,* vol. 50, no. 2, pp. 833-836, Feb. 2014.

[5] A. Boglietti, A. Cavagnino, M. Lazzari, "Computational Algorithms for Induction-Motor Equivalent Circuit Parameter Determination—Part I: Resistances and Leakage Reactances", *IEEE Transactions on Industrial Electronics,* vol.58, no.9, pp.3723,3733, Sept. 2011.

[6] E.H.R. Coppoli, R.C. Mesquita, R.S. Silva, "Induction Machines Modeling With Meshless Methods", *IEEE Transactions on Magnetics,* vol. 48, no. 2, pp. 847-850, Feb. 2012.

[7] K. Boughrara, N. Takorabet, R. Ibtiouen, O. Touhami, F. Dubas, "Analytical Analysis of Cage Rotor Induction Motors in Healthy, Defective and Broken Bars Conditions", *IEEE Transactions on Magnetics,* 2014, in press, early access article available on IEEEXplore.

[8] J. D. Jackson, *Classical Electrodynamics*, John Wiley and Sons, New York, 1999.

[9] A. Tessarolo, "Leakage Field Analytical Computation in Semi-Closed Slots of Unsaturated Electric Machines", *IEEE Transactions on Energy*

[10] A. Boglietti, R.I. Bojoi, A. Cavagnino, P. Guglielmi, A. Miotto, "Analysis and Modeling of Rotor Slot Enclosure Effects in High-Speed Induction Motors", *IEEE Transactions on Industry Applications,* vol.48, no.4, pp.1279-1287, July-Aug. 2012.

11 Concluding remarks

In this doctoral thesis I have collected most of the research work produced during my Ph.D. course.

The main line of inquiry followed in the development of my Ph.D. study has been the attempt to approach many engineering problems related to electric machine design and analysis through analytical techniques that may be valuable alternative to traditional numerical approaches like finite element analysis. The main purpose which have been pursued in conceiving these approaches is the reduction in the computational burden required.

In this perspective, various electrical machines of practical interest in today's application have been addressed (induction motors, synchronous reluctance motors, permanent-magnet machines, wound-field machines) and, for any type of machine, some problems have been selected to develop innovative analytically-based computation approaches. The problems to solve have been selected based on the needs resulting from practical applications as well as by a careful consideration of the "gaps" in the state-of-the-art of electric machine analysis design and methodologies.

Interesting and innovative results have been found in regards to various subjects, like:

- the cogging torque analytical calculation and minimization in surface-mounted permanent-magnet machines based on the winding function theory
- the fully-analytical accurate computation of slot leakage inductances for induction machines by direct solution of Maxwell equations for the magnetic field
- the full-load torque waveform analytical prediction in synchronous reluctance machines through a magnetic-equivalent-circuit approach combined with conformal mapping techniques
- the computation of the magnetic field in the whole slotless machine domain by direct solution of the magnetic field equations.

All the results reported in this work have been presented in IEEE-sponsored or IEEE-cosponsored conferences and have been published in scientific papers currently available through IEEEXplore.